UNIVERSITY OF SOUTHAMPTON

FACULTY OF ENGINEERING AND THE ENVIRONMENT

Aeronautics, Astronautics and Computational Engineering

Plasma Based Jet Actuators for Flow Control

by

Xinfu Luo

Thesis for the degree of Doctor of Philosophy

May 2012

ABSTRACT

A set of plasma based jet actuators were designed for flow control applications. The characteristics of these actuators and their flow control applications were studied experimentally in a low speed wind tunnel.

A dielectric barrier discharge (DBD) based jet actuator is designed, which is made of a covered cavity with two spanwise aligned parallel slots. Two-component particle image velocimetry (PIV) measurements were conducted to determine the effect of actuator in quiescent air and on a canonical zero pressure gradient turbulent boundary layer. It was found that the designed plasma jet actuator produced a transverse jet similar to a continuously blowing jet but with no mass addition into the flow field. The device is different from a traditional alternative blowing-and-suction synthetic jet as the current jet is continuously blown. As such, the DBD based jet actuator is different from either a mass injection blowing jet actuator or a traditional diaphragm based synthetic jet actuator. The impact of the actuation with the designed actuator on the boundary layer characteristics was investigated in detail at different Reynolds numbers.

Circular cylinder wake flow control using a newly designed five-electrode plasma jet actuator is also presented in this thesis. This plasma actuator configuration mounted on the cylinder model can easily produce either a downward or upward jet into the flow around the circular cylinder by simply adjusting the same five electrodes' electrical circuits. The experiments were performed at Reynolds numbers from 7,000 to 24,000. Wake profile measurements were made to evaluate the modification to the mean and fluctuation velocities in the cylinder wake. The results shown that the cylinder wake flow and the turbulence levels in the wake were modified under the actuations, sectional drag reduction and drag increment were obtained by different actuator actuation directions. The study suggested that this new designed five-electrode actuator can be applied to practical separation suppression or enhancement control by adjusting the plasma actuator electric circuits conveniently.

Contents

List of figures

viii

List of tables

x

DECLARATION OF AUTHORSHIP

I, Xinfu Luo

declare that the thesis entitled

Plasma Based Jet Actuators for Flow Control

and the work presented in the thesis are both my own, and have been generated by me as the result of my own original research. I confirm that:

- this work was done wholly or mainly while in candidature for a research degree at this University;
- where any part of this thesis has previously been submitted for a degree or any other qualification at this University or any other institution, this has been clearly stated;
- where I have consulted the published work of others, this is always clearly attributed;
- where I have quoted from the work of others, the source is always given. With the exception of such quotations, this thesis is entirely my own work;
- I have acknowledged all main sources of help;
- where the thesis is based on work done by myself jointly with others, I have made clear exactly what was done by others and what I have contributed myself;
- parts of this work have been published as:

- Luo, X. and Zhang, X., 2011, "Dielectric barrier discharge based jet actuator for flow control," *41st AIAA Fluid Dynamics Conference and Exhibit*, AIAA paper 2011-3988.

- Zhang, X., Luo, X. and Chen, P., 2011, "Airfoil flow control using plasma actuation and Coanda effect ," *29th AIAA Applied Aerodynamics Conference*, AIAA paper 2011-3516.

- Peers, E., Huang, X., and Luo, X., 2009, "A numerical model of plasma-actuator effects in flow-induced noise control," *IEEE transactions on plasma*, Vol. 37, No. 11, pp. 2250-2256.

Signed:

Date:

Acknowledgements

There are many individuals that I would like to thank for providing me with support during my period of Ph.D. study. First of all, I would like to express my sincere gratitude to my supervisor, Professor Xin Zhang, for his guidance, encouragement and patience throughout the research period. He has shown me what a scientist should do and how to become a researcher. I would also like to thank my advisor, Dr. Zhiwei Hu, for his support and sharing his knowledge and experience.

I am very grateful to Dr. Xun Huang and Dr. Yong Li for helping me learn experimental techniques and for assisting me with the experiments. I would like to thank all other colleagues in the AFM Group for their warm friendship and support during my Ph.D. study. I would also like to thank my old friends in China, for their constant encouragement through all these years.

Finally, I would like to show my greatest appreciation to my family and especially to my dear wife, Lan Wei, in particularly for her encouragement and taking care of our lovely young daughter over these years. Without her support and hard work, this work could not have been completed.

Definitions and abbreviations

Nomenclature

$b_{1/2}$	wake half-width, m
c_d	drag coefficient
D	distance between actuator two slots centerline or cylinder diameter, m
H	shape factor
P	static pressure, Pa
P_{atm}	atmospheric pressure, Pa
ΔP	relative static pressure (P-P_{atm}), Pa
Re	Reynolds number
Re_D	Reynolds number based on the cylinder diameter
U	mean streamwise velocity, m/s
ΔU	streamwise velocity defection, m/s
ΔU_{max}	maximum of velocity reduction, m/s
u	streamwise velocity fluctuations, m/s
U_{rms}	RMS of streamwise velocity, m/s
U_∞	freestream velocity, m/s
u_τ	friction velocity, m/s
u^+	normalized streamwise mean velocity (U/u_τ)
V	mean vertical velocity, m/s

v	vertical velocity fluctuations, m/s
V_{pp}	peak-to-peak voltage, V
Vel	velocity magnitude, m/s
W	mean transverse velocity, m/s
w	transverse velocity fluctuations, m/s
W_{rms}	RMS of transverse velocity, m/s
X	streamwise coordinate, m
$\varDelta X$	streamwise distance from the actuator downstream slot centerline in, m
Y	vertical coordinate, m
y^+	normalized wall normal coordinate (Yu_τ/ν)
Z	transverse coordinate, m

Greek symbols

δ	boundary layer thickness
δ^*	boundary layer displacement thickness
θ	boundary layer momentum thickness

Abbreviations

AC   alternative current

DC   direct current

AC+DC a plasma actuator configuration combined with AC and DC power supplies

DBD   dielectric barrier discharge

IGBT   insulated gate bipolar transistor

PIV   particle image velocimetry

RMS   root mean square

SD   sliding discharge

TBL   turbulent boundary layer

ZPG   zero pressure gradient

Chapter 1

Introduction

Plasma actuators are relatively new devices for flow control. A dielectric barrier discharge (DBD) actuator is a commonly used type of plasma actuators. A single DBD actuator consists of two electrodes separated by a dielectric, where the upper electrode is usually exposed to the flow and the lower electrode is insulated. The actuator is driven by a high frequency (hundreds Hz to tens kilo-Hz) AC voltage of several thousand volts. The electrodes can be fabricated from metal tapes or wires, and dielectric can made from Kapton, glass, ceramics, rubber and other materials. The actuators are inherently robust, relatively easy and inexpensive for practical flow control applications [1]. However they also suffer from a lack of control authority.

There are a number of flow control methods using a jet issued into an oncoming stream in the transverse direction (either with a net mass flow or with a zero net mass flux). Zero net mass flux jets (or synthetic jets) are formed from the working fluid of the system in which they are applied, and have been widely used as active flow control devices. These types of devices commonly use an oscillating diaphragm on the floor of a cavity to produce the required jets. The actuator units usually are flush mounted on the aerodynamic surface of interest. The diaphragm is driven periodically and hence the fluid is alternatively ejected from or sucked into the cavity at a certain frequency. A comprehensive review of the synthetic jets was given by Glezer and Amitay [2].

The two active flow control devices mentioned above operate on fundamentally different mechanisms. The work present here aims to investigate a new concept of constructing a flow control device that combines the features of both plasma actuators and synthetic jets. In order to produce a vertical plasma jet just using a single DBD, a normal DBD actuator is installed into a cavity and aligned perpendicular to the

freestream. The jet velocity and actuation frequency can be controlled through the plasma actuation parameter adjustment. In this study, the plasma induced ionic wind injects into the flow field through a spanwise oriented rectangular slot. As the air in the cavity is ionized by the plasma actuation, a constant air supply is needed and to this purpose an air supply slot with the same size is integrated into the system to supply fresh air to the cavity.

In this work, the above mentioned DBD based plasma jet actuator was designed and used to control a ZPG TBL flow. One objective of this research is to investigate the physical mechanism associated with TBL control using the new DBD based plasma jet actuators and discern their applications in other flow control applications such as airfoil, bluff body and others.

On the other hand, bluff body wakes affect the performance of many air vehicles, thus motivating significant research efforts into modifications of the unexpected wake effects. For this reason, another objective of the work presented in this thesis is to develop and implement plasma based jet actuators for the control of a circular cylinder wake. Bluff body wake flow is usually characterized by high level of unsteadiness, large regions of separated flow, and highly fluctuating pressures. Problems resulting from bluff body wakes including high drag, noise emissions, and distorted optimal path of separated shear layers. The high drag penalty due to separated flows is a significant problem for commercial and military vehicles. Another relevant issue is that the aircraft noise can be associated with vortex shedding from landing gear structures and the level could be quite high. The representative shapes on a landing gear are bluff bodies. Those situations require regularization of the separated flow. Several combinations of the designed plasma actuators are implemented in this research.

Many studies have been conducted to control the flow behavior using the downward jet for the main flow at different Reynolds numbers. However, less study has been conducted using an upward jet. With this background, the aim of this study was to investigate the wake characteristics behind a circular cylinder using the downward and upward plasma based jet actuators under different Reynolds number. The downward and upward jets to the main flow direction were induced by changing electrode

arrangements. The flow behaviors of the wake generated by the introduction of the downward and upward plasma based jet actuators were investigated using PIV.

This thesis describes the experimental works performed to control the TBL and circular cylinder flows using plasma based jet actuators. The thesis is structured into several chapters. Chapter 2 provides a review of the fundamental mechanisms of the boundary layer and cylinder flows and the existing methods for their flow control. Relevant plasma actuators were also introduced in this chapter. Chapter 3 is concerned with the experimental results of the TBL flow control by using a newly designed plasma jet actuator. The facilities and the experimental setup used for the research including the design of the wind tunnel model and the plasma actuator system are also presented. Chapter 4 is devoted to the experimental results obtained from wind tunnel testing on circular cylinder flow control using different combination plasma actuators. The baseline flow and wake fields with and without plasma actuations of a circular cylinder are discussed. Conclusions and a discussion on future work are presented in Chapter 5.

Chapter 2

Literature Review

In this chapter, works related to plasma actuators and their applications, TBL flow and its control, circular cylinder flow and its control are reviewed.

2.1 Plasma Actuators

There are various types of actuators for flow control applications, and these can be classified in a number of ways. Cattafesta III and Sheplak [3] classified them as illustrated in Figure 2.1, which classified the actuators based on function as fluidic, moving object/surface, plasma and others.
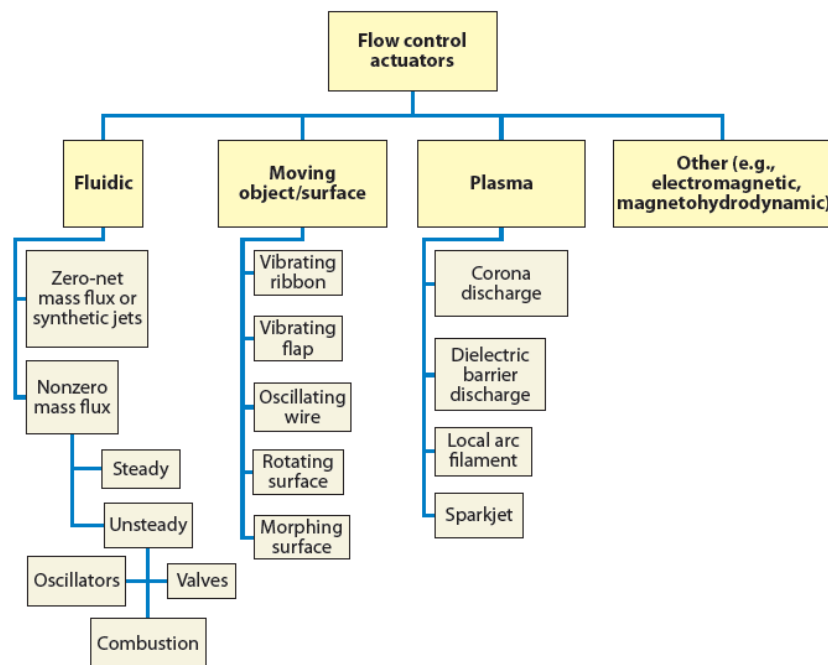
Figure 2.1: A typical classification of flow control actuators [3].

Their review provided a framework for the discussion of actuator specifications, characteristics, selection, design, and classification for aeronautical applications and also highlighted the strengths and inevitable drawbacks of each and potential future research directions. Because the work in this thesis is based on plasma actuators, the relevant topic on plasma actuators is discussed separately here.

Plasma is formed by particles which break down into positive and negative ions under sufficient energy. A simple plasma actuator consists of two electrodes powered by high voltage (AC or/ and DC). When a high enough voltage (kilo-volts) is applied, cold plasma appears between the electrodes. The discharge is based on the mechanism of electron avalanche, and its regime is a function of voltage-current. These discharges can be achieved with high voltage from a few kilo-Volts to several tens of kilo-Volts, frequency from 50 Hz to 50 kHz, and current from a few μA to a few mA.

A detailed discussion of the main characteristics of plasma can be found in Roth's [4]. Collision ions and neutral molecules in electrode gap form electric wind, corona or/and ionic wind, and flow between the electrodes. An equation for velocity of electric wind is given by:

$$v_G = k \sqrt{\frac{i}{\rho \mu}} \qquad (2.1)$$

where k is geometrical constant, μ is the ion mobility, i is the time-average current and ρ is gas density. The velocity of ions is:

$$v_i = \mu E \qquad (2.2)$$

Where E is intensity of electric field. The velocity of ions can usually reach hundreds or thousands meters per second, but the electric wind velocity is about a few meters per second. A parametric study performed by Forte et al [5] in order to increase the velocity of the ionic wind induced by DBD actuators. Their results indicated that an optimization of geometrical and electrical parameters can obtain a time-averaged ionic wind velocity up to 8 m/s at 0.5 mm from the wall.

A surface corona discharge basically uses two wire-electrodes embedded on the surface (not covered). The anode diameter is less than the cathode's. When the electric field strength is greater than the breakdown energy of the surrounding neutral particles, an electrical discharge brought on by the ionization of air surrounding a conductor.

Increasing of onset voltage at a certain gap between the electrodes, the discharge regime will turn from a spot regime to a streamer regime and a thin sheet of blue ionized air will appear between the electrodes. The glow discharge is obtained with higher voltage; there is no thin sheet of blue ionized air between both electrodes but only a set of adjacent luminescent spots around both electrodes. This is usually called a typical corona. When the voltage increases further, filament will then occur. Surface corona discharge is sensitive to humidity, pressure, temperature, electrode geometry and other environmental conditions. The velocity of electric wind increases with applied current. The measured maximum velocity is at about 1mm above the surface [6].

In order to prevent the transition to corona/sparks, a dielectric barrier is placed between electrodes and AC frequencies from 50 Hz to 500 kHz are applied instead of using DC voltage input. The most typical actuator is surface dielectric barrier discharging (DBD), which was invented by Roth [7] in 1998. A simple DBD actuator consists of a dielectric with two electrodes placed on both sides. One electrode is excited by an AC high voltage and the other is grounded. When the voltage reaches the ignition value, plasma appears on both sides and induces electric wind at the same time. In practical use, the grounded electrode usually is encapsulated. Then there is no electric wind on the bottom side. Many detailed works [8,9,10,11] have been reported on the physics of the plasma. Electrical and mechanical properties are strongly dependent on various parameters such as electrode width, electrode gap, dielectric material and thickness, high voltage value and frequency and so on. Generally speaking, a body force is generated by the collisions of the accelerated ions with the neutral air molecules. Due to the force production mechanism, the force is limited to a small region close to the gap between the anodes and the cathodes. This force acts on the air to accelerate and hence change its velocity. The force will create a wall jet by accelerating the air tangentially to the wall in quiescent medium and leads to a pressure drop above the electrodes. The force depends on the operating voltage of the actuator. The body force is proportional to 3.5 power of the applied high AC voltage [12,13].

Moreau [14] summarized the velocity profiles of their DBD actuators as below:
- the velocity induced by the grounded electrode (when it is not encapsulated) is slightly smaller than the velocity induced by the high voltage electrode;
- as for the surface corona, the momentum comes from the region placed above

the air exposed electrode, meaning that the discharge induces a depression towards the wall;

- the maximum velocity is always reached at the limit of the plasma extension, usually placed at the downstream edge of the grounded electrode;

- at low frequency (from 300 to 700 Hz), and up to 20 kV, the maximum velocity which is usually at about 0.5mm above the wall, increases linearly with the applied voltage.

As to the induced net force, the main findings are [14]:

- the waveform is of great importance in the net force. In fact, the positive saw tooth waveform produces the greatest net force for a given input power;

- the optimum frequency is 5 kHz (under their conditions);

- thicker dielectric configurations are generally able to produce higher maximum net forces because the dielectric is able to withstand higher currents;

- net force is proportional to the applied frequency;

- the force induced by a positive pulse is greater than the one induced by a negative pulse.

Plasma actuators are relatively new devices for flow control that have several obvious advantages but also disadvantages. Some advantages were summarized by Grundmann [15] as following:

- No moving parts.

- Very short response time. It is in the order of 10 to 100 μs depending on the operating frequency.

- Operable in a wide frequency range. The operating frequency can be increased up to 100 kHz,

- Simple integration into an aerodynamic model. The plasma actuator consists of just two foil-like electrodes and an insulation film in between.

- Low system mass. The actuator itself is very light; the main weight comes from the power supplies for the actuators.

The main disadvantage is the low efficiency of energy conversion and high voltage application. These actuators may also modify the gas properties near the wall (such as density and temperature). But overall it is a very promising device for flow control

applications. Consequently, plasma actuators are now widely used in flow controls, especially in boundary layer flow control and relevant areas.

Depending on different discharge, many plasma actuators have been developed for practical flow control. Some actuators for flow control application are listed below:

Surface corona discharge actuator. Corona discharge actuators use an anode and a cathode mounted in the working fluid. The anode emits positive ions that travel to and bombard the cathode surface. A typical configuration of DC plasma actuator is shown in Figure 2.2.
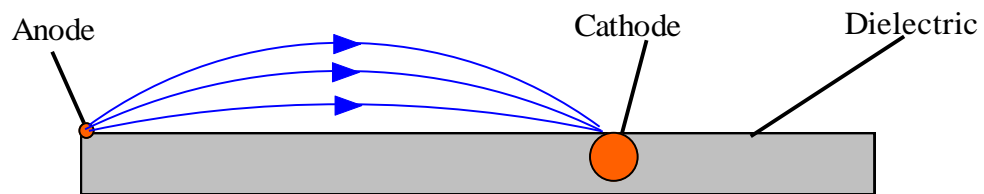
Figure 2.2: DC discharge plasma actuator.

These kinds of actuators have been used for a number of fluid dynamic applications, which showed their abilities for drag reduction [16,17]. Control of low velocity airflow along a flat plate by a DC surface corona discharge was investigated by Moreau et al [18]. A significant drag reduction has been achieved for velocities up to 25 m/s. The maximum drag reduction is about 30% at 1mm downstream of the cathode and 35% at the trailing edge (70mm downstream of the cathode). The drag decreases with the applied current.

Surface DBD actuators. A single DBD consists of two electrodes separated by a dielectric, while the upper electrode is usually exposed to the flow and the lower electrode is insulated. This type of actuator is the most commonly used plasma actuator, as sketched in Figure 2.3.
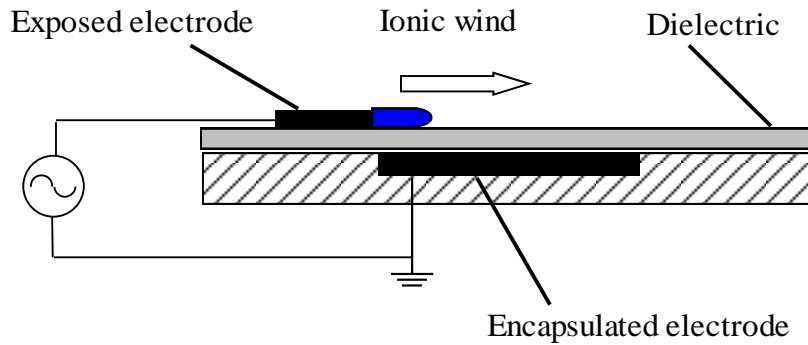
Figure 2.3: A typical DBD actuator.

This actuator is driven by a high frequency (hundreds Hertz to tens kilo-Hertz) AC-voltage of several thousand volts. The electrodes can be fabricated from metal tape or wire, dielectric can made from Kapton, glass, ceramics, rubber and other materials, making them inherently robust, relatively easy and inexpensive for practical flow control applications. Roth [37] first demonstrated a variety of flow control applications in boundary layers. Streamwise and spanwise oriented actuators were used to alter the velocity profiles of boundary layers at different velocities. Drag reduction and increment were observed on a panel downstream of the actuator, depending on the actuator's orientation. Investigations for TBL drag reduction were performed by Jukes et al. [19,20], they used opposing pairs of asymmetric surface AC glow discharge plasma electrodes to produce spanwise flow oscillation in the near-wall region of a TBL. In their study, the electrode sheet was affixed to a heat sink flush mounted 1.9m from the leading edge of a 3m long flat plate, over which a TBL was developed. The freestream speed was 1.8m/s and the boundary layer thickness is approximately 70mm at the measurement position. The plasma jet velocity was around 1 m/s and the frequency of the generated velocity oscillation was 21 Hz. A 22% drag reduction was reported. Investigations of different plasma actuators for boundary layer flow control have also been done by others [21,22].

Apart from using a single actuator, actuators can also be implemented as arrays [37]. The actuators in an array can be driven with voltages of the same phase or with a phase shift between them. A phase shift driving causes an electrostatic wave to move along the surface and results in higher wall-jet velocities than with actuators in phase. Roth also invented actuators combine peristaltic and paraelectric effect and the induced electric wind can be reversed.

Usually, the plasma induced flow velocity is limited and has an asymptotic behavior with increasing operating voltage [23], so the applications are normally restricted to small scale. The above mentioned DBD arrays, energized by zero-phase delayed or phase- shifted high voltages can be used in larger scale. However, the mutual interaction between successive discharges introduces negative effects to the standard multi-DBD actuators as well. Benard et al [24] newly designed an electrode for large-scale flow control applications. It replaces each single two-electrode DBD (S2DBD) by a three-electrode DBD (S3DBD) where the third electrode acts as a shield between the two successive DBDs (Figure 2.4).
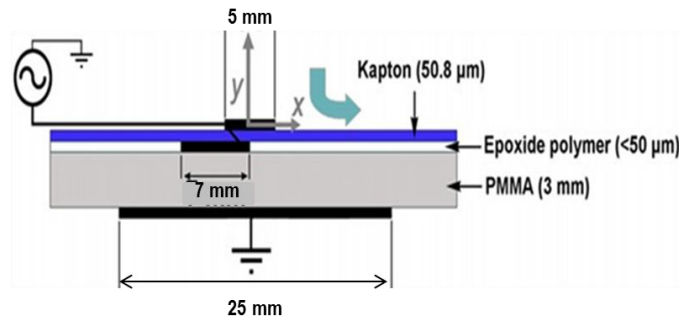
Figure 2.4: A S3DBD actuator [24].
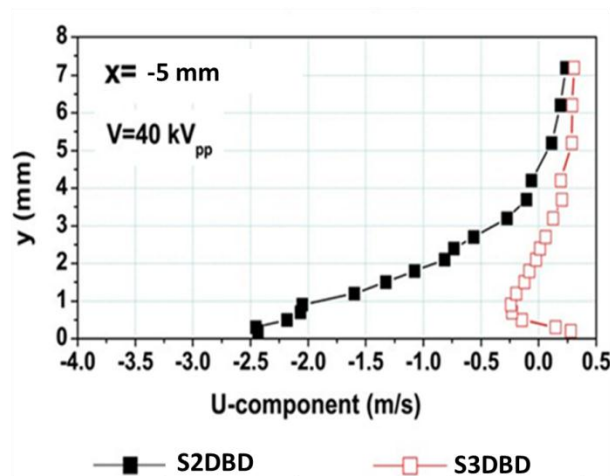
Figure 2.5: Velocity component of backward flow [24].

Experimental measurements results shown that the S3DBD design can reduce the backward flow by 65% (Figure 2.5).

Because a S3DBD can eliminate the backward flow, it may induce a larger and steadier plasma flow. Their results showed that the interaction between the electrodes, although not fully cancelled, is strongly reduced. This new DBD design conduces to a nearly constant plasma speed over the whole actuation surface (Figure 2.6). From a practical point of view, this design is suitable for large-scale and stable actuation applications.
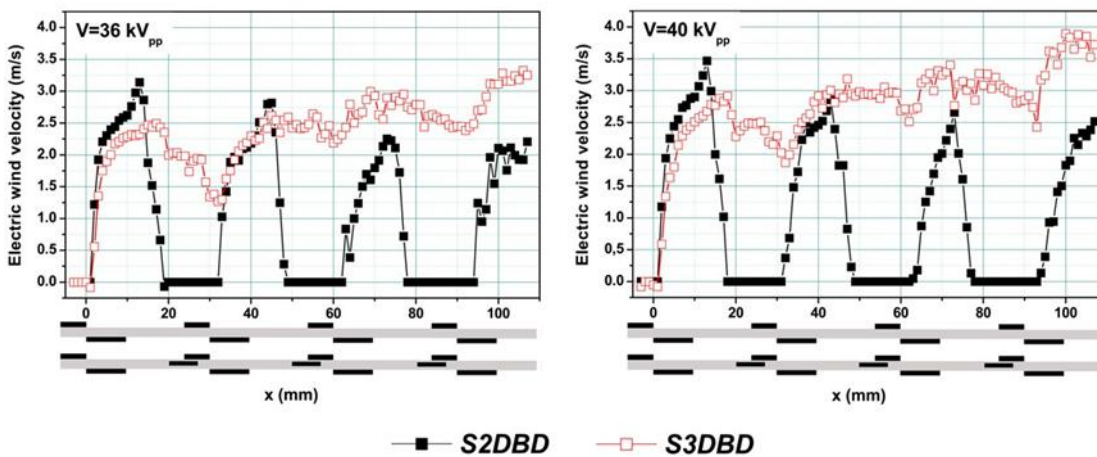
Figure 2.6: Electric wind velocity for multi-DBD array [24].

Plasma synthetic jet actuators. A plasma actuator design consisting of an annular electrode array, the Plasma Synthetic Jet Actuator (PSJA), was investigated by Santhanakrishnan [25]. This particular plasma induced flow is in the form of a vertical synthetic jet (Figure 2.7). This configuration is basically still a DBD actuator, but its induced flow alignment is perpendicular to the surface compare to a tangential wind of a traditional DBD, we therefore discuss it separately. If the jet is induced by using two rectangular-strip exposed electrodes and one embedded electrode (Figure 2.8), it is usually called a linear plasma synthetic jet actuator (L-PSJA). A PSJA configuration can be easily reversed to act as a suction device by exchange the electrodes.
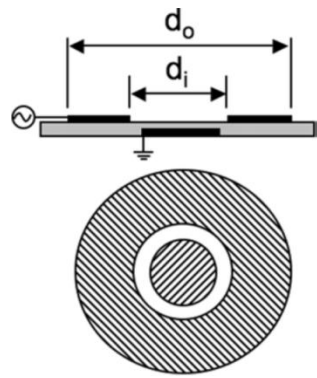
a) top view and cross section   **b) Plasma ring created on actuation**
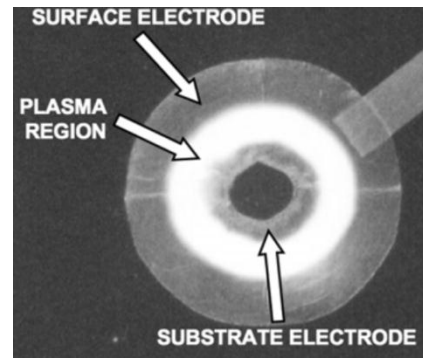
Figure 2.7: Schematic of a PSJA [22].
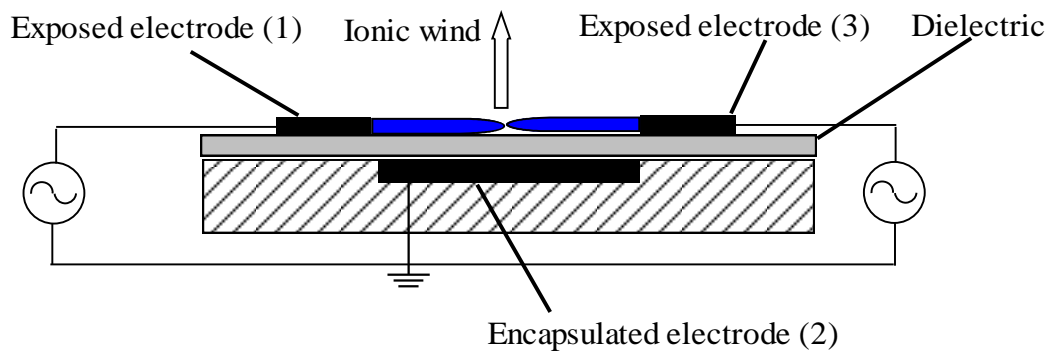
Figure 2.8: An L-PSJA actuator.

The two actuators were observed to affect the flat plate boundary layer flow field in different manners. The PSJA was observed to interact with a cross flow in a similar manner as a conventional jet. The interaction of the L-PSJA with a cross flow results in the formation of a cross stream vortex downstream of the plasma region, similar to a single DBD actuator. The effectiveness of the plasma synthetic jet in penetrating the mean flow was found to decrease with increase in Reynolds number.

Three-electrode actuators. More recently, a new group of plasma actuators consisting in three electrodes devices has been developed [26] (Figure 2.9).

13
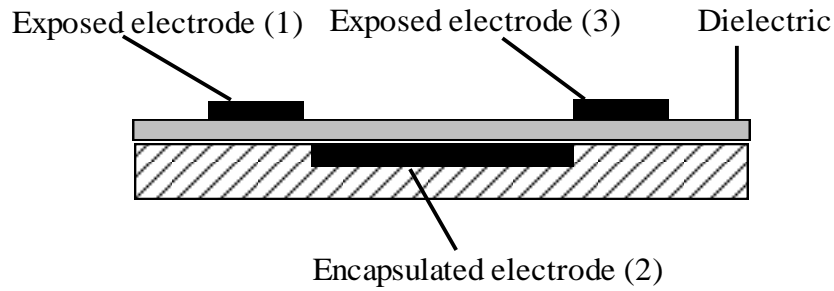
Figure 2.9: Configuration of a three electrodes plasma actuator.

Two upper electrodes (1) and (3) are flush mounted on the air-exposed surface, and a lower electrode (2) is placed on the opposite side of the insulating surface. The concept is to utilize the AC DBD to weakly ionize the air, and then to superpose a DC potential that establishes a corona discharge between spatially separated electrodes. The DC component induces the sliding discharge.

With different AC and DC component combination circuits, some special plasma can be induced. If the first upper electrode (1) is at an AC voltage and the electrodes (2) and (3) are grounded, a typical surface dielectric barrier discharge is formed between electrodes (1) and (3), the actuator works like a conventional DBD actuator (Figure 2.10).
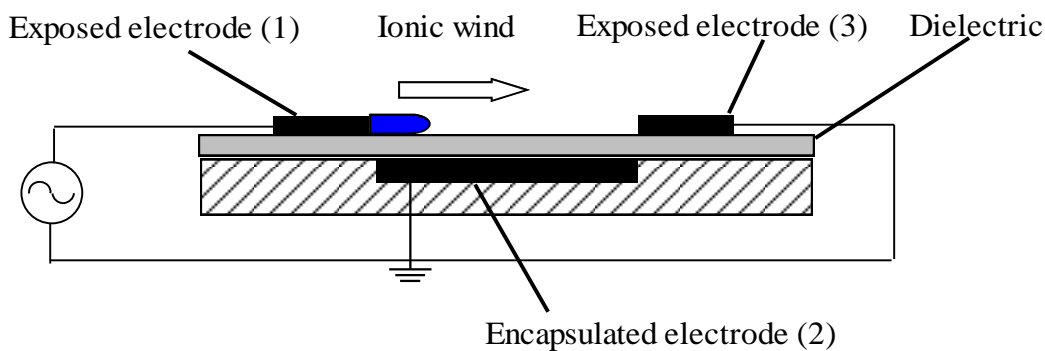
Figure 2.10: A three-electrode plasma actuator without DC.

On the other hand when the electrode (1) is at an AC voltage and the electrode (3) is applied to a high enough DC voltage with electrode (2) grounded, different discharges will be induced depending on the polarity of the DC voltage. A plasma sheet which occupies the whole electrode gap is produced when DC < 0. The direction of the

actuator induced electric wind depends on the applied AC voltage. By varying the AC voltage value one can make the global plume like flow direction and span angles almost lying in the range 0-180° referred to the dielectric surface (Figure 2.11). The discharge looks like a normal DBD, but with stronger actuation when DC > 0 (Figure 2.12). Both discharges were as stable as the corresponding DBD [27, 28, 29].
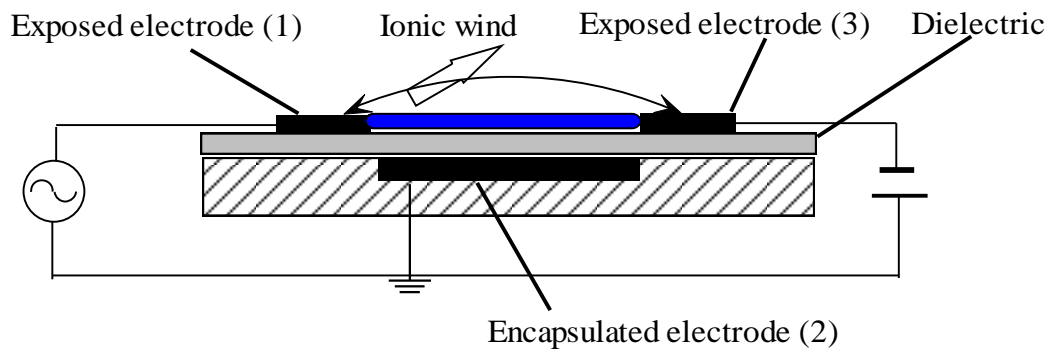
Figure 2.11: A three-electrode plasma actuator with DC<0.
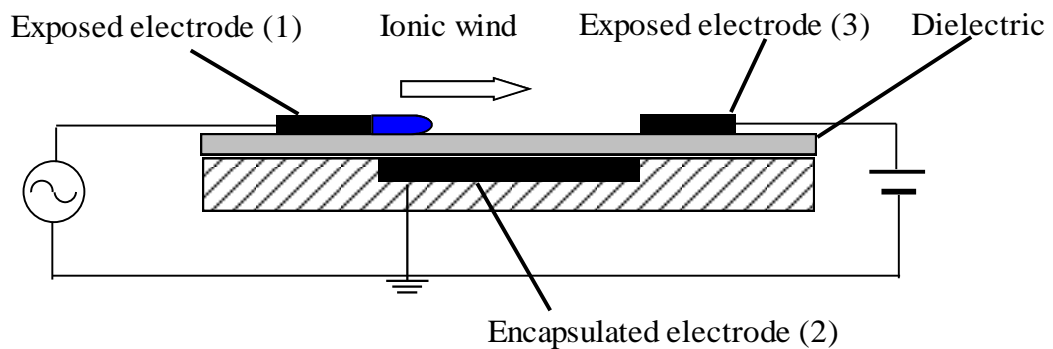
Figure 2.12: A three-electrode plasma actuator with DC>0.

The drag reduction in a circular cylinder was explored by Sosa et al [30] using these three-electrode plasma actuators. The results indicated that these actuators can reduce the drag coefficient by up to 25% with respect to the base flow drag coefficient. The three three-electrode plasma configurations mentioned above will be called as AC+DC actuation

Another design was made by Thomas et al [31]. In this case, the electrode (2) is connected to an AC voltage while a DC voltage (either positive or negative) is applied

to electrode (1) and the electrode (3) grounded (Figure 2.13). When the actuator is operating only with the AC input on, it works like two DBDs and very weak plasma can be seen near the edges of the two exposed electrodes. However, the addition of the DC induced visible plasma can extend the whole space between electrodes (1) and (3). The induced electric wind direction depends on the polarity of the input DC voltage. Sliding Discharge (SD) will be used to define those kinds of configurations in this thesis.
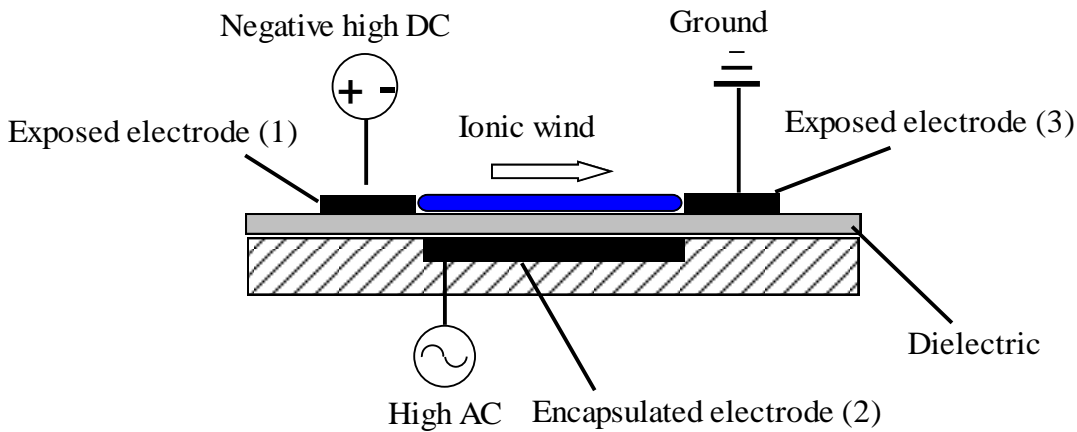
Figure 2.13: A SD plasma actuator configuration.

Roupassov et al designed a new DBD based actuator driven with repetitive nanosecond-scale pulse signal [32,33,34,35]. The rapid discharge (5–50 ns) promotes rapid gas heating that creates localized shock waves with little discernible electric wind, suggesting that these are no longer cold plasmas. This short-pulse DBD may substantially improve control authority in high-speed flows.

2.2 Turbulent Boundary Layer Flow and Its Control

Because a TBL produces significantly higher skin-friction drag than a laminar boundary layer and at most practical high Reynolds number the boundary layer flow is turbulent, much more efforts have been tried to understand the TBL fluid motions to achieve flow-control objectives[36]. Control of TBLs has been a subject of much interest owing to its fundamental research benefits. Both a thorough understanding of the underlying physics of turbulent flow and an efficient control algorithm are very important for successful flow control.

Turbulence is very difficult to precisely define. Tennekes and Lumley[37] described the characteristics of turbulent flows as below.

- Randomness. So the turbulence problems should be approached using statistical methods.

- The diffusivity is an important feature of turbulent flows, which causes the increasing rates of momentum, heat and mass transfers and exhibits spreading of velocity fluctuations through the surrounding fluid.

- Three-dimensional vorticity fluctuations. Turbulence is rotational and three dimensional and is characterised by high levels of fluctuating vorticity.

- Large Reynolds number always accompanies turbulent flows.

- Turbulent flows are always dissipative. The turbulence needs a continuous supply of energy to make up for these viscous losses.

Passive or active flow control can cause a beneficial change in boundary layer, which including drag reduction, flow-induced noise suppression, lift enhancement, mixing augmentation and so on. Active flow control is usually adopted to modify flow field characteristics to achieve a desired aerodynamic performance with combining sensing, actuation, flow physics and control. Compare to passive techniques, such as grooves or riblets, which use geometric shaping to adjust the gradient pressure on a surface to reduce drag, active control manipulates a flow field using a forcing system (addition of energy) to leverage a natural instability of the flow. Active flow control can use a small local energy input to attain a large effect and apply for complex dynamical processes control. Many attempts have been made to control boundary layer flows. These include the modification of the wall surface by installing riblets [38], using a compliant wall [39] or a spanwise oscillating wall [40]. An experimental investigation by Laadhari et al [41] was performed over a flat plate. The responses of a TBL under a local spanwise oscillation at various non-dimensional frequencies of the wall were tested. The study indicated that the three components of the turbulence intensities and the Reynolds stresses decrease along with the increase of the driving frequency. This reduction affects almost the whole boundary layer in a cross section at the middle of the oscillating wall. An extensive study of the near-wall structure of TBL over a spanwise oscillating wall was conducted by Choi and Clayton [42] to understand the turbulent drag reduction mechanisms. Under certain conditions, skin friction coefficient reductions as much as 45% were observed. Recently, by combining computational fluid dynamics (CFD),

control theories, and sensor/actuator technologies, significant progress has been made. Due to Direct numerical simulation (DNS) and large-eddy simulation (LES), the understanding of the physics of TBLs and free-shear flows has been significantly improved over the past two decades[43]. Here we mainly focus on works relevant to boundary layer flow control using blowing/suction and synthetic jet.

Among the control of boundary layer flows, the use of local suction/blowing has been studied in more detailed fashion because it provides a simple and efficient means for locally actuating wall-bounded flow. Moreover, the strength of suction/blowing can also be controlled with relative ease. Both steady and unsteady suction/blowing actuations were studied experimentally and numerically. Sano and Hirayama [44] examined the effect of steady blowing or suction through a spanwise slit in a TBL. They found that steady suction (blowing) increases (decreases) skin friction and decreases (increases) turbulent intensity behind the slot. Antonia et al.[45] measured the local wall-shear stress and Reynolds stresses in a low Reynolds number TBL with concentrated suction applied through a short porous wall strip and quantified the effect of suction on relaminarization and subsequent transition. Relaminarization occurred immediately downstream of the strip with a sufficiently large suction. They also proposed an empirical drag coefficient distribution that groups results obtained at different streamwise stations and different suction rates. Park and Choi [46] studied the effects of uniform blowing and suction on near-wall vortices by DNS. In the case of uniform blowing, the skin friction on the slot decreases rapidly. The near-wall streamwise vortices were lifted up by blowing, and thus the interaction of the vortices with the wall becomes weaker. Accordingly, the lifted vortices became stronger in the downstream direction due to less viscous diffusion (above the slot) and more tilting and stretching (downstream of the slot), resulting in an increase of the turbulence intensities as well as the skin friction downstream of the slot. On the other hand, in the case of uniform suction, the skin friction on the slot increased significantly. The near-wall streamwise vortices were drawn toward the wall by suction, and thus viscous diffusion becomes very effective near the slot, resulting in weaker streamwise vortices downstream of the slot. Therefore, the turbulence intensities as well as the skin friction decrease downstream of the slot. Krogstad and Kourakine [47] conducted experimental investigations the effect of weak blowing through a porous strip on a TBL. Kim et al.

[48] examined the effect of blowing velocity on the characteristics of the TBL through direct numerical simulations. Three different values of the blowing velocity under conditions of constant mass flow rate through the slot were assessed.

In contrast to the studies using steady blowing, Tardu [49] carried out experimental studies to compare the actuations of a periodically blowing system and a steady-blowing system. He found that both types of blowing led to a reduction in the skin friction. When the blowing frequency is larger than a critical value, the blowing induces a positive wall vorticity layer that subsequently rolls up into a coherent spanwise vortex. Further downstream, a negative vorticity layer rolls up. Experimental investigations were conducted by Park et al [50] to probe the effects of periodic blowing and suction through a spanwise slot on a TBL. Their results showed that the turbulent structures of boundary layer experience larger changes with higher forcing frequency. The skin friction reduced with increasing forcing frequency. Rhee and Sung [51] compared the experimental results by performing unsteady Reynolds-averaged Navier–Stokes simulations. Other works on the effects of wall suction or blowing were also reported [52,53,54].

Another widely used actuator is a synthetic jet actuator (SJA). A SJA is a jet generator with zero mass input but non-zero momentum output. The basic components of a SJA are a cavity and an oscillating material. A jet is synthesized by oscillatory flow in and out of the cavity via an orifice or a slit in one side of the cavity. The flow is induced by a vibrating membrane located on one wall of the cavity. Flow enters and exits the cavity through the orifice/slit by suction and blowing. Thus, over a single period of oscillation of the diaphragm, a turbulent-like jet that has been synthesized from the coalescence of a train of vortex rings, or vortex pairs, of the ambient fluid. Ingard and Labate [55] used standing waves in an acoustically driven circular tube to induce an oscillating velocity field in the vicinity of an end plate and observed the formation of zero-net mass flux jets from opposing trains of vortex rings on both sides of the orifice (Figure 2.14).
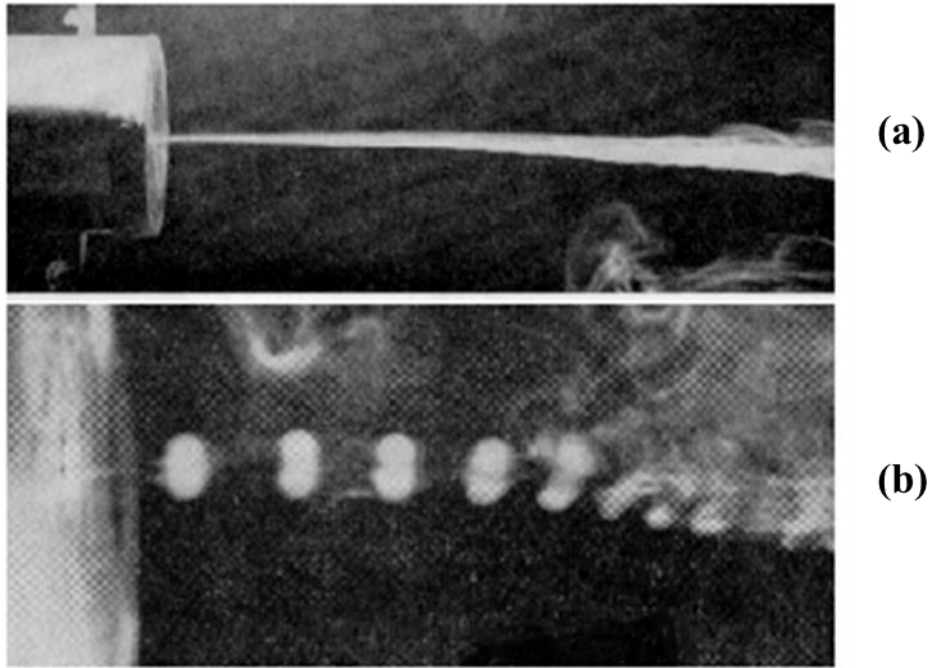
Figure 2.14: Jets driven by (a) steady and (b) stroboscopic illumination [55]

Piezoelectric synthetic jets have been used in numerous flow control applications. A representative zero-net mass flux device is shown in Figure 2.15. Glezer and Amitay summarized [56] its Pros include low power input, compact, thousands Hz bandwidth and broad range of length and time scales; Cons include relatively low control authority, resonant frequency response, piezoceramic aging and failure. Other relevant computational and experimental work was also conducted by many researchers [57,58,59]. Compare to traditional devices such as steady [60] and pulsed [61] jets, advantages of using SJA include simple compact structure, low cost and ease of operation. One obvious benefit of employing SJAs as a flow control device is that no air supply is needed and so there is no requirement for piping, connections, and compressors associated with steady jets. The properties of synthetic jets in the absence of cross flow have been investigated experimentally and numerically [62,63].

a) Schematic diagram of the actuator   b) Schlieren image of the synthetic jet
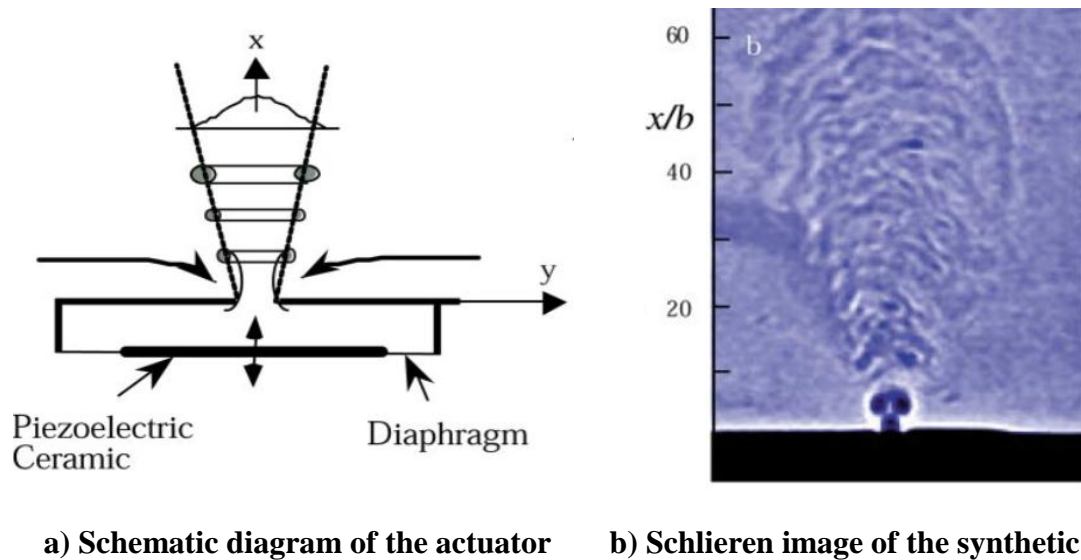
Figure 2.15: A piezoelectric synthetic jet actuator [56].

Among the many micro-active devices that have been used in flow control, SJAs have demonstrated a potential in modification of aerodynamic lift and drag [64], forebody flow-asymmetry management [65], flow separation control [66], and improvement of aircraft maneuverability [67]. Recent research in the field has emphasized on the need of understanding the SJA's effect on flow field and in particular its operation in a boundary layer under an adverse pressure gradient. Smith et al [8] demonstrated that significant lift could be generated on a two-dimensional cylinder using synthetic jets. A simulation study on the jet dynamics and its interaction with a flat plate boundary layer under ZPG has been systematically carried out using an incompressible Navier–Stokes solver [68].

The work present in this thesis aims to investigate a new concept of constructing a flow control device that combines the features of both plasma actuators and synthetic jets. In order to produce a vertical plasma jet just using a single DBD, a normal DBD actuator is installed into a cavity and aligned perpendicular to the freestream. The jet velocity and actuation frequency can be controlled through the plasma actuation parameter adjustment.

2.3 Flow around Circular Cylinder and Its Control

Flow over a cylinder is a fundamental fluid mechanics problem of practical importance. It has been studied extensively because of its widespread engineering applications and associated problems of vibration induced by the flow, wake turbulence, acoustic noise, and drag forces on bodies. The characteristics of cylinder flows were reviewed comprehensively by Williamson [69] and Zdravkovich [70].

Figure 2.16: Flow regimes of a circular cylinder [70].

A variety of flow regimes exists in the cylinder flow as shown in Figure 2.16. The flow field over the cylinder is symmetric at low values of Reynolds number. As the Reynolds

number increases, flow begins to separate behind the cylinder causing vortex shedding which is an unsteady phenomenon. The structure of the boundary and shear layers and vortex structure depends strongly on the Reynolds number. Based on boundary layer development and Re, there are three main flow regimes around a cylinder: subcritical, supercritical and transcritical [71]. Subcritical flow occurs between $300 < \text{Re} < 3 \times 10^5$ where the flow over the cylinder is completely laminar including laminar flow separation with a Strouhal number of 0.21. Supercritical flow occurs between $3 \times 10^5 < \text{Re} < 1.5 \times 10^6$ where the flow over the cylinder starts laminar and transitions to turbulent flow between the stagnation and separation points and the vortex shedding frequency is irregular. Transcritical flow occurs when $\text{Re} > 4.5 \times 10^6$ where the flow over the cylinder is completely turbulent and the Strouhal number is between 0.25 and 0.3. In all of these flow regimes, the flow separates from the cylinder surface and exhibits unstable, but periodic and alternating, three dimensional vortex shedding.

In this study, the Reynolds number varies from 7,000 to 24,000 which correspond to the subcritical regime. The vortex shedding in the subcritical regime is characterized by the turbulent transition in the shear layers and usually has two distinct stages: formation and shedding. For the formation stage, Prandtl [72] proposed that the vortices are formed behind the cylinder by the spiral roll-up of the free shear layer in an almost-fixed location; the free shear layer feeds the circulation into the growing vortices. Gerrard [73] suggested that, in the shedding stage, when the developing vortex becomes sufficiently strong it draws the other shear layer across the wake. The interaction of the oppositely-signed vorticity from the other shear layer cuts off the circulation and stops the growth of the vortex; this causes the vortex to shed into the wake. The vortex street is formed by the alternate shedding of the fully-grown vortices.

Many researches have been conducted on the control of flow over cylinders in order to reduce drag, increase lift, suppress noise, decrease vibration, and increase mixing or heat transfer. The method of control depends on the objective as well as the Reynolds number of the flow. Cylinder flow controls can be classified into three groups, passive control, open-loop active control and closed-loop active control, for cases of actuator(s) without power input, actuator(s) with power input but no sensor, and sensor(s) and actuator(s) with power input, respectively [74].

Flow control using passive flow control devices has been investigated by a number of researchers. Those devices including surface modifications with roughness [75], small secondary control cylinder [76, 77, 78], dimple[79], helical wire [80],splitter plate[81,82,83,84] and longitudinal groove[85]. Many open-loop active control methods have been also applied to circular cylinder flow, such as synthetic jet [86]; streamwise and spanwise cylinder oscillations [87,88,89]; steady and unsteady blowing/suction [90,91,92,93,94]; inflow oscillation[95]; electromagnetic forcing [96,97] and distributed forcing [98]. Among them Tokumaru & Dimotakis [99] experimentally obtained approximately 80% drag reduction at *Re* = 15,000 by using rotary oscillation has attracted many intensive experimental and numerical studies for bluff body drag reduction.

Recently, many work have involved in circular cylinder flow controls by using plasma actuators. Thomas et al [100] carried out experimental study of a circular cylinder by using steady and unsteady DBD plasma actuators at a Reynolds number of 3,3000. Their testing results showed that the turbulent intensities in the wake decreased, and the sound pressure levels also decreased. They also found that the actuation frequency of 1 is most effective for unsteady plasma actuators. Gregory et al [101] used 3D actuation based on combining DBD plasma actuator configurations for a circular cylinder flow control. Both tangential and perpendicular jets of plasma actuators were studied experimentally at a Reynolds number of 6,500. The measured drag coefficient decreased from 0.89 to 0.29 for tangential blowing. However drag coefficient for perpendicular blowing increased from 0.94 to 1.44 by using these DBD plasma actuators.

Juke et al [102] measured the changes of dynamic lift and drag forces by pulse DBD plasma actuations at a Reynolds number of 15,000. The lift over the circular cylinder could be increased by up to 300% using a single and short-duration pulse of DBD plasma actuators.

2.4 Summary

A review on plasma actuators, TBL flow and its control and flow around circular cylinder and its control has been presented. The literature review in the preceding sections gives the relative research into plasma actuators, boundary layer flows and circular cylinder flow. In particular the review highlights the work on their flow mechanisms and the various control methods applied to their flow control. The advantages of plasma actuators are also outlined. Current literature has shown that the majority of plasma actuator research and development has been applied to flow control applications. The design of plasma based jet actuator for flow control is still attractive for many researchers. The specific aims of the research are to:

- Develop plasma based jet actuator for flow control applications by applying it to the ZPG TBL.

- Develop combined three-electrode plasma actuators for circular cylinder flow control.

- To explore and analyse the major physics of flow control using the designed plasma based jet actuator on the TBL flow field and circular cylinder wake flow.

- Analyse the governing performance parameters of the new developed plasma jet actuators on the fluid fields.

Chapter 3

Turbulent Boundary Layer Flow Control Using DBD Based Jet Actuators

In this chapter, a DBD based plasma actuator was designed and used to control a ZPG TBL flow. The objective of this part of the research is to investigate the physics associated with TBL control using the DBD based plasma vertical jets and discern its applications in other flow control applications such as airfoil, bluff body and so on.

A new massless plasma actuator consisting of a normal DBD actuator set in a two slots cavity unit was investigated experimentally. This new actuator produces a vertical plasma jet into the operating flow field. There is no net mass exchange in the working fluid of the system, so the jet can be regarded as a zero-net mass flux jet. Wind tunnel experiments were conducted to assess the performance of the actuator for a TBL flow control.

3.1 Experimental Apparatus

3.1.1 Wind Tunnel

All the experimental research works were conducted in a low speed wind tunnel at the University of Southampton [103] (Figure 3.1).
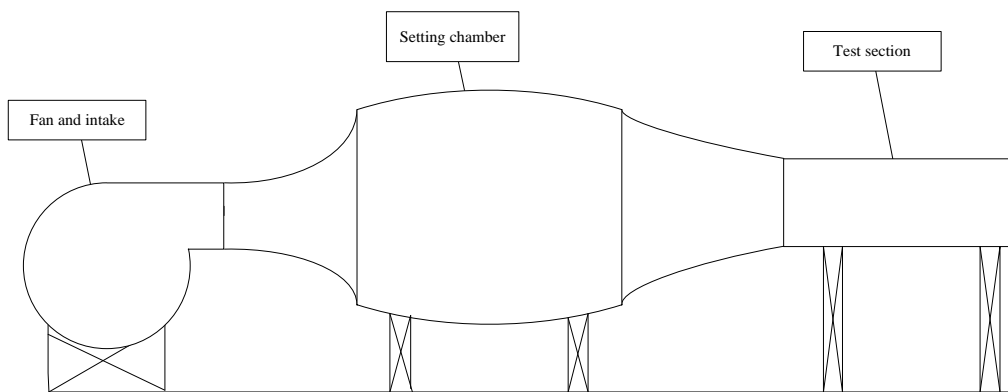
Figure 3.1: Schematic of the wind tunnel general assembly.

The wind tunnel was designed with a contraction ratio of 4:1 from the settling chamber to the main test section. An axial Halifax fan with 12 blades is driven by a 4 kW three-phase electric motor, providing a maximum fan speed of 1500 rpm. The maximum flow speed attainable in the test section is 25m/s (±0.04m/s). The original test section is 850mm×250mm×350mm in length, height and width, respectively. In this study, the wind tunnel was reassembled in another lab. In order to get enough length for the developing of the required TBL flow, we extended the test section length from 850mm to 1400mm. Subsequently, a new test section was made for the proposed research. Both of the side walls and the ceiling of the new designed test section are fitted with Perspex boards for the access of laser and camera used in the PIV measurements.

Because the wind tunnel was modified for inducing the required TBL flow, it is necessary to consider the turbulence level in the test section of the wind tunnel and keep its value at a reasonable level. The turbulence level was measured using hot-wire anemometry with a single wire probe. A newly developed traverse system was used to

28

position the hot-wire (Figure 3.2).
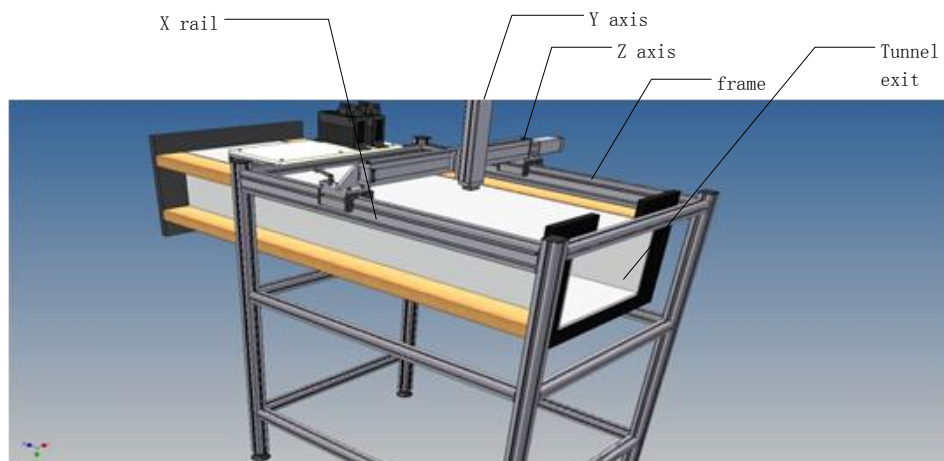
Figure 3.2: Traverse system in the wind tunnel.

The traverse system is mounted on a frame cross the wind tunnel ceiling. The two axes (vertical-horizontal) are combined with an Oriental Motor's motorized cylinder (EZAM4E030MC) mounted on the table of a motorized slide (EZSM4E050MC). The drive motor adopts the closed-loop α stepping motor that eliminates misstep and hunting which can achieve greater convenience and performance in positioning. The accuracy of either cylinder or slide is 0.01mm which provides enough resolution for the flow field measurement. The combination axes are mounted on the slide rail of the frame and can move in the longitudinal direction manually. Two Oriental Motor's Limo ESMC-C2 linear motion controllers were connected to a PC that operated the traverse system with the provided editing software.

The hot-wire probe was calibrated in the empty wind tunnel with a pitot tube. The hot-wire and pitot tube were located at the centre of the test section but separated by 50 mm in the vertical direction to avoid flow measurement interference. The hot-wire system used for the experimental work employed a Dantec 5μm single component probe connected to a Mini CTA (54T30). The output signal from the bridge unit was fed into an analogue-to-digital converter in a PXI chassis. The data acquisition and processing was described in Figure 3.3.
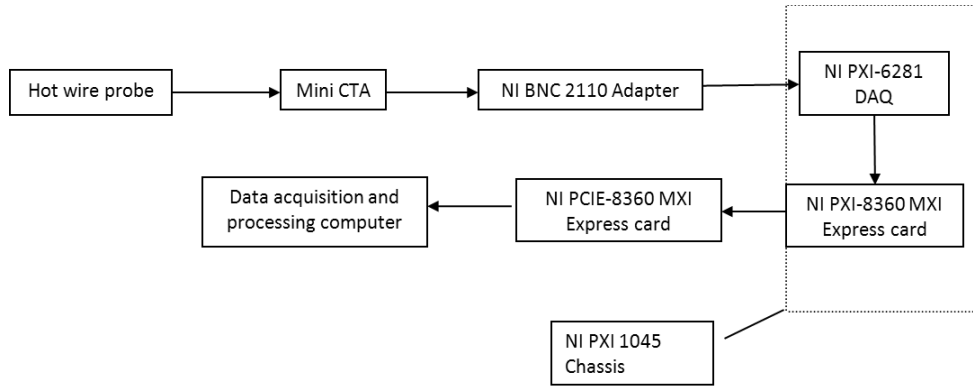
Figure 3.3: Hot-wire measurement system.

The calibration of the hot-wire anemometry system usually use a King's Law:

$$E^2 = A + BU_\infty^n \tag{3.1}$$

Where E is the voltage across the wire, U_∞ is the velocity of the flow normal to the wire and A, B, and n are constants, usually $n = 0.45$. It is common for hot-wire probe calibration that A and B are found by measuring the voltage, E, obtained for a number of known flow velocities and performing a least squares fit for the values of A and B which produce the best fit to the data. The values of A and B depend on the settings of the anemometer circuitry, the resistance of the wire used, the air temperature, and, to a lesser extent, the relative humidity of the air.

The selected hot-wire was calibrated in a range of freestream velocities. A typical calibration result was shown in Figure 3.4.
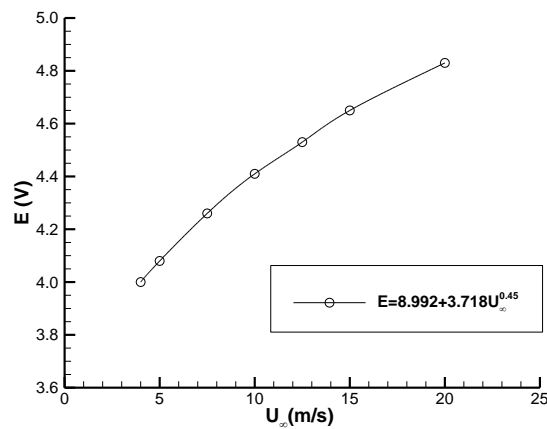
Figure 3.4: A typical hot-wire calibration curve.

The turbulence intensity in the streamwise direction measured by the calibrated hot-wire was presented in Figure 3.5.
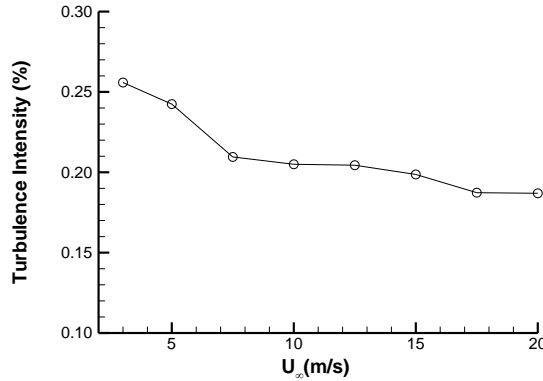
Figure 3.5: Wind tunnel background turbulence level.

The results showed that the empty wind tunnel freestream turbulence intensity is about 0.2% which is at a reasonable level for flow control study.

3.1.2 Flat Plate Model

A flat plate was installed 50 mm above the bottom wall of the test section (Figure 3.6). The plate was designed to develop a TBL. The flat plate is 1390mm in length with a 50mm long trailing edge adjustable flap to form a ZPG TBL. The boundary layer was tripped using a combination of a trip wire of diameter 1.5 mm and a roughness strip of length 30 mm. The trip wire is located 20 mm downstream the plate leading edge and the roughness strip is placed 50 mm downstream the trip wire. This combination ensured a self-preserving TBL upstream of the local plasma jet actuator.

A Scanivalve pressure scanner with 48 ports was employed to measure the static pressure distribution along the flat plate floor for adjusting the required ZPG boundary. Because the static pressures along the flat plate floor are very low, a high accuracy Setra 239 transducer was used in the scanner instead of using the original transducer of the Scanivalve system. The Setra 239 has a range of 0 to 1 inch H_2O (249 P_a) with an accuracy of $\pm 0.14\%$. The measured relative static pressure Δp distributions along the

31

flat plate floor for freestream velocities of 3 m/s, 5 m/s and 10 m/s were shown in Figure 3.7. The results indicate that the required ZPG boundary layer has been formed successfully.
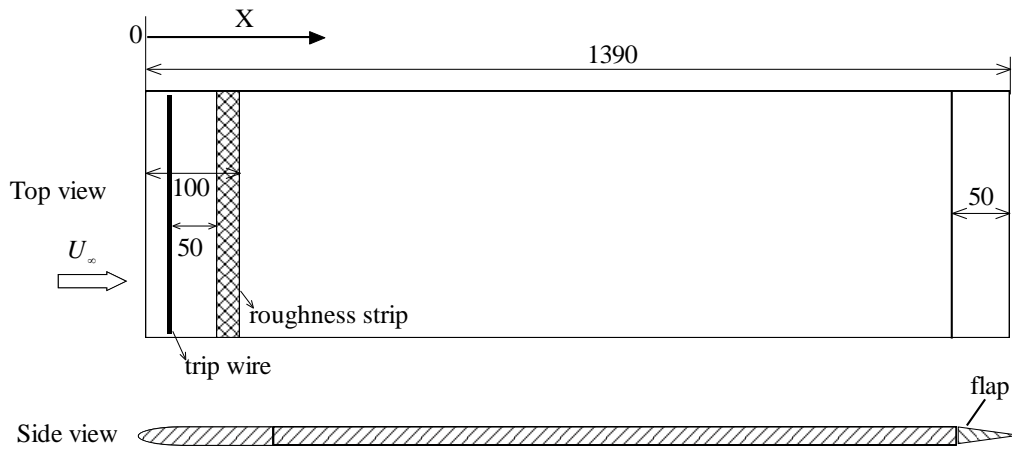
a) Schematic of the flat plate (sketch not to scale).
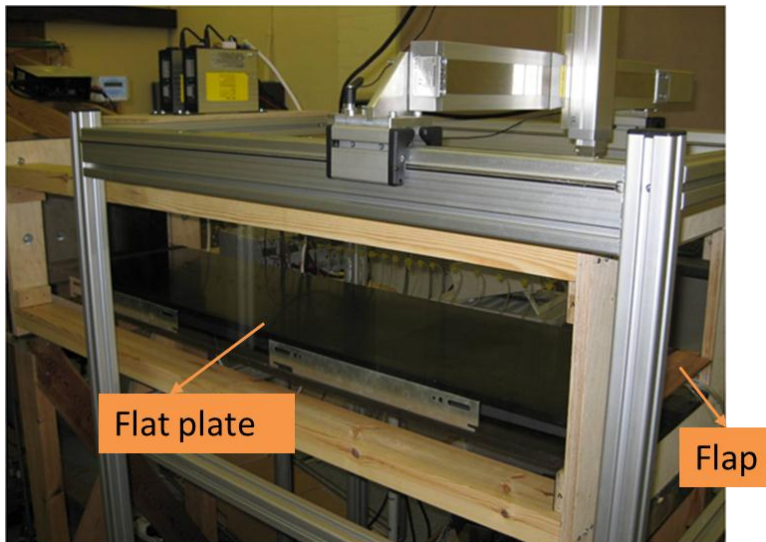
b) The flat plate in the wind tunnel.

Figure 3.6: Boundary layer development flat plate.
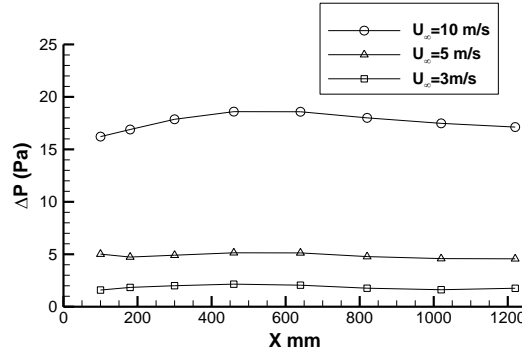
Figure 3.7: Static pressure distribution along the flat plate.

In order to characterize the TBL flow over the flat plate, measurements were conducted using a small glass tube with 0.6 mm in outer diameter. The measurements were taken at spanwise centerline and 1024 mm downstream the flat plate leading edge, where the plasma actuator will be installed. The measurements were conducted at three freestream flow speeds of 5m/s, 10m/s and 15m/s; the corresponding Reynolds number based on the length from the flat plate leading edge to the measurement location is 3.5×10^5, 7.0×10^5 and 10.5×10^5 respectively. The characteristics of the boundary layers were shown in Figure 3.8. The mean velocity profiles shown in Figure 3.8a collapse to a typical ZPG TBL profile for the range of Reynolds numbers tested. The boundary layer mean velocity profiles in inner variable scaling (see Figure 3.8b) exhibit the classic log-law profile of a typical ZPG TBL. A required turbulent boundary has established for our flow control study.

a) **Mean velocity profiles.**   b) **Mean velocity in wall units.**
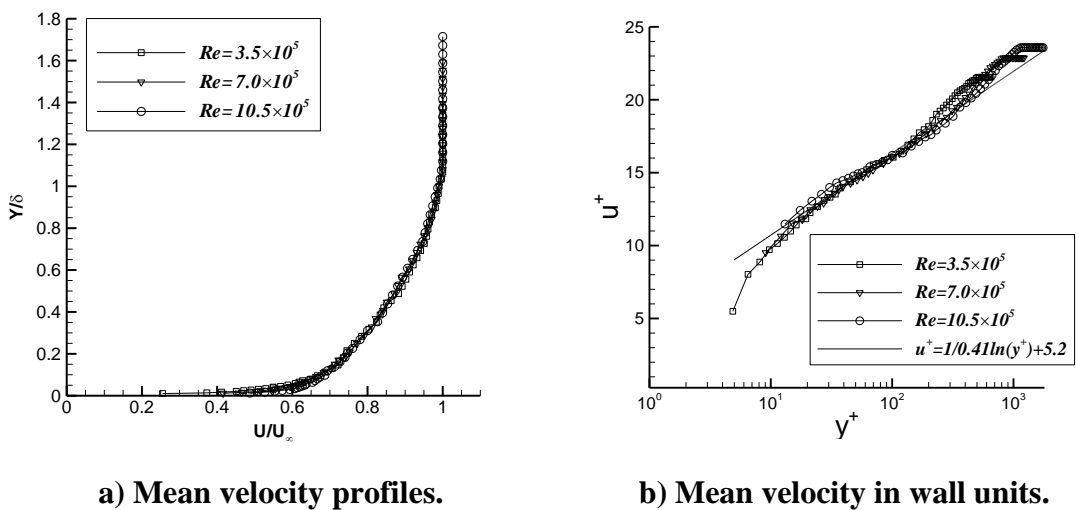
Figure 3.8: Characteristics of the flat plate boundary layer.

33

3.1.3 Plasma Actuator Circuit and Fabrication

To generate glow discharge atmosphere plasma, the air locals to high voltage electrodes should be broken down with a sufficiently high electric field. The applied voltage for sustaining the glow discharge is operating at a few kHz. The power supply system used in this thesis study has a switching circuit topology; see Figure 3.9. The driving signal is a square wave and signal for driving the plasma is generated from a TTi function generator (TG550). The optimal driving frequency for the present plasma actuators is 5 kHz. The optimal driving frequency switches a step up transformer through an insulated gate bipolar transistor (IGBT) and high alternating current AC supply is subsequently output from the step up transformer to induce discharges.
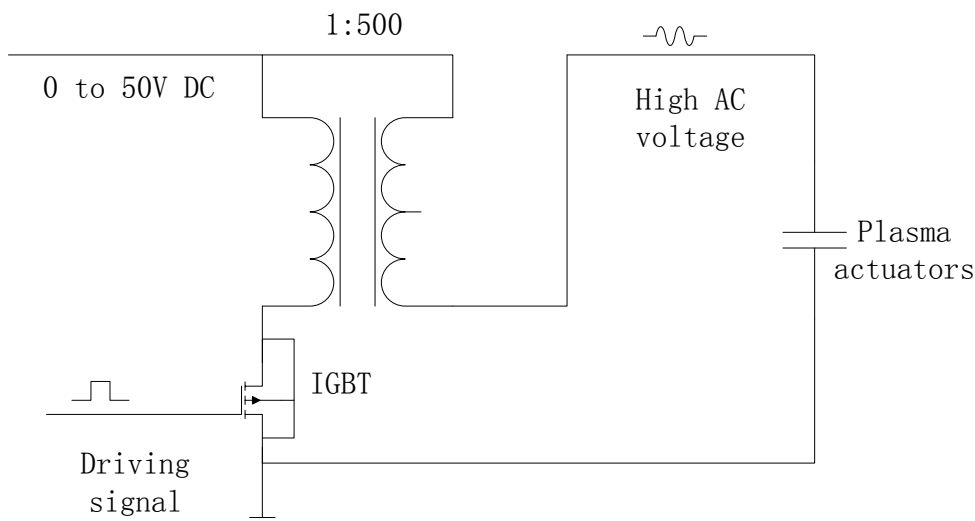
Figure 3.9: Plasma power supply circuit.

The tested plasma actuators were designed using a Perspex board as the dielectric material between the electrodes. All the electrodes were made of the same sized copper strips of 35μm thickness. The width of the electrodes can be easily adjusted. In this study, the width of the exposed electrode was 5mm and that of the encapsulated electrode was 20mm (Figure 3.10).
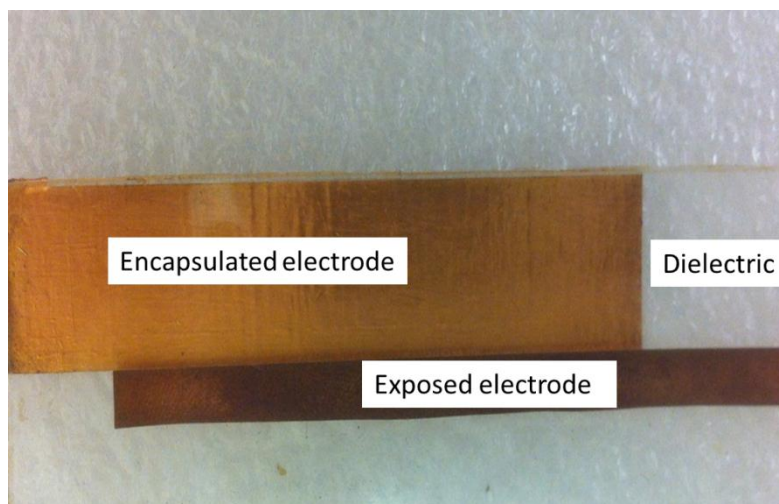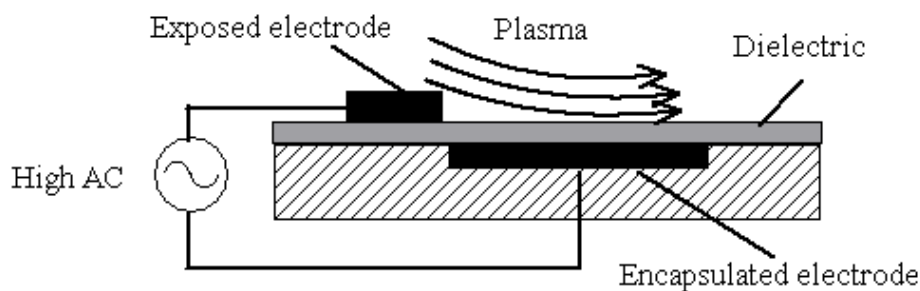
Figure 3.10: Photo of a single DBD actuator.

In order to understand the characteristic of the plasma induced velocity, a typical single DBD actuator was investigated in quiescent air. The DBD actuator is composed of two 35μm copper electrodes flush mounted on a 2mm thick Perspex which served as the dielectric. Both electrodes are 100 mm long. The top air-exposed electrodes are 10 mm wide. There is no gap separating the two electrodes. The grounded electrode is 20 mm wide and encapsulated. The intensity of the glow varies with the input voltage to the actuators: the higher voltages produced a higher intensity glow. The output voltage from the transformer is decided by the input supply voltage. For the initial investigation, the input low DC voltage was set to 20 V, 25V and 30 V. The DC voltage was effectively oscillated at 5.0 kHz across the transformer to generate output voltages in the kilovolt range at the desired frequency. The input power to the transformer can be obtained from the voltage and current output of the DC power supply. The transformer output high voltage was measured using a Testec high voltage probe (TT-HVP 15HF) connected to a Goldstar oscilloscope (type OS-9020A). For the current system, the peak to peak voltage is about 500 times of the input DC voltage. The induced velocity distribution in

the vertical plane was measured using a 0.5mm in diameter Preston tube 30mm away from the anode of the actuator. The maximum induced velocity is increased with the input voltage and achieved at 1~2mm above the surface. The results are shown in Figure 3.11a. The induced velocity distribution along the horizontal direction at Y=1.5mm for AC=25 kV with a 2 mm thick rubber as dielectric is shown in Figure 3.11b. The results were used for a computational model developing to model the potential of plasma actuators to reduce flow-induced noise [104].
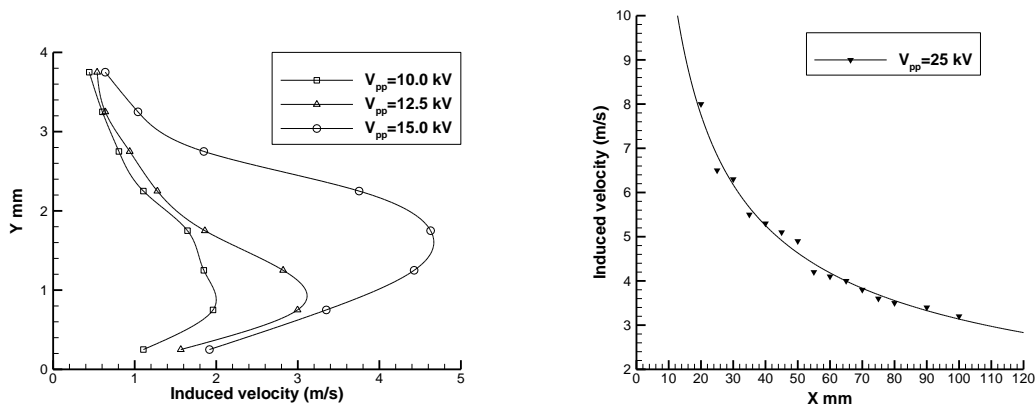
a) Velocity profiles in vertical direction   b) Velocity along horizontal direction

Figure 3.11: Induced velocity profiles by a DBD in quiescent air.

3.1.4 Particle Image Velocimetry

Particle Imaging Velocimetry (PIV) is a non-intrusive measurement technique. It can capture instantaneous flow fields of a common plane with particles lie on. Because PIV captures an entire region of the flow field, the structure of the flow can be detected. The PIV system used in the experiments was a TSI Measurement Systems and incorporates two Gemini Nd:YAG1 lasers by New Wave Research that are capable of running at 16 Hz double-pulse repetition rate, emitting 120 mJ pulses at 532 nm wavelength. A TSI 2048×2048 resolution CCD camera was used and operated in a double frame mode to capture images of the flow field at a sampling frequency of 2 Hz. The lenses available for the CCD camera were Nikon-produced Nikkor 24 mm, 60 mm and 105 mm type f/2.8 lenses. A Safex S195G smoke seeder using Regular DJ Mix Fluid by Martin Manufacturing (UK) Plc. was used to provide seeding for the flow. The typical sizes of the non-spherical particles were 2 μm in diameter. The statistical information of the

flow and its turbulence quantities can be obtained by analysis of the raw velocity vectors PIV provided. The details of the various processing of the raw velocity vectors can be conduct with TSI's software "Insight 3G". The PIV setup is shown in Figure 3.12.
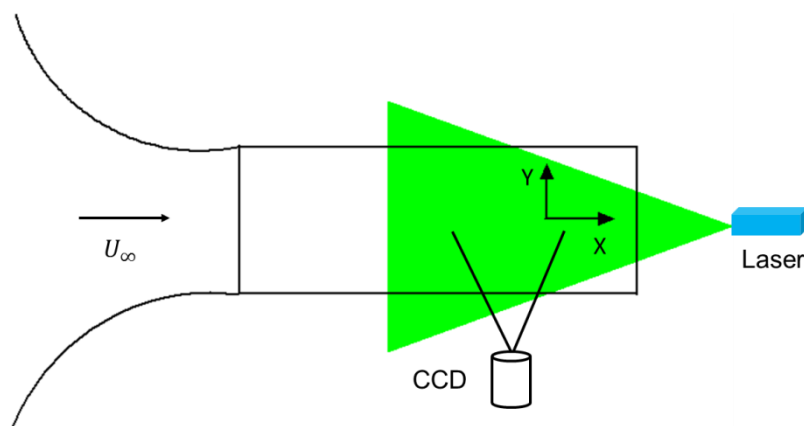
Figure 3.12: A schematic of the PIV system configuration (side view).

A typical boundary layer mean velocity profile obtained from a PIV measurement is compared with the Pitot tube results as shown in Figure 3.13. The freestream velocity is 10 m/s and the measurement was conducted at 1024 mm downstream the flat plate leading edge. The results indicated that, both measurement methods compare well with each other.
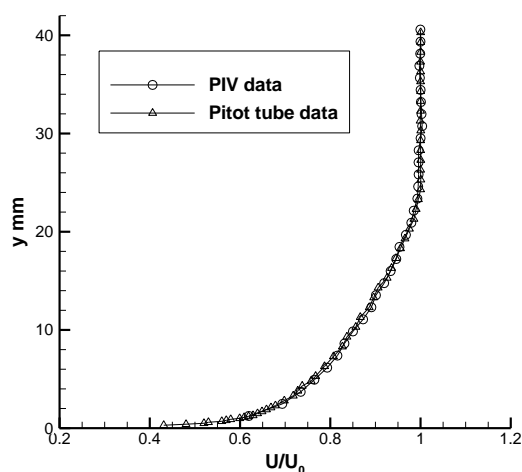
Figure 3.13: Comparison of different measurement methods (U_∞=10m/s).

3.1.5 Error and Uncertainty

The two components of the velocity field were measure by a TSI 2D PIV system in this study. Images of the flow field are captured using a CCD camera. The images are correlated to determine the displacements of the seeding particles which are eventually represented as velocity vectors. The errors and uncertainties were estimated based on the mathematical derivation by Maina [103].

The error in the velocity is defined by:

$$\varepsilon_U = \frac{p_c \gamma S_f}{\Delta t} \tag{3.1}$$

The scale factor S_f is obtained experimentally and represents the number of pixels per unit displacement, for a typical experimental, the parameters for the PIV measurement were as below; the scale factor S_f=9.9, the time between laser pulses Δt=60μs, The CCD resolution γ=6.7μm is determined by the hardware and is fixed and the correlation peak p_c =0.1. The uncertainty in the velocity for an instantaneous vector is then estimated to be 0.1m/s.

The positional error of the vectors on a PIV vector map is depends on the resolution of the CCD camera γ and the scale factor S_f :

$$\epsilon_x = \epsilon_y = \gamma S_f \tag{3.2}$$

And then the uncertainty in the position of the vector is then estimated to be 0.07 mm both in the streamwise and vertical axis.

3.2 Results of Jet Blowing from the Downstream Slot

3.2.1 Jet Actuation without External Flow

The flat plate together with the designed actuator was installed 50 mm above the bottom wall of the test section (Figure 3.14). The origin of the measurement coordinate system was located at 1024mm downstream of the plate leading edge, which is the centre of the two slots' of the actuator. Because the distance between the actuator two slots may different, we define another parameter ΔX refer to the streamwise distance from the downstream slot as shown in Figure 3.14.
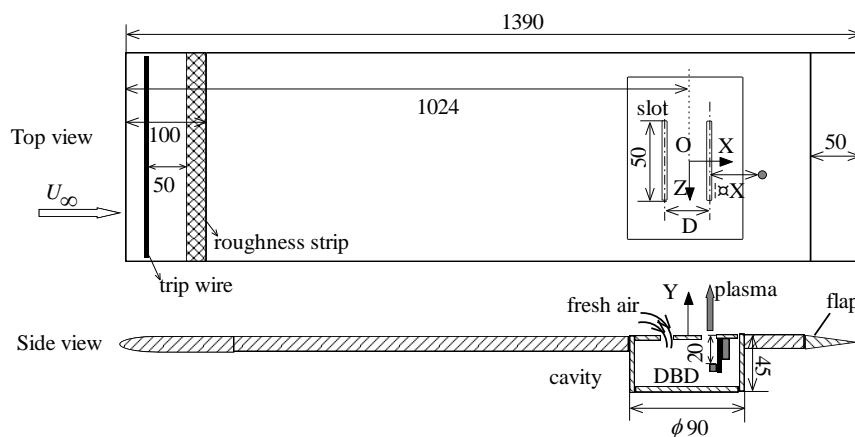
a) Flat plate with the installed actuator

b) Photo of the actutor

Figure 3.14: Boundary layer development flat plate and actuator.

A schematic of the DBD based plasma vertical jet actuator is also shown in Figure 3.14. The actuator is composed of a circular cavity, a thin flat plate cavity cover with two parallel slots and a normal DBD actuator. The width of both slots is 3 mm. The DBD actuator was vertically mounted under the downstream slot, the distance from the exposed electrode edge to the surface of the flat plate was 20mm. Before conducting the boundary layer flow control tests, the velocity field induced by the newly designed plasma jet actuator in quiescent air was measured using PIV. The DBD actuator in the cavity was operated in a steady 5 kHz square wave mode with the applied high AC voltage of 18.5kV peak-to-peak. Figure 3.15 shows the induced flow field from an ensemble average of 300 image pairs. The result shows the fundamental features of the designed vertical jet actuator. In the ambient air, a vertical jet is generated from the slot under the DBD actuation in the cavity. Meanwhile, the supply fresh air is sucked into the cavity from the air supply slot. The effect of suction is far weaker than the effect of blowing. So the produced vertical jet is very similar to a continuously blowing jet. But unlike a normal blowing jet, the induced plasma jet is still a zero net mass flux jet (or synthetic jet) as there is no mass flow been added into the flow field. On the other hand, because the induced plasma jet is a continuously blowing steady jet, it is also different from a traditional alternative blowing and suction synthetic jet. As such, the designed DBD based jet actuator is different from either a mass injection blowing jet actuator or a traditional diaphragm based synthetic actuator.

a) velocity field   b) vorticity field
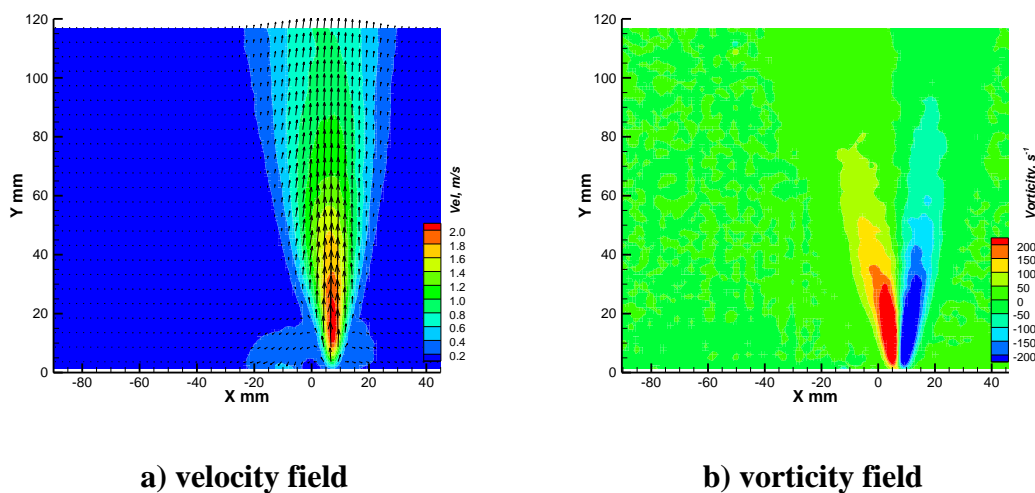
Figure 3.15: Actuator induced velocity field in ambient air.

3.2.2 Turbulent Boundary Layer Actuation

The effects of the induced spanwise jet actuation on the ZPG TBL over the flat plate were also measured non-intrusively using the TSI PIV system. The PIV measurement X-Y plane was over the spanwise centerline of the actuator slots. The results presented here for the jet blowing from the downstream slot were conducted at freestream velocities ranging from 3.0m/s to 10.0m/s ($Re_x = 2.1 \times 10^5$ to $Re_x = 7.0 \times 10^5$). The effects of different applied high AC voltages and slot locations were also investigated.

3.2.2.1 Effects of the Actuator Applied Voltage

The induced jet velocities from the cavity are different at different applied high AC voltages. A higher applied voltage will result in higher ionic wind output from the slot into the quiescent air or flow field. The effects of applied voltages were first studied with two applied high AC voltages (V_{pp}=15 kV and V_{pp}=18.5 kV) over the TBL at a freestream velocity of 5 m/s. The TBL characteristics measured 20mm downstream of the actuator jet blowing slot are compares with the baseline case (no actuation) in Figure 3.16, and boundary layer parameters are summarized in table 3.1.

| a) Mean velocity profiles | b) Turbulence intensity profiles |
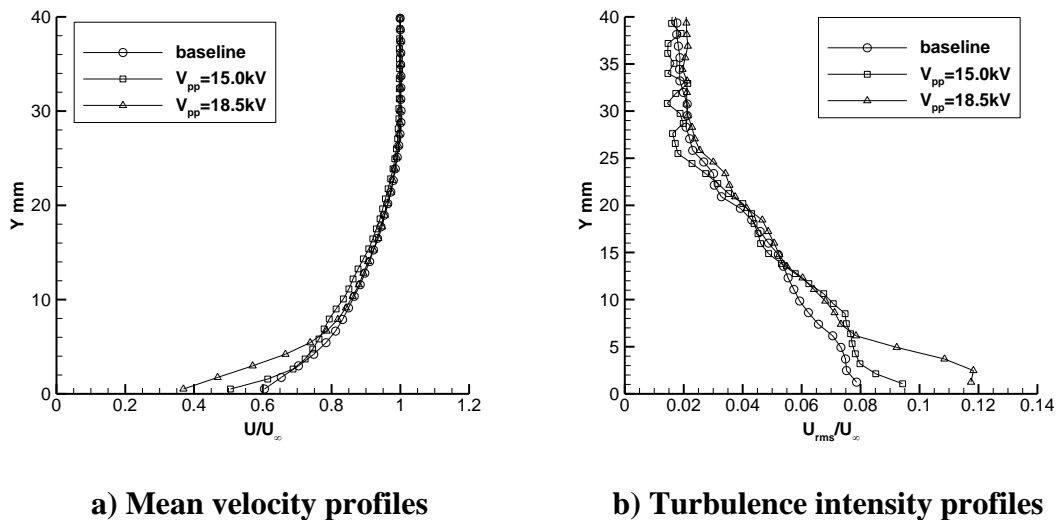
Figure 3.16: Effects of different applied voltages (U_∞=5 m/s, ΔX=20mm).

41

Figure 3.16a indicate that the effect on the boundary layer mean velocity profile increases with the applied voltage. The results showed in the Table 3.1 indicate that actuation at V_{pp}=18.5 kV increase the 99% boundary-layer thickness by 9.7% when compared with the plasma-off case. The momentum thickness and displacement thickness are increased by 6.6% and 26% respectively. This resulted in a velocity profile shape factor increased from 1.29 to 1.52. As to the applied voltage of 15 kV, the increments of the boundary layer thickness, displacement thickness and shape factor are smaller than that of 18.5 kV, but the momentum thickness is increased byu 10.4% compared to 6.6% of 18.5 kV. The results suggest that the changes of the boundary characteristics are different at different applied voltage.

Table 3.1: Boundary layer characteristics at different applied voltages (ΔX=20mm).

Applied voltage	δ, mm	δ^*, mm	θ, mm	H
V_{pp}=0	25.8	3.47	2.69	1.29
V_{pp}=15.0 kV	26.5	4.03	2.97	1.36
V_{pp}=18.5 kV	27.1	4.38	2.88	1.52

The corresponding streamwise-component turbulence intensity profiles for the spanwise actuation of the flat plate TBL are shown in Figure 3.16b. The actuation results in increasing near wall turbulence intensity for both of the applied high AC voltages. For the case of V_{pp}=18.5 kV actuation, the turbulence intensity increase in the boundary layer is bigger than that of 15 kV actuation. This is because of the spanwise vorticity injection by the plasma jet is decreased with less applied voltage.

3.2.2.2 Effects along the Streamwise Direction

The effect of the plasma jet actuation on the ZPG boundary layer along the streamwise direction was investigated at a freestream velocity of 5 m/s ($Re_x = 3.5 \times 10^5$). The mean velocity and vorticity field are shown in Figure 3.17. The boundary layer characteristics obtained from the PIV measurements at five typical positions along the

streamwise direction are plotted in Figure 3.18. The undisturbed baseline case from the plasma off case measurement is included also plotted for comparison.

According to Figure 3.17a, the velocity profile near the jet blowing slot is changed by the actuation. Figure 3.17b indicates that the blowing slot downstream near wall vorticity is increased. Figure 3.18a shows the mean streamwise velocity profiles at five streamwise positions together with the baseline case without actuation. It should be noted that, because the undisturbed velocity profile is almost the same in the compared region due to the well-developed ZPG TBL condition, just one baseline profile is plotted. In the disturbed mean velocity profiles near the blowing slot (ΔX=5, 10 mm), especially at ΔX=5 mm, an accelerated flow region appears and affects about 25% of the boundary layer region. Whereas at ΔX=10 mm, the regions close the wall and in the upper 25% part of the boundary layer thickness seem to be less affected by the blowing jet and the accelerated flow becomes weaker. At $\Delta X \geq 20$ mm, the boundary layer near wall flow is retarded and the retarded flow become weaker with the increasing distance. The retarded flow velocity profiles converge towards the undisturbed baseline case. This retarded flow is similar in characteristic to a localized injection into a ZPG boundary layer with skin friction reduction [105].

a) Mean velocity   b) Mean vorticity
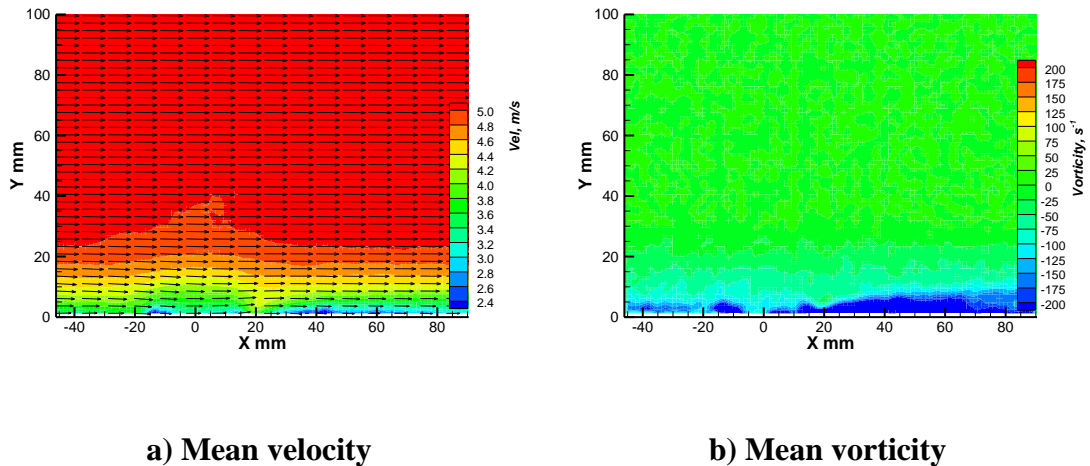
Figure 3.17: PIV measurement at U_∞=5 m/s, V_{pp}=18.5 kV.

Table 3.2: Boundary layer characteristics along the flat plate.

case	δ, mm	δ^*, mm	θ, mm	H
baseline	25.8	3.47	2.69	1.29
ΔX=5mm	28.3	2.91	2.44	1.19
ΔX=10mm	27.6	3.30	2.60	1.27
ΔX=20mm	27.1	4.38	2.88	1.52
ΔX=40mm	26.7	4.56	3.08	1.48
ΔX=60mm	25.8	4.32	3.04	1.42

The turbulent boundary layer characteristics along the *X* direction under the actuation are summarized in Table 3.2. In the vicinity of plasma jet blowing slot (ΔX=5, 10 mm), the boundary layer displacement thickness, the momentum thickness and the shape factor are all reduce. However at ΔX=10 mm, the changes of the boundary layer parameters are very small compared to the baseline case. After this position, the retarded flow results in an increment of the displacement thickness, the momentum thickness and the shape factor and the effect of blowing gradually decreases with the increasing distance from the blowing slot.

a) **Mean velocity profiles**   b) **Turbulence intensity profiles**
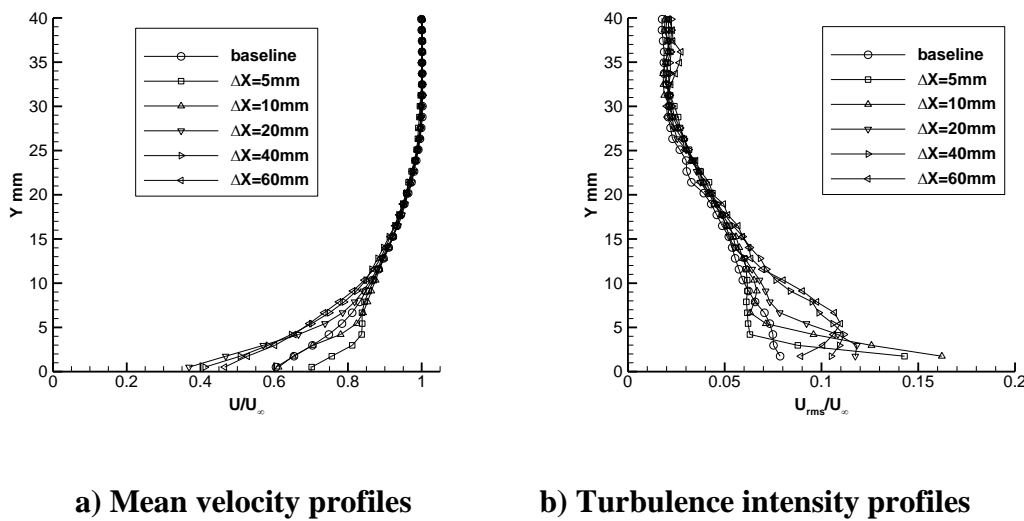
Figure 3.18: Boundary layer characteristics at different streamwise positions (U_∞=5 m/s, V_{pp}=18.5 kV).

The effects of the plasma jet actuation on the boundary layer turbulence intensity are shown in Figure 3.18b. The turbulence intensities along the streamwise direction are significantly modified by the blowing jet. Just downstream the blowing slot (ΔX=5 mm), the turbulence intensity increases in the near wall region, and then decreases, followed by a recovery to the undisturbed value. The near wall turbulence intensity increases under the actuation when $\Delta X \geq$20 mm.

3.2.2.3 Effects of Reynolds Numbers

The effects of *Re* on the velocity and vorticity field of the same actuation are shown in Figures 3.19 and 3.20. The mean velocity and vorticity fields suggest that the effect of induced plasma jet actuation becomes weaker with increasing Reynolds number. For the velocity fields, at $Re_x = 2.1 \times 10^5$ (U_∞=3 m/s), Figure 3.19a shows that the boundary layer profiles upstream, above and downstream of the actuation are been changed significantly; a large increment in boundary layer thickness can be observed over the two slots area. When Reynolds number is increased to 7.0×10^5 (U_∞=10 m/s), a slight change can be found above the jet blowing area; downstream of the blowing slot, there is almost no change in the boundary layer. At $Re_x = 2.1 \times 10^5,\ 3.5 \times 10^5$ (U_∞=3, 5 m/s), Figure 3.17b and Figure 3.19b show clear vorticity increment just downstream of the blowing slot, whereas at $Re_x = 7.0 \times 10^5$ (U_∞=10 m/s), there is no visible vorticity changes (Figure 3.20b).

a) Mean velocity   **b) Mean vorticity**
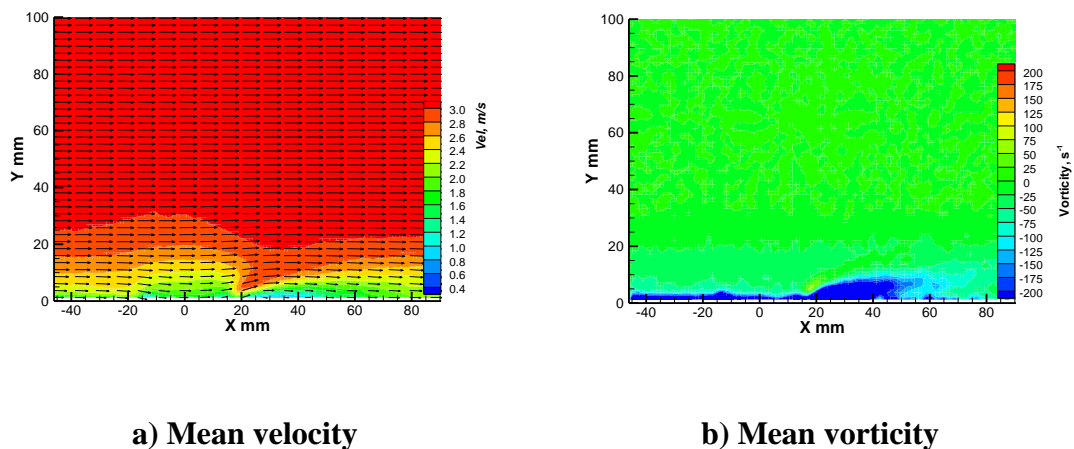
Figure 3.19: PIV measurement at U_∞=3 m/s, V_{pp}=18.5 kV.

a) Mean velocity   **b) Mean vorticity**
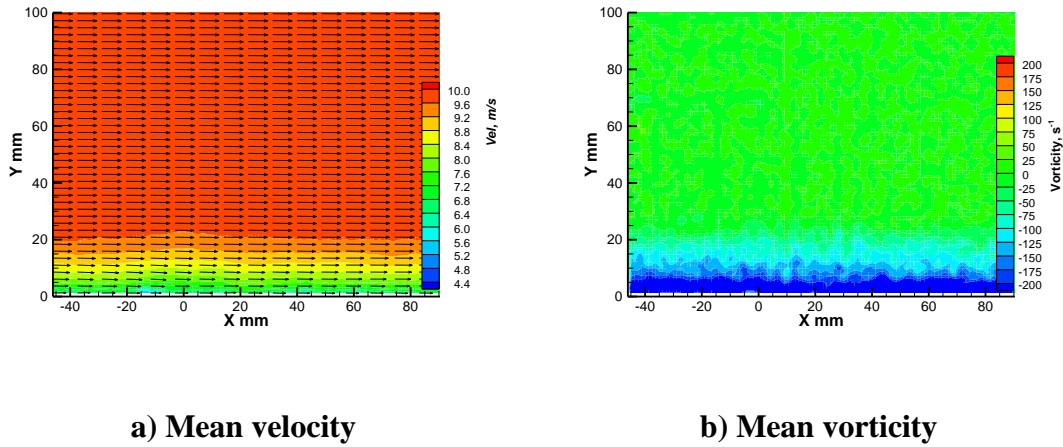
Figure 3.20: PIV measurement at U_∞=10 m/s, V_{pp}=18.5 kV.

In order to clarify the effect of actuation at different Reynolds numbers in detail, the disturbed TBL velocity and turbulence intensity profiles at 20mm downstream of the actuator blowing slot at different Reynolds number are plotted together with the corresponding baseline values in Figures 3.21-3.23. With the increase of Reynolds number, the influence on the boundary layer velocity profiles and turbulence intensity profiles both reduces. At $Re_x = 2.1 \times 10^5$ (U_∞=3 m/s), as shown in Figure 3.21a, the boundary layer velocity profile is changed significantly. The disturbed boundary layer near wall velocity is delayed but accelerated in the region of Y/δ=0.23 to 0.6. The turbulence intensity is increased by more than 300% in the near wall region and the increment can be found at 70% of the boundary layer thickness (Figure 3.21b). When the Reynolds number is increased to 7.0×10^5 (U_∞=10 m/s), under the applied actuation condition, the effect of the actuation on the boundary layer is very small (Figure 3.23).

a) Mean velocity   **b) Turbulence intensity**
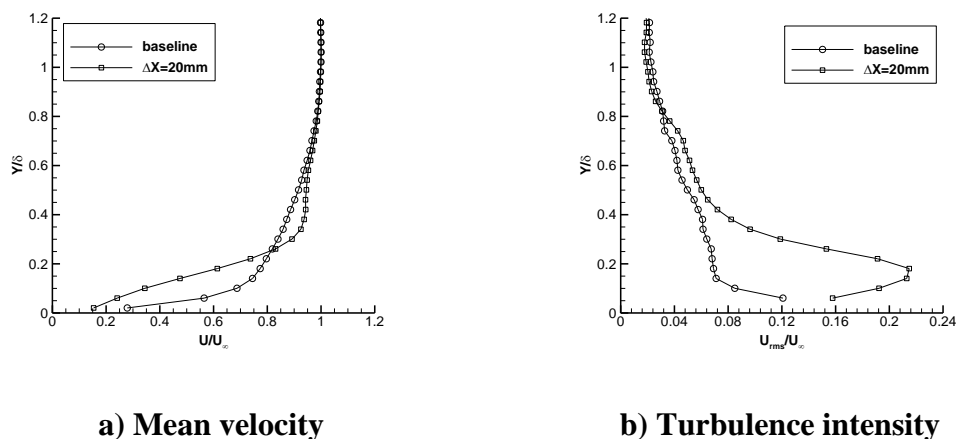
Figure 3.21: Boundary layer characteristics at U_∞=3 m/s, V_{pp}=18.5 kV.

a) Mean velocity   **b) Turbulence intensity**
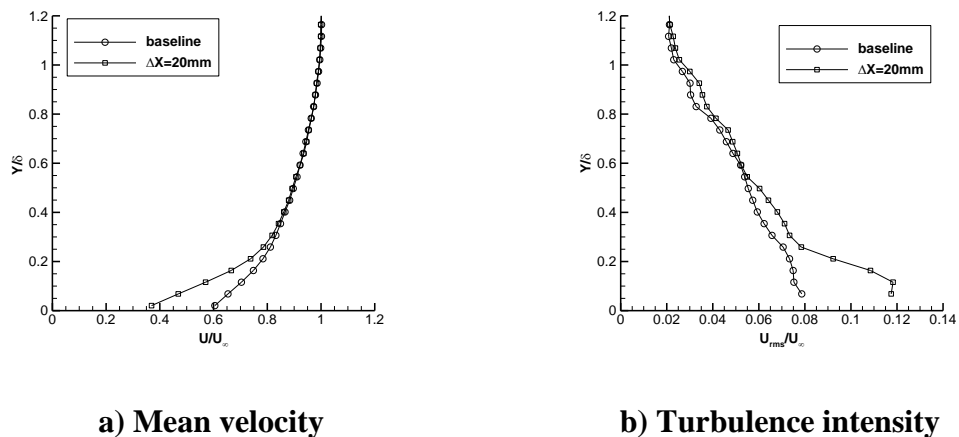
Figure 3.22: Boundary layer characteristics at U_∞=5 m/s, V_{pp}=18.5 kV.

a) Mean velocity   **b) Turbulence intensity**
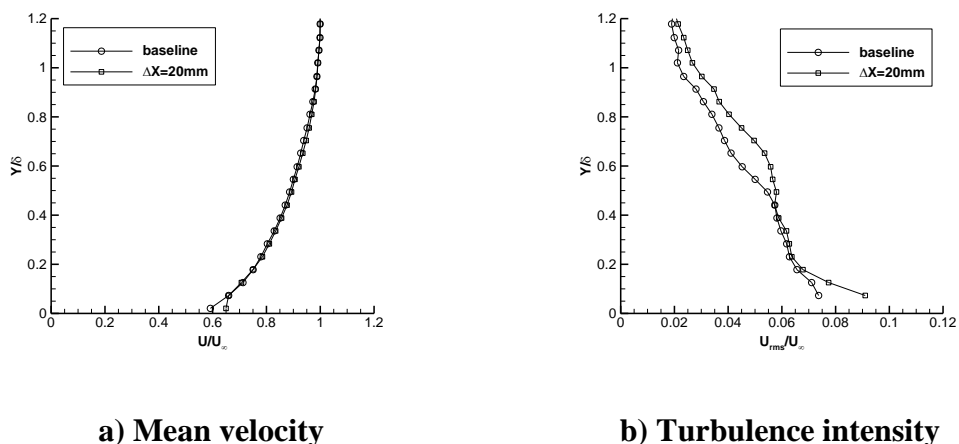
Figure 3.23: Boundary layer characteristics at U_∞=10 m/s, V_{pp}=18.5 kV.

47

The variation of boundary layer characteristics of the flat plate TBL at the same downstream location at different Reynolds number is summarized in Table 3.3.

Table 3.3: Effects at different Reynolds number

Reynolds number	case	δ, mm	δ^*, mm	θ, mm	H
$Re_x = 2.1 \times 10^5$	baseline	30.7	4.18	2.82	1.48
	ΔX=20mm	30.3	5.32	2.51	2.12
$Re_x = 3.5 \times 10^5$	baseline	25.8	3.47	2.69	1.29
	ΔX=20mm	27.1	4.38	2.88	1.52
$Re_x = 7.0 \times 10^5$	baseline	23.4	3.21	2.51	1.28
	ΔX=20mm	23.4	3.38	2.61	1.30

At the measurement location, the disturbed boundary layer displacement thickness, the momentum thickness and the shape factor increments are reduced with the increase of Reynolds number. At $Re_x = 2.1 \times 10^5$ (U_∞=3 m/s), the shape factor is increased from 1.48 to 2.12. But for $Re_x = 7.0 \times 10^5$ (U_∞=10 m/s), the actuation has little impact on the boundary layer parameters and the shape factor just increased from 1.28 to 1.30. The results indicated that the effects of the plasma actuation at high *Re* is small, work should be done in the future to improve its authority for practical flow control applications.

3.2.2.4 Effect of Air Supply Slot Location

Two separation distances (15mm and 30mm) between the air supply slot and jet blowing slot were tested. A typical result at U_∞=5m/s and ΔX=20mm is shown in Figure 3.24. The results indicate that the effects on the characteristics of the boundary layer by both actuators with different separation distance are similar. The actuation of the actuator has little association with the upstream air supply slot location. This is because the upstream slot just serves as the unionized fresh air supply and the fresh air suction velocity is far slower compares to the plasma driven blowing velocity as shown in

Figure 3.24. The results indicate that effect of the designed actuator actuation mainly depends on the plasma induced jet; it can therefore be concluded that fresh air supply slot design can fit the required operating condition flexibly. This is a helpful finding for flow control applications.

a) Mean velocity profiles   b) Turbulence intensity profiles
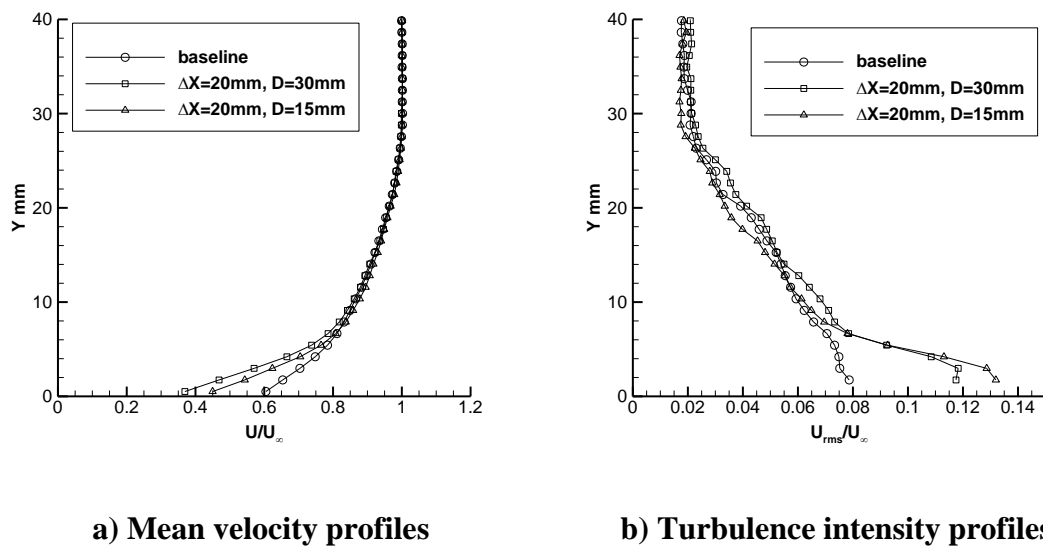
Figure 3.24: Effects of distance between the two slots of the actuator.

3.3 Results of Jet Blowing from the Upstream Slot

3.3.1 Jet Actuation without External Flow

The actuator configuration for induced jet blowing from the upstream slot together with the boundary layer flat plate was shown in Figure 3.25. The coordinate system and the ΔX definition were also shown in Figure 3.25.
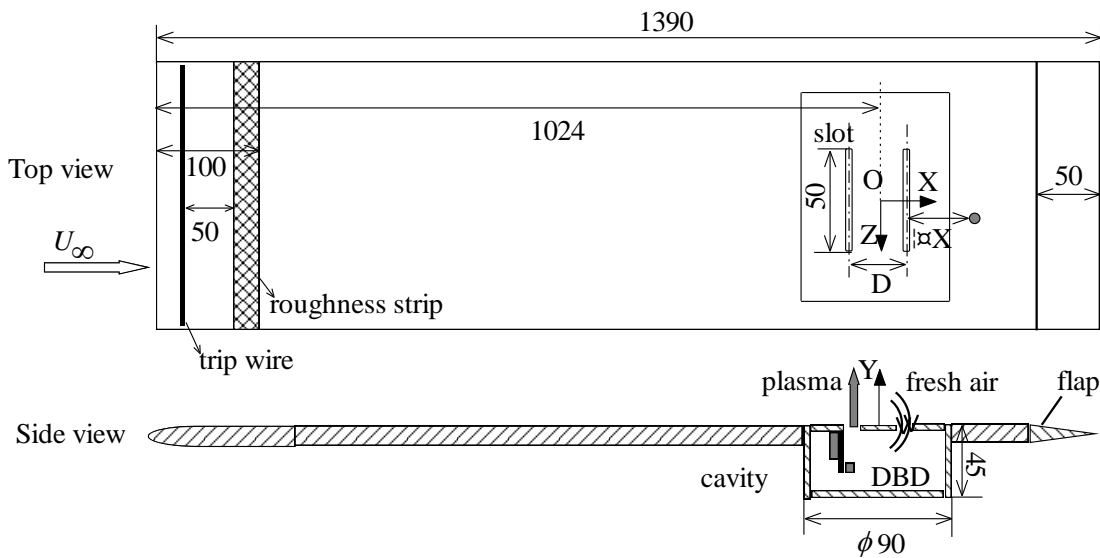
Figure 3.25: Upstream blowing plasma based jet actuator (sketch not to scale).

The DBD based upstream blowing plasma jet actuator showed in Figure 3.25 has the same structure and components as described in section 3.2.1.

The velocity field induced by the upstream blowing plasma jet actuator in quiescent air is shown in Figure 3.26. The DBD actuator in the cavity was operated in a steady 5 kHz square wave mode with the applied high AC voltage of 18.5kV peak-to-peak. The induced flow field was obtained from an ensemble average of 300 image pairs of PIV measurement. Because there is just blowing from different slot location, the induced velocity field is nearly the same as the jet blowing from the downstream slot with the same DBD actuation.

a) Velocity field   b) Vorticity field
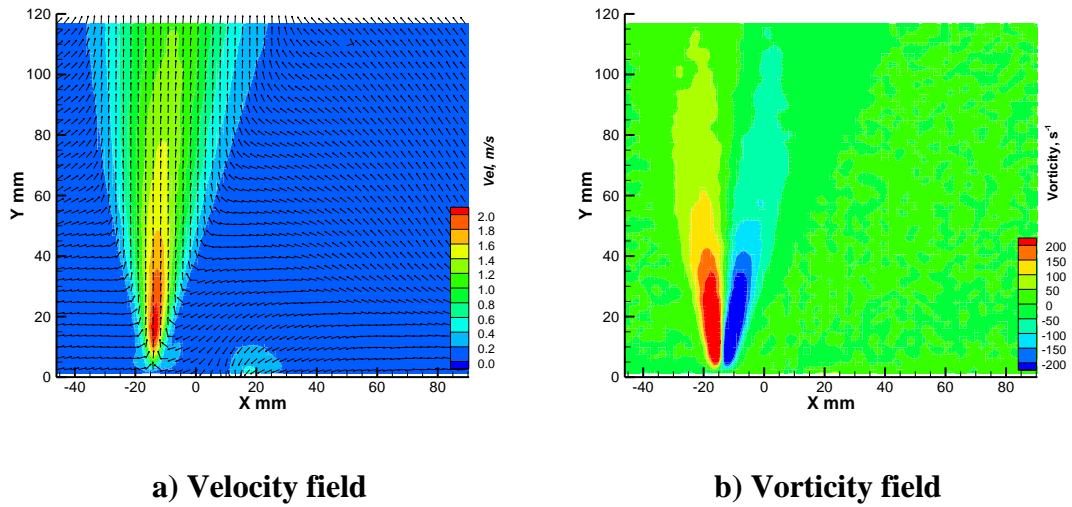
Figure 3.26: Upstream blowing actuator induced velocity field in ambient air.

3.3.2 Turbulent Boundary Layer Actuation

The effects of the induced upstream blowing jet actuation on the ZPG TBL over the flat plate were also measured non-intrusively using the TSI PIV system. The results presented here for the jet blowing from the downstream slot were also conducted at freestream velocities U_∞=3.0 m/s, 5 m/s and 10.0 m/s ($Re_x = 2.1 \times 10^5$, $Re_x = 3.5 \times 10^5$, and $Re_x = 7.0 \times 10^5$).

3.3.2.1 Effects along the Streamwise Direction

The effect of the upstream blowing actuation on the ZPG boundary layer along the streamwise direction was investigated at a freestream velocity of 3 m/s ($Re_x = 2.1 \times 10^5$). The mean velocity and vorticity field are shown in Figures 3.27 and 3.28. The corresponding downstream slot blowing case is also shown for comparison.

According to Figure 3.27, the large changes of the velocity profiles both occur near the jet blowing slot. The main differences between the two cases are the boundary layer profile changes upstream and above the actuators. At a certain distance downstream the jet blowing slot, the modified boundary layer flows become similar. The near wall turbulence intensity increase just downstream the blowing slot can be found for both

cases; but the vorticity levels are decreased from 25mm downstream the blowing slot for the two actuations (Figure 3.28).

a) Upstream slot blowing   **b) Downstream slot blowing**
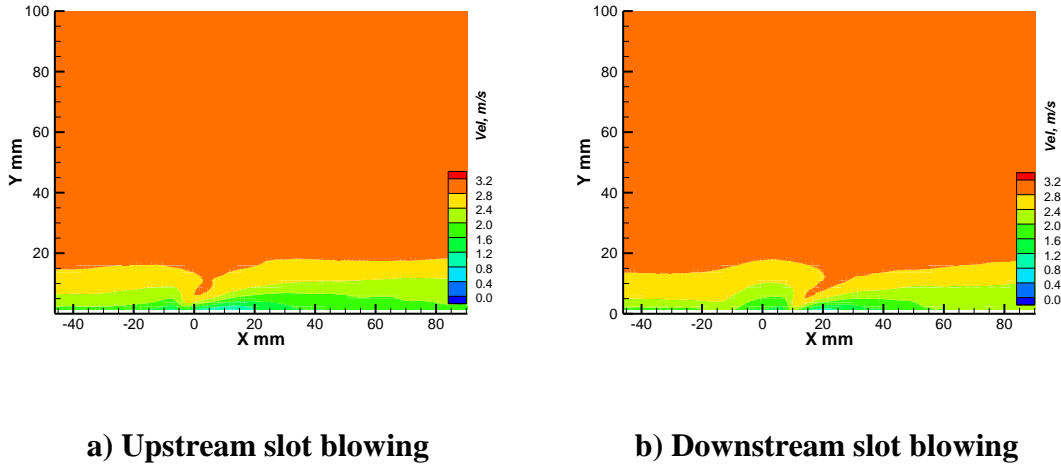
Figure 3.27: Comparison of mean velocity flow field (U_∞=3 m/s, V_{pp}=18.5 kV).

a) Upstream slot blowing   **b) Downstream slot blowing**
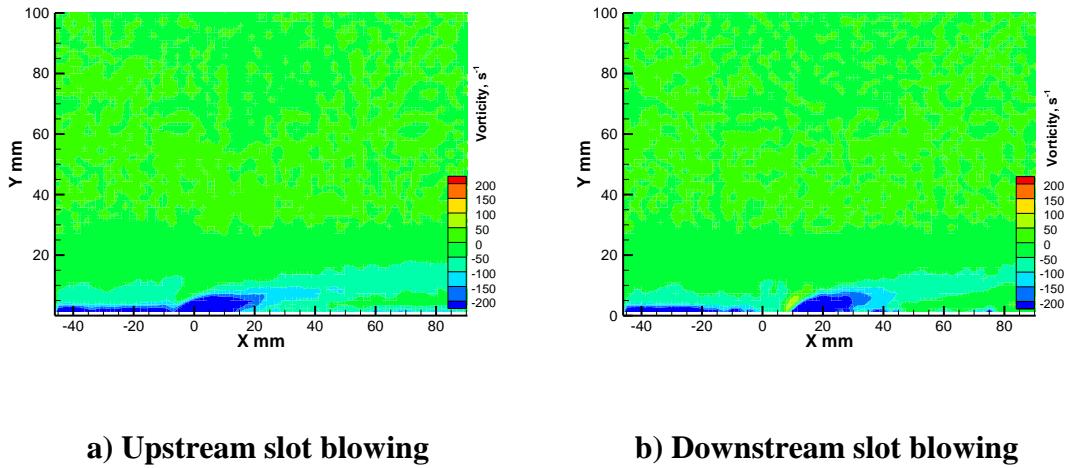
Figure 3.28: Comparison of mean vorticity flow field (U_∞=3 m/s, V_{pp}=18.5 kV).

The boundary layer characteristics at a typical position of ΔX=40 mm are plotted for both the upstream and the downstream slot blowing, as shown in Figures 3.29 and 3.30. The boundary layer near wall flow is retarded for both cases but the retarded flow for the upstream slot blowing is weaker than the downstream slot blowing case. This is due to the actual distance from the blowing slot is relative longer for the upstream slot

blowing. The characteristics of the modified near wall turbulence intensity are similar for both cases. The increment of the turbulence intensity under the upstream slot blowing actuation is smaller compare to the downstream slot blowing.

a) Upstream slot blowing   b) Downstream slot blowing
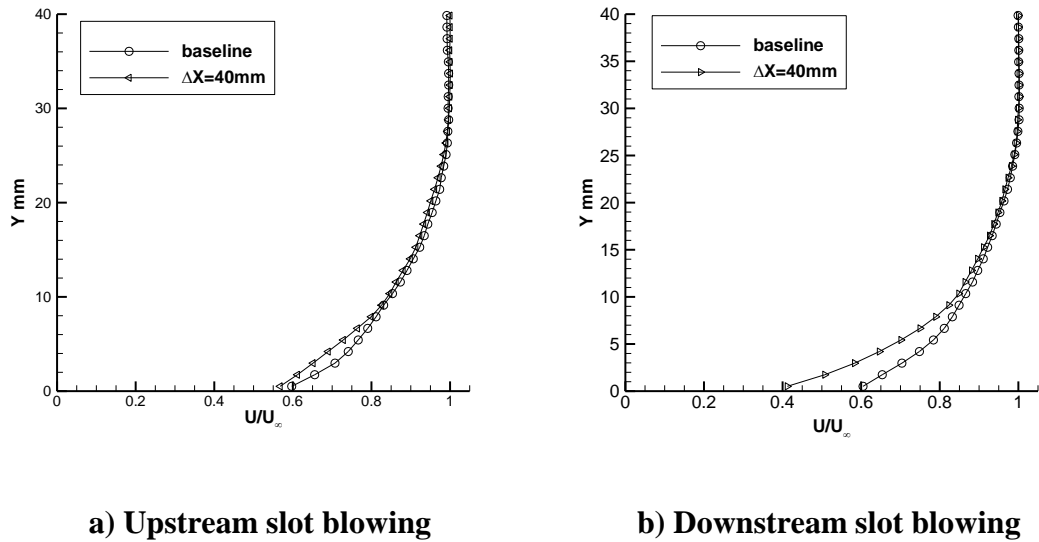
Figure 3.29: Comparison of mean velocity profiles (U_∞=3 m/s, V_{pp}=18.5 kV).

a) Upstream slot blowing   b) Downstream slot blowing
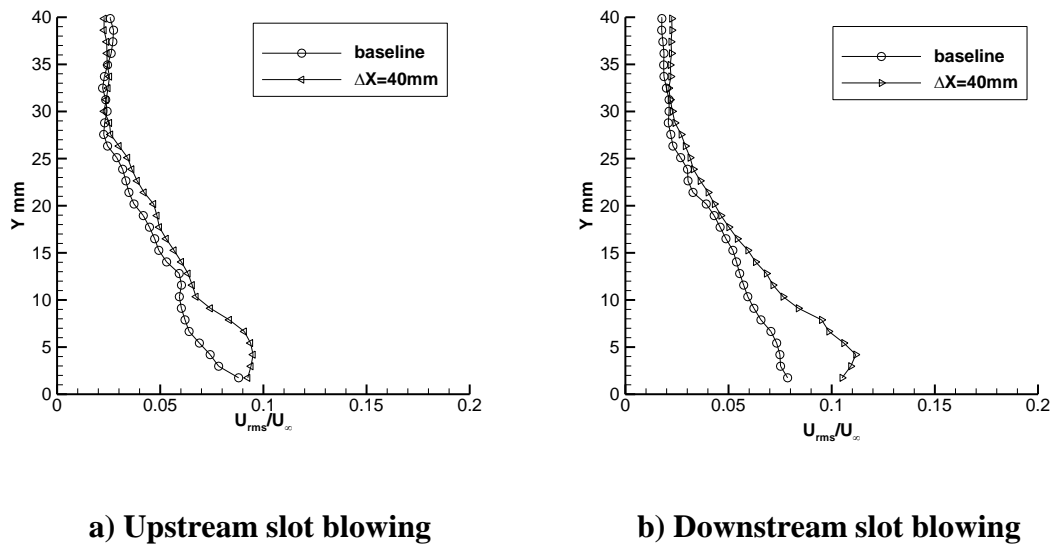
Figure 3.30: Comparison of turbulent intensity profiles (U_∞=3 m/s, V_{pp}=18.5 kV).

3.3.2.2 Effects of Reynolds Number

Figures 3.31 to 3.33 show the disturbed TBL velocity and turbulence intensity profiles 20mm downstream the actuator air supply slot at different Reynolds numbers. The influences on the boundary layer velocity profiles and turbulence intensity profiles are both decreased with the increase of Reynolds number. The plasma actuator was operated at V_{pp}=18.5 kV. At $Re_x = 2.1 \times 10^5$ (U_∞=3 m/s), as shown in Figure 3.31a, the boundary layer velocity profile is changed significantly. The disturbed boundary layer near wall velocity is delayed 50% of the boundary layer thickness. The turbulence intensity is increased by more than 200% at 20% of the boundary layer thickness (Figure 3.31b). When the Reynolds number increased to 7.0×10^5 (U_∞=10 m/s), under the applied actuation condition, the effect of the actuation on the boundary layer is very small (Figure 3.33).

a) Streamwise mean velocity   b) Streamwise turbulence intensity
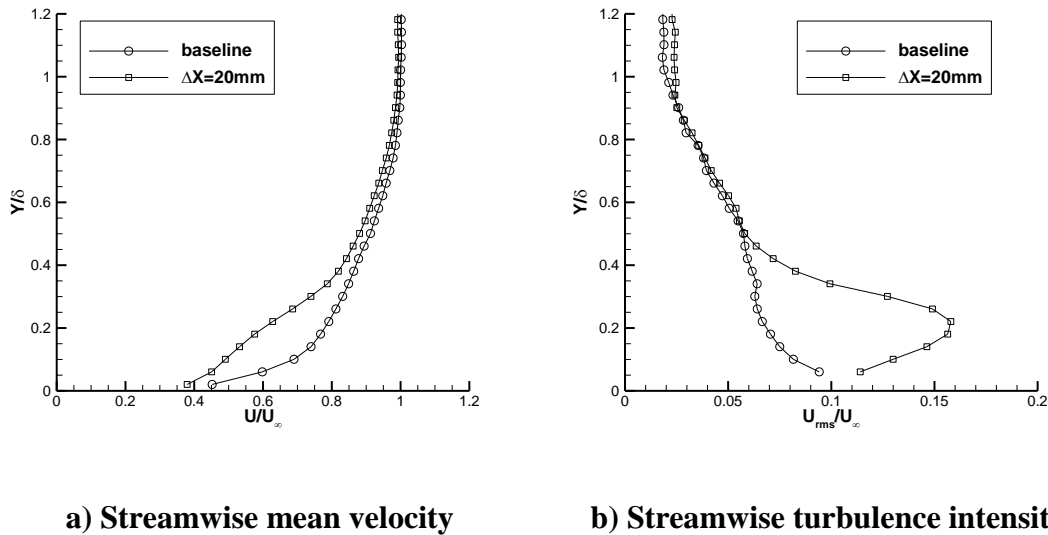
Figure 3.31: Effects of upstream slot blowing at U_∞=3 m/s.

a) Streamwise mean velocity   **b) Streamwise turbulence intensity**
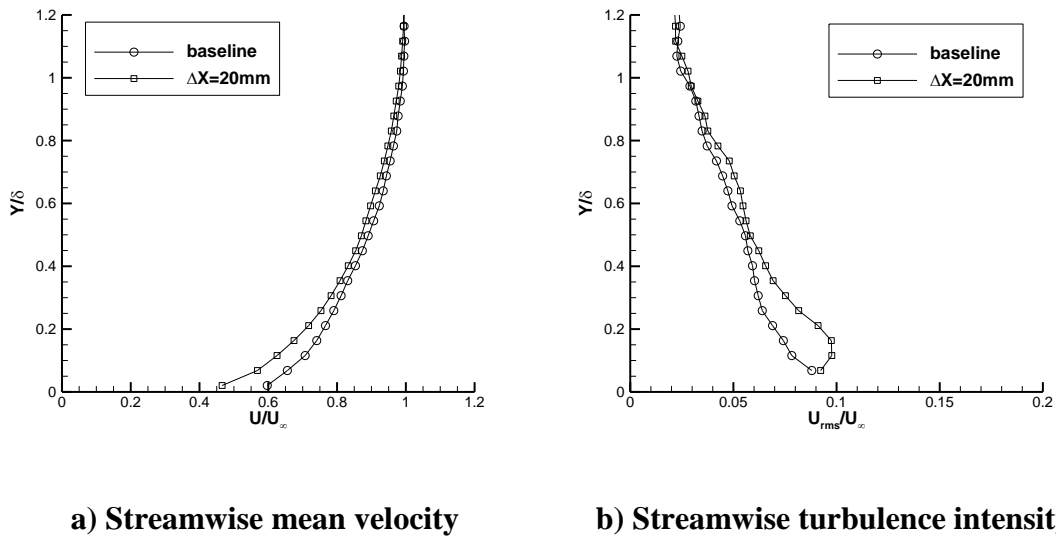
Figure 3.32: Effects of upstream slot blowing at U_∞=5m/s.

a) Streamwise mean velocity   **b) Streamwise turbulence intensity**
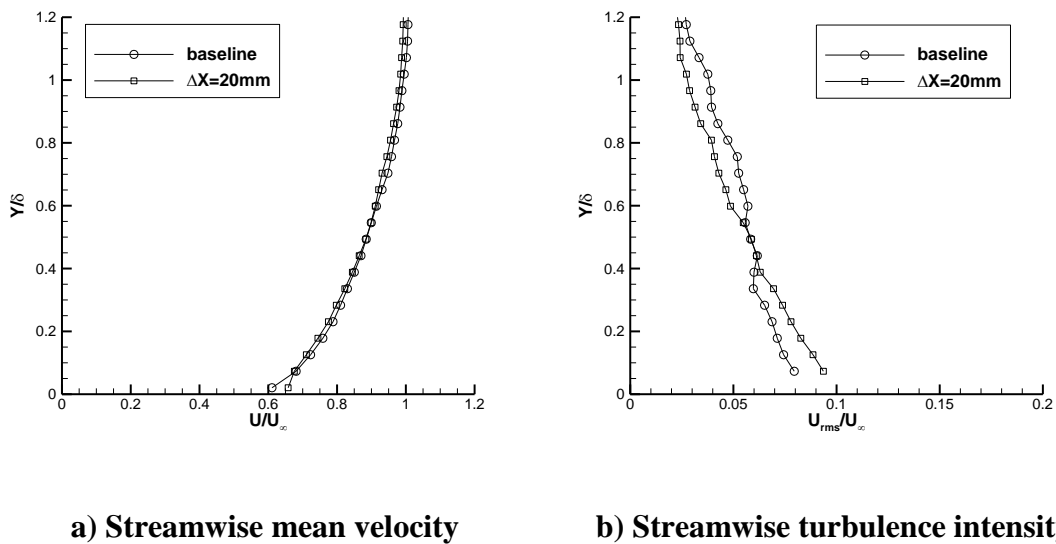
Figure 3.33: Effects of upstream slot blowing at U_∞=10 m/s.

55

3.3.2.3 Effect of Air Supply Slot Location

Two separation distances (15mm and 30mm) between the air supply slot and jet blowing slot were also tested. A typical result at U_∞=5m/s and ΔX=20mm is shown in Figure 3.34. The results indicate that the effects of the separation distance on the characteristics of the boundary layer are similar to that of the jet blowing from the downstream slot. The results shown again that effect of the designed actuator actuation mainly depends on the plasma induced jet.

a) **Mean velocity profiles**　　　　b) **Turbulence intensity profiles**
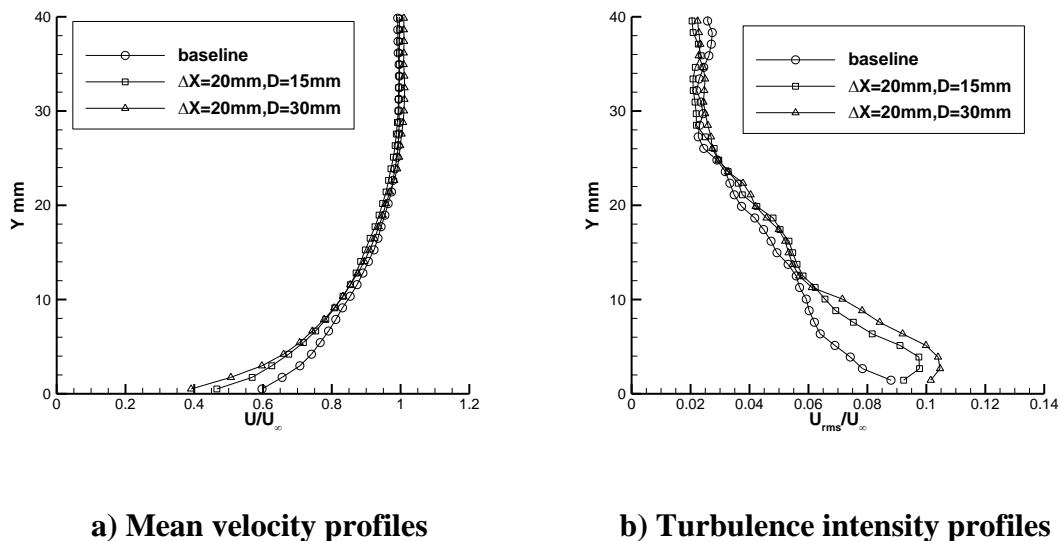
Figure 3.34: Effects of distance between the two slots of the actuator.

3.4 Summary

A detailed description of the wind tunnel and its modification for this study has been provided including an explanation for the major measurement techniques used. The design of the flat plate model and the driving circuit for the plasma actuators has also been discussed. The setup of measurement equipment and their calibration for the investigation are also presented. An outline of the flow conditions and boundary layer conditions is also provided.

The modified small wind tunnel keeps a turbulent level at about 0.2% and can be used for flow control investigation. The measurement flat plate surface pressure distribution and velocity profiles in the vertical plane indicted that the ZPG TBL flow has been fully developed.

It was found that the plasma jet actuator produced a transverse jet similar to a continuously blowing jet but with no mass addition into the flow field. The device is different from a traditional alternative blowing-and-suction synthetic jet as the current jet is continuously blown. As such, the DBD based jet actuator is different from either a mass injection blowing jet actuator or a traditional diaphragm based synthetic jet actuator.

Both the plasma actuations from the upstream and downstream slot effect along the streamwise direction is similar to that of a traditional blowing jet; in the vicinity of the plasma jet blowing slot, the flow is accelerated and the boundary layer displacement thickness, the momentum thickness and the shape factor are reduced. Farther downstream of the actuation slot, the actuation results in an increment of the boundary layer shape parameter and the changes gradually decreases with the increasing distance from the blowing slot. The effect of the plasma jet actuation on the mean velocity becomes weaker with increasing freestream flow speed. The effect of plasma actuation from the upstream slot blowing is smaller compare to the downstream slot blowing. Actuator with different air supply slot locations for both actuations have similar effect on the boundary layer and hence the fresh air supply slot design can fit the required operating condition flexibly. This is helpful for its flow control applications.

Chapter 4

Circular Cylinder Flow Control Using Plasma Based Jet Actuators

In this chapter, the circular cylinder flow control using the new designed five-electrode SD and AC+DC plasma based jet actuators are presented. Consideration is given to the application of the designed plasma jet actuators to a circular cylinder wake flow. The test Reynolds number based on the cylinder diameter are from 7,000 to 24,000 (the freestream velocity varies from 3m/s to 10m/s). An extensive flow control study was conducted using PIV measurement.

4.1 Experimental Setup

This section describes the cylinder model and wind tunnel facilities used for the experiments. The plasma based jet actuators used in this study are also presented.

4.1.1 Wind Tunnel Facility

The cylinder flow control experiments were performed in the same wind tunnel as described in section 3.1.1 at the University of Southampton. The cylinder model was mounted vertically in the test section 500mm downstream from the test section inlet. Both sidewalls and ceiling of the test section have optical access for non-intrusive laser flow field diagnostics (see Figure 4.1).

The cylinder model takes the form of a Perspex cylinder with an outer diameter D = 35 mm, wall thickness d = 3 mm, which serves as the dielectric. Hence the cylinder model produced a blockage ratio of 10%; the essential characters of the cylinder flow are therefore not altered by the test section blockage effect. Furthermore, in this study it is

the relative characters of the actuated versus non-actuated flows that are of most interest and this will not be significantly influenced by the degree of blockage.

Figure 4.1: Cylinder model in the wind tunnel.

4.1.2 PIV Setup

To determine the flow field in the wake of the cylinder, PIV was used to detect the characteristics of the flow. The PIV system used in this study is the same as described in section3.14. To capture images of the flow in the X-Z plane, the CCD camera was mounted above the wind tunnel pointing towards the floor of the test section. The laser was located outside of the wind tunnel test section exit. To capture images in the X-Z plane the laser sheet was aligned horizontally in parallel to the floor of the wind tunnel test section (Figure 4.2).
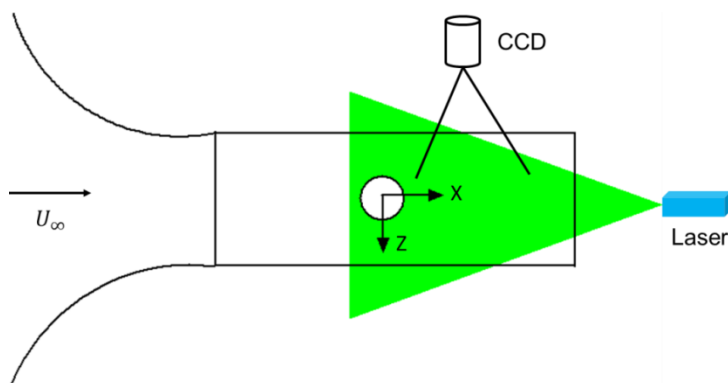
Figure 4.2: Arrangement of PIV measurement (top view).

4.1.3 Error and Uncertainty

The circular cylinder wake flow field with and without plasma actuations were measured by the same TSI 2D PIV system described in section3.1.4. For a typical experiment, the parameters for the PIV measurement were as below; the scale factor S_f=10.9, the time between laser pulses Δt=60μs, The CCD resolution γ=6.7μm is determined by the hardware and is fixed and the correlation peak p_c =0.1. The uncertainty in the velocity for an instantaneous vector $\varepsilon_U = \varepsilon_W$ is then estimated to be 0.11m/s based on the Eq. (3.1). And the corresponding uncertainty in the position of the vector $\varepsilon_X = \varepsilon_Z$ based on the Eq. (3.2) is 0.077 mm both in the streamwise and spanwise directions.

4.1.4 Plasma Based Jet Actuators Design

All the plasma based jet actuators used in this study are based on combined discharges with high AC and DC power supplies. The AC power supply system used in this study is the same system as described in section 3.13. For the combined discharges, the high DC voltage power supply is added to the object electrodes. The high DC voltage is produced from a Fug HCP140-35000 high DC power supply with output of 0 to -35 kV and 0 to 4mA, or a Fug HCP140-20000 high DC power supply with an output of 0 to 20 kV, and 0 to 6mA (Figure 4.3).

Figure 4.3: A high DC voltage power supply

The plasma jet actuators used in this study are all based on a new five-electrode design by combining two SD or AC+DC plasma actuators. The configuration of AC+DC discharge, as we know, when one exposed electrode is connected to a high AC voltage and a high positive DC component applied to another exposed electrode, the induced electric wind will increase respect to the case of DC = 0. But the induced visible plasma sheet is almost the same as a single DBD actuator (Figure 4.4). As mention in the literature review, when one exposed electrode is connected to a high AC voltage and a high negative DC component applied to another exposed electrode, the induced plasma sheet occupies the whole electrode gap.
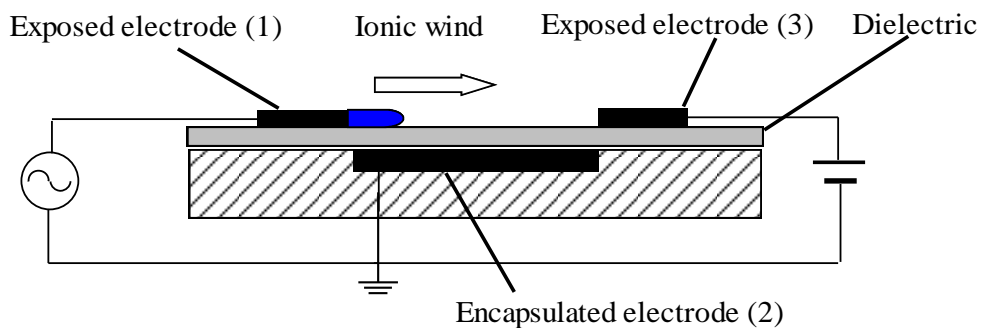
a) Actuator configuration.
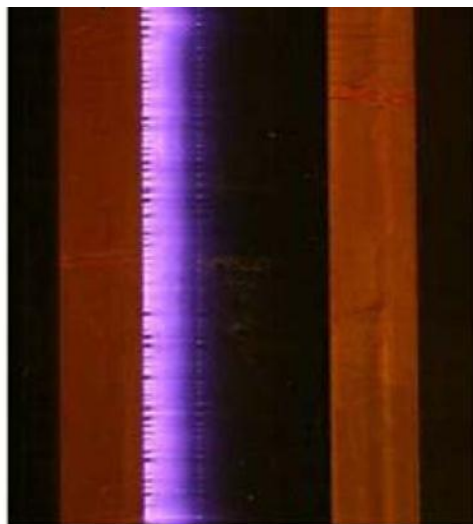
b) Photo of the AC+DC discharge (DC>0).

Figure 4.4: An AC+DC plasma actuator.

For a SD actuator actuation, the high AC voltage was applied to the encapsulated electrode, a negative (or positive) high DC was applied to one of the exposed electrode and the other exposed electrode was grounded. The induced plasma sheet covers the whole gap between the two exposed electrodes (Figure 4.5).
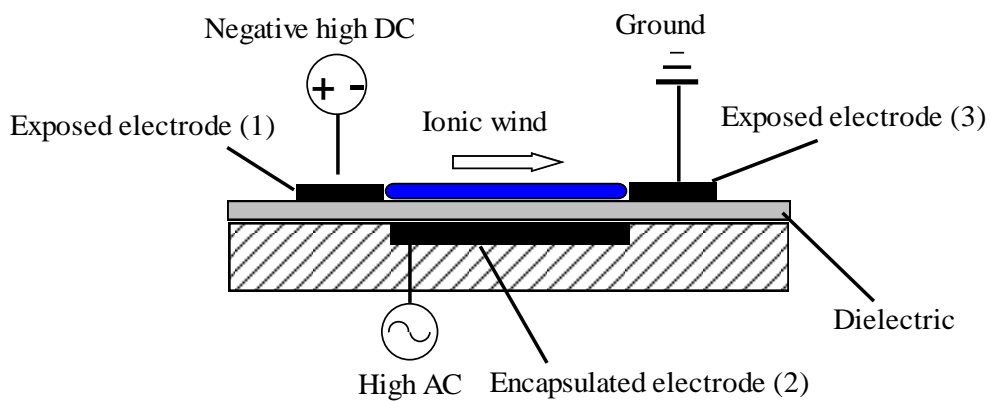
a) Actuator configuration.
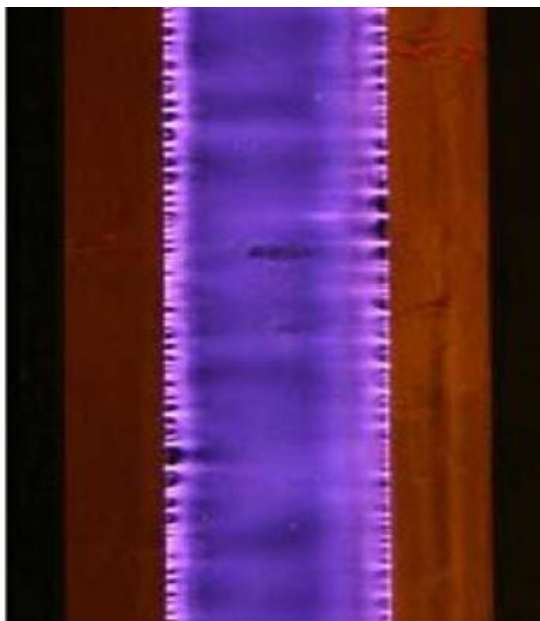
b) Photo of the SD discharge.

Figure 4.5: A SD plasma actuator.

4.1.4.1 Induced Flow in Quiescent Air by a SD Actuator

A typical single SD actuator induced flow field was investigated on a flat plate firstly, A scheme of the experimental setup is shown in Figure 4.6. In order to analyze the induced electric wind in the quiescent air, the plasma actuator was placed as a part of floor on the flat plate as described in section 3.1.2. Both exposed electrodes were made of copper foils and flush mounted on the surface of a Perspex flat plate (150 mm x 300 mm, thickness of 3 mm) and a third one disposed at the opposite side and was buried in order to inhibit discharges on this dielectric plate side. The exposed electrodes dimensions were 35 μm in thickness, 100 mm in length and 10 mm in width. The insulated electrode was 20 mm wide. The flat plate was put into the test section of the low speed wind tunnel in order to avoid external flow perturbations. One pressure probe was mounted on the dielectric surface. This probe was made of electrically insulating glass tube (internal diameter: 0.35 mm, outer diameter 0.67 mm, see Figure 4.6) and was connected by mean of a plastic tube to a low differential pressure transducer (0 to 249 Pa, accuracy of 0.14% full scale). The reference pressure value was measured at the test section but far away from the electrodes.
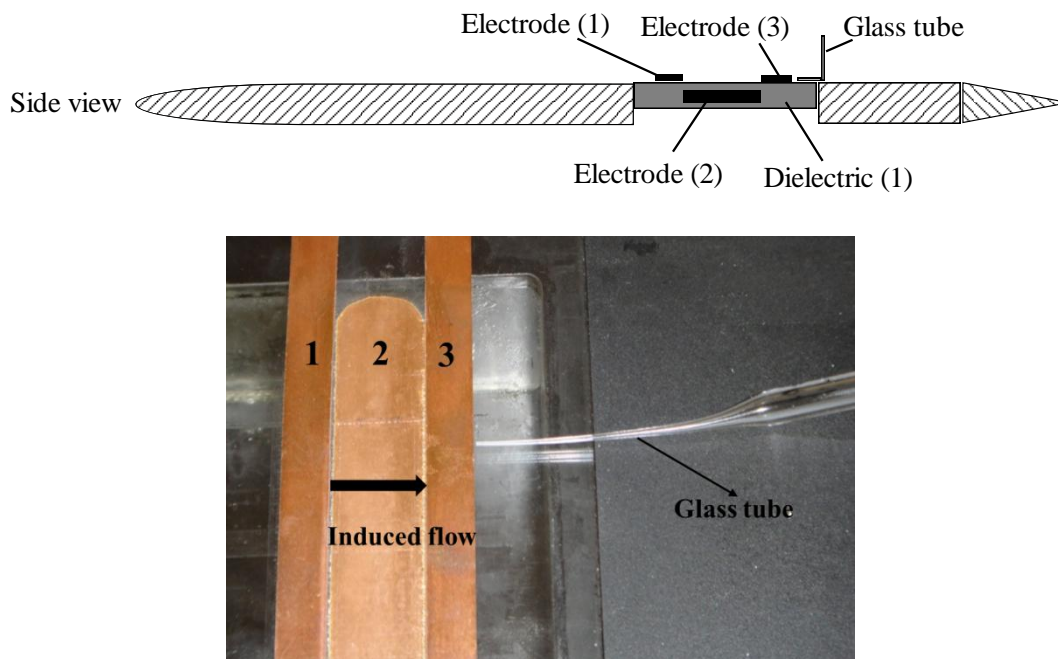
Figure 4.6: The measurement of a SD plasma actuator induced velocity.

Figure 4.7 shows the characteristics of the induced velocity in quiescent air generated by the SD actuator (as shown in Figure 4.5) under different operating conditions. The measurements were conducted on a flat plate and the induced velocity was measured using a glass Preston tube. The data were collected at a distance of 30 mm downstream of the edge of the electrode (1). The corresponding normal DBD induced velocity profiles were also measured at the same location. Compared to a normal DBD actuator, the SD actuator can induce a thicker wall jet and the maximum velocity increases with the applied DC high voltage. The induced maximum velocity will only reach the value achieved by a normal DBD when the applied DC voltage reaches a certain level (-12 kV in this case). At a fixed high DC voltage, a thicker wall jet and a higher induced maximum velocity can be obtained with a higher applied AC voltage. The application of these two types' actuators to a NACA0015 airfoil circulation control indicated that a higher lift augmentation can be achieved by a SD actuation compared to the corresponding AC actuation [106].
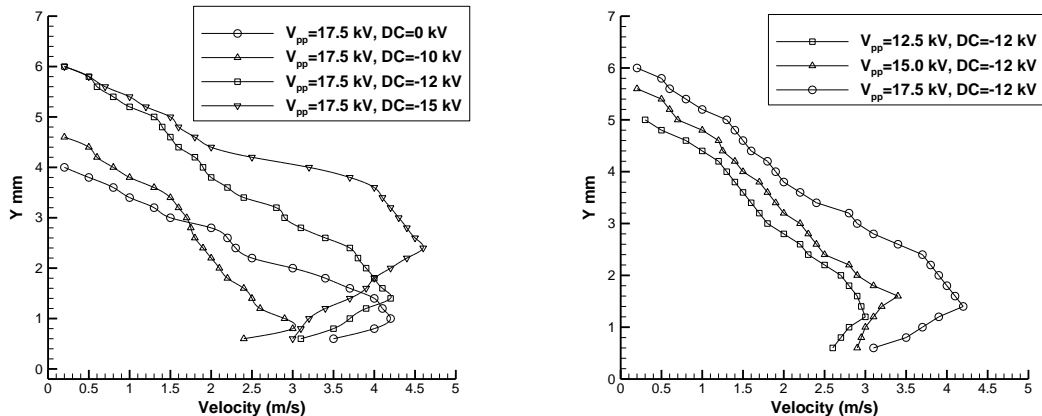
a) Comparison of different DC voltages.   b) Comparison of different AC voltages.

Figure 4.7: Induced velocity profiles by a single SD actuator in quiescent air.

4.1.4.2 Induced Flow in Quiescent Air by a SD Based Five-Electrode Actuator

A five-electrode configuration plasma jet actuator which combined with two SD plasma actuators is shown in Figure 4.8 and the corresponding discharge picture is shown in Figure 4.9.The time-averaged induced flow field by the plasma actuator is shown in

Figure 4.10. A vertical jet can be seen clearly. The actuator was operated with an *AC* voltage of 15 kV and the *DC*=-12 kV.
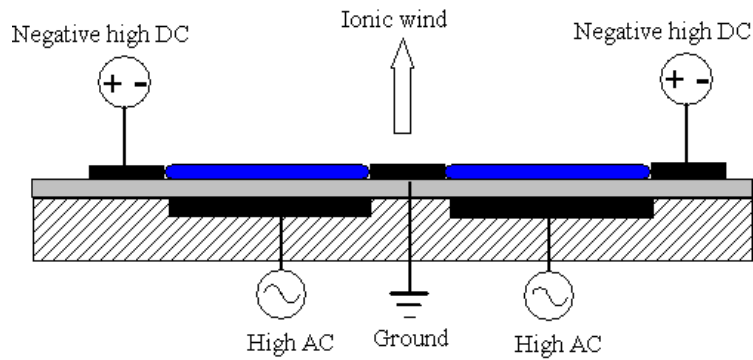
Figure 4.8: A five-electrode actuator configuration.
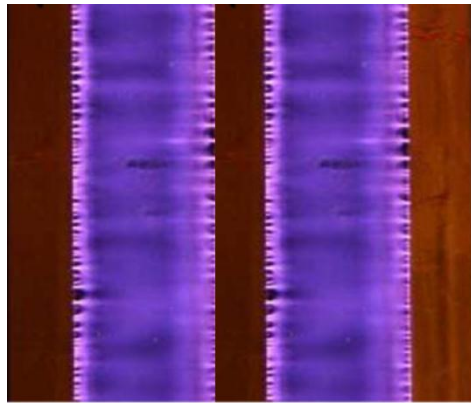
Figure 4.9: Discharge of a five-electrode actuator.
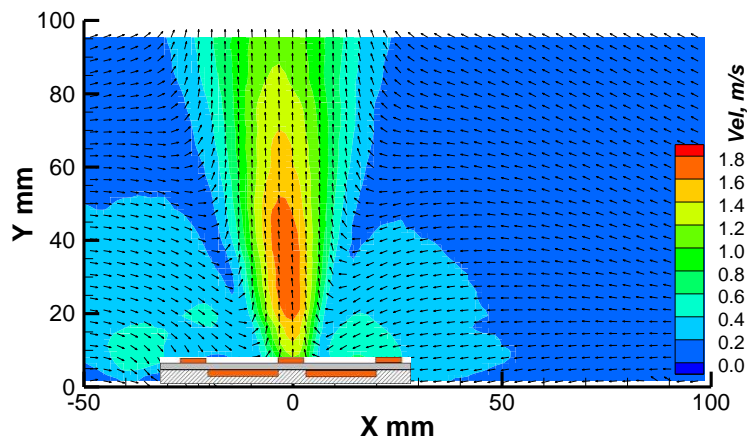
Figure 4.10: Induced velocity field in ambient air of a five-electrode actuator.

4.2 Application of Plasma Based Jet Actuators to a Circular Cylinder Model

Figure 4.11 presents the schematic of the new designed five-electrode plasma based jet actuator mounted on a circular cylinder model.
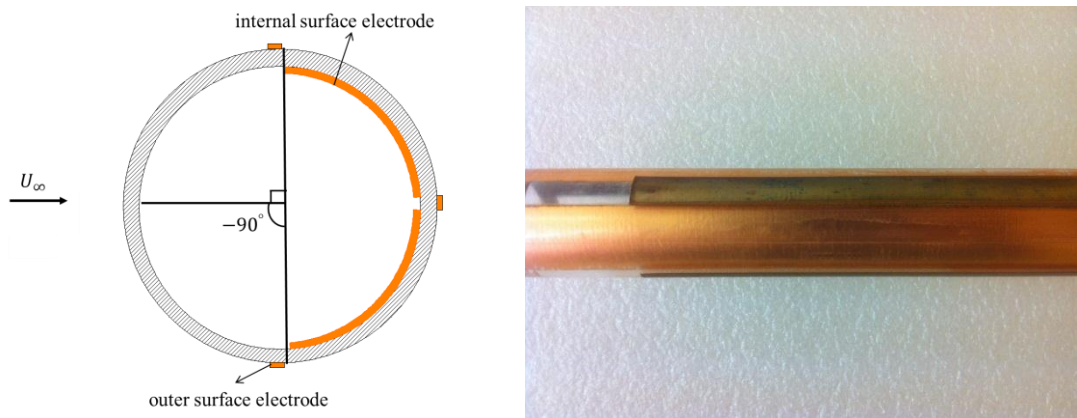
a) Electrodes arrangement.   **b) Photo of the cylinder with actuator.**

Figure 4.11: Schematic of a five-electrode actuator on a cylinder model.

In the configuration shown in Figure 4.11 the hollow cylinder wall serves as the dielectric barrier for the applied plasma actuators. As indicated in the sketch, two exposed electrodes are mounted to the surface of the cylinder with their plasma generating edges located at ±90° with respect to the approach flow direction and another exposed electrode was located at 180° position. These electrodes are made of 35 μm thick copper foil tape of width 5 mm. Note that the thickness of the electrodes is greatly exaggerated in Figure 4.11a. The corresponding two inner electrodes are mounted to the inner surface of the cylinder. They are each made of 35 μm thick copper foil tape of 20 mm width. Both inner and outer electrodes extend 230 mm in the spanwise direction. Plasma forms near the edge of the exposed electrode and extends a distance along the cylinder's dielectric surface. This approach of integration of the actuator with the model, in which the model wall serve as a dielectric barrier, common for all actuator configurations is very convenient and flexible compared to taping thin film actuators to the model surface or installing the plasma actuators into special slots in the model.

Induced flow in quiescent air. Before characterizing the behavior of the plasma based jet actuations on the flow around a circular cylinder in the wind tunnel, the flow induced solely by a typical SD based five-electrode actuator (Figure 4.12a) was examined in absent of external flow. Figure 4.12b presents the actuator induced flow downstream the cylinder. Because the plasma sheet produced by the SD based five-electrode actuator covers the whole rear part of the cylinder and the interaction between bright plasma sheet and the laser sheet will distort the PIV measurement results close to the cylinder rear end, the flow details near the surface were also not available due to insufficient particle seeding and/or high levels of reflection near the plasma sheet covered model surface. All our PIV data collections in this study were collected at 50mm-150mm ($X/D \approx 1.4$-4.0) downstream from the cylinder center line.
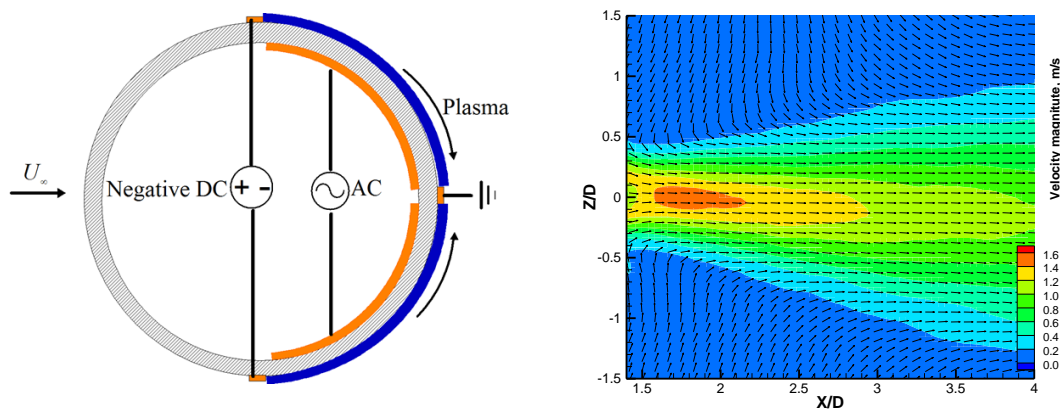
a) Actuator configuration (not to scale)   b) Velocity field

Figure 4.12: Induced velocity field in ambient air of a downward actuation.

The objective of this work is to determine the capability of the new designed five-electrode SD and AC+DC based jet actuators on circular cylinder wake flow control. The application of new designed five-electrode actuator on the circular cylinder can easily induce a downward or upward actuation around the rear part of the cylinder by simply changing the electrodes' connection. For example, by the driving circuit as shown in Figure 4.12, a downward actuation established. An upward actuation can be realized using the electrical circuit as shown in Figure 4.13. Both of these two types of actuations were studied in this thesis.
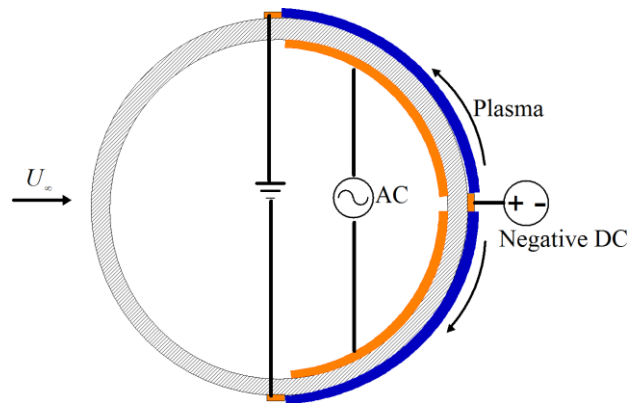
Figure 4.13: A SD based upward five-electrode actuator configuration.

The test conditions including different combinations and plasma driving parameters for both downward and upward actuations were summarized in Table 4.1.

Table 4.1: Experimental matrix

Downward actuations	Upward actuations
SD (U_∞=3, 5, 10 m/s)	AC+DC (U_∞=3, 5, 10 m/s)
SD with different AC (U_∞=5 m/s)	SD (U_∞=5 m/s)
SD with different DC (U_∞=5 m/s)	−
SD with different DC polarity (U_∞=5 m/s)	−
AC+DC (U_∞=5 m/s)	−

The Reynolds number for the current series of experiments (based on the freestream velocity and the diameter of the cylinder) are from $Re_D = 7{,}000$ to $24{,}000$ (the magnitude of free-stream velocity from 3m/s to 10m/s). These Reynolds numbers are in the subcritical flow regime with laminar flow separation. In this regime, the free shear layers form transition vorticies shortly after separation and before rolling into a turbulent Karman vortex street [107]. Near wake measurement results by using PIV are presented. All of these measurements were performed both with and without plasma actuation. The modifications of the circular cylinder wake at different Reynolds

numbers by different designed five-electrode plasma actuators were analyzed.

All the results of the cylinder wake characteristics are obtained from an ensemble average of 500 image pairs. Velocity measurements at the cylinder wake area highlighted the effect of the plasma actuation on the cylinder wake flow. The measured turbulence intensity is calculated based on the magnitude of the standard deviation of velocity and the freestream velocity:

$$U_{rms} = \{\frac{1}{N-1}\Sigma_1^N(U - U_{mean})^2\}^{0.5} \tag{4.1}$$

$$W_{rms} = \{\frac{1}{N-1}\Sigma_1^N(W - W_{mean})^2\}^{0.5} \tag{4.2}$$

$$TI = \sqrt{U_{rms}^2 + W_{rms}^2}/U_\infty \tag{4.3}$$

In the near wake of the circular cylinder, drag determinations based solely on the streamwise velocity deficit are insufficient [108], the contribution of Reynolds normal stresses to the total momentum deficit was found to be non-trivial, so the determination of sectional drag coefficients necessarily included contributions of the Reynolds normal stresses to the total momentum deficit, as given by

$$c_d = \frac{2}{DU_\infty^2}\int_{-\infty}^{+\infty} U(U_\infty - U)dz + \frac{2}{DU_\infty^2}\int_{-\infty}^{+\infty}(W_{rms}^2 - U_{rms}^2)dz$$

$$= \frac{2}{D}\sum_1^N \frac{U}{U_\infty}(1 - \frac{U}{U_\infty})\Delta Z + \frac{2}{D}\sum_1^N(\frac{W_{rms}^2}{U_\infty^2} - \frac{U_{rms}^2}{U_\infty^2})\Delta Z \tag{4.4}$$

This expression was evaluated numerically for each transverse measurement location in the wake region.

4.3 Experimental Results for Downward Plasma Actuations

In this section, a series of experimental investigations were conducted with the designed downward five-electrode plasma based jet actuators as described in Table 4.1.

4.3.1 Results of a SD based Downward Actuation

Firstly, the effect of a SD based five-electrode actuation is checked in detail. The plasma actuator configuration is shown as in Figure 4.12a. The actuation was operated at V_{pp} =17.5 kV, DC=-10 kV.

Figures 4.14-4.16 show the velocity field in the cylinder wake with and without plasma actuation at different freestream velocities. The flow is from left to right. The velocity fields were obtained from an ensemble average of 500 image pairs. In contrast to the plasma-off case, the plasma actuation reduced the width of the separated wake region and the velocity magnitude was increased in the wake. The effects of the actuation decreased with the increasing of freestream flow speed. For example, at U_∞= 3 m/s, X/D=4, the velocity defect region is reduced from ±1.5D to ±1.0D, but for U_∞= 10 m/s, X/D=4, the velocity defect region just reduced from ±1.5D to ±1.4D.

a) Plasma-off case   b) Plasma-on case
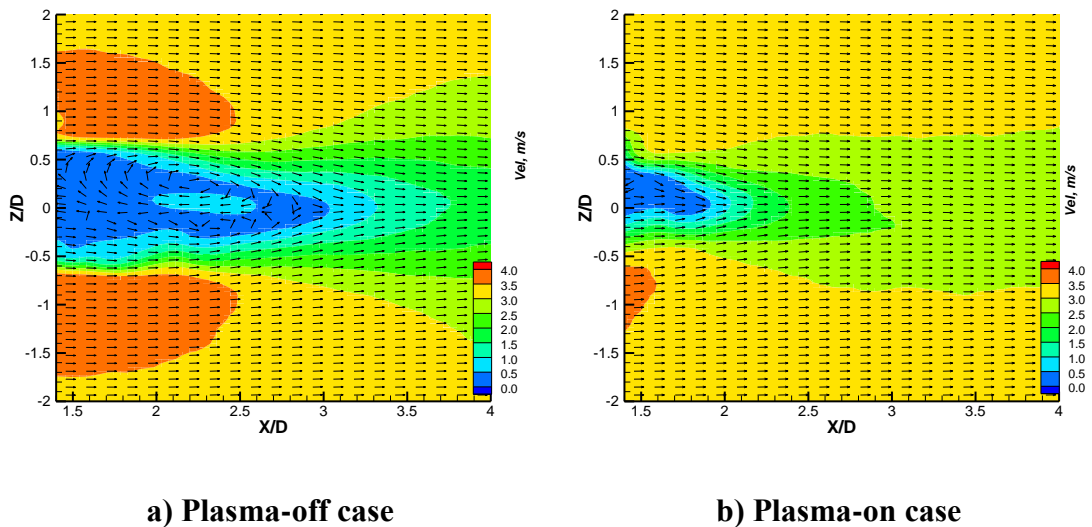
Figure 4.14: Velocity field at U_∞= 3 m/s (SD, V_{pp}=17.5 kV, DC=-10 kV).

a) Plasma-off case   b) Plasma-on case
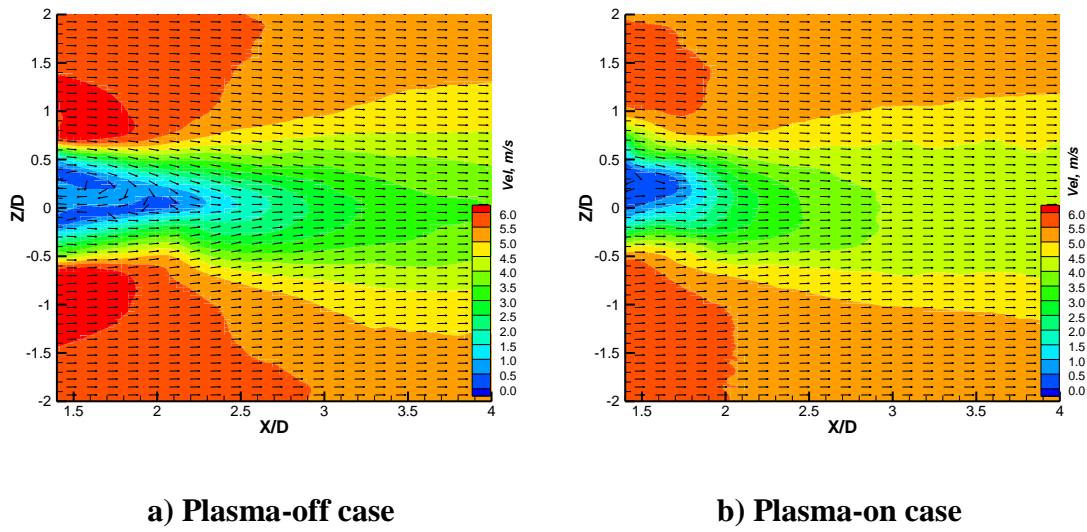
Figure 4.15: Velocity field at U_∞= 5 m/s (SD, V_{pp}=17.5 kV, DC=-10 kV).

a) Plasma-off case   b) Plasma-on case
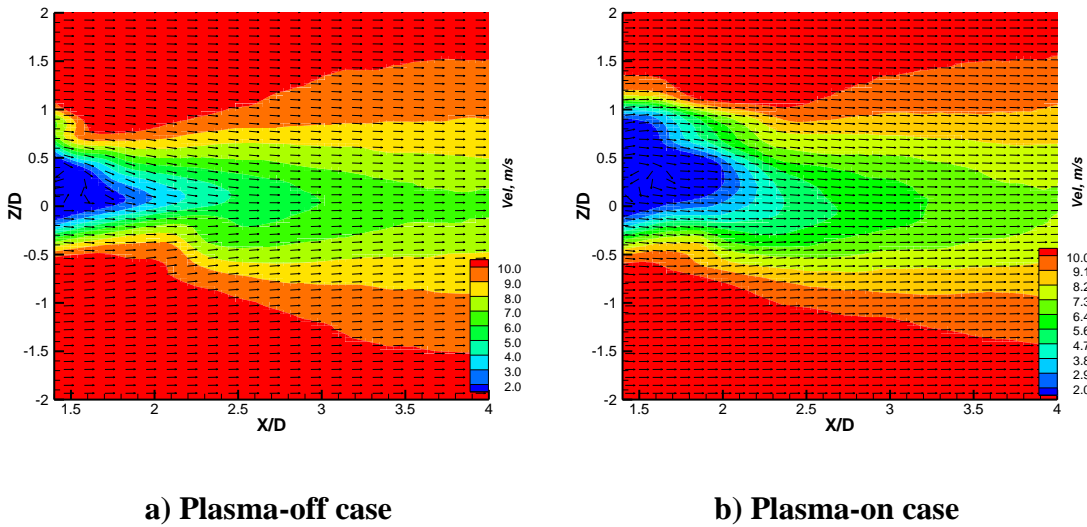
Figure 4.16: Velocity field at U_∞= 10 m/s (SD, V_{pp}=17.5 kV, DC=-10 kV).

The turbulence intensity contours showed in Figures 4.17-4.19 identify the effect of the plasma actuation on the cylinder wake. The results indicate that the plasma actuation stables the flow separation, both the highest level and higher magnitude area of the turbulence intensity in the wake decrease under the plasma actuation. For example, at U_∞= 5 m/s, the maximum turbulent intensity reduces from 0.7 to 0.5 and the whole area of the turbulence intensity magnitude bigger than 0.5 is reduced to 0.4. The

effectiveness of plasma actuation on the cylinder wake flow field and its turbulence intensity decreases with the increasing of oncoming freestream velocity.

a) Plasma-off case   b) Plasma-on case
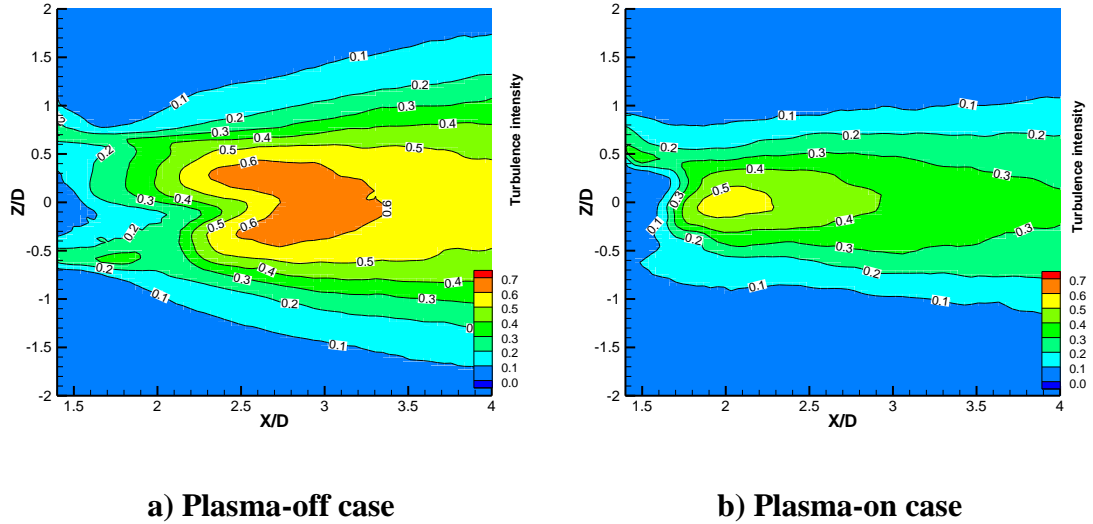
Figure 4.17: Turbulence intensity at U_∞=3 m/s (SD, V_{pp}=17.5 kV, DC=-10 kV).

a) Plasma-off case   b) Plasma-on case
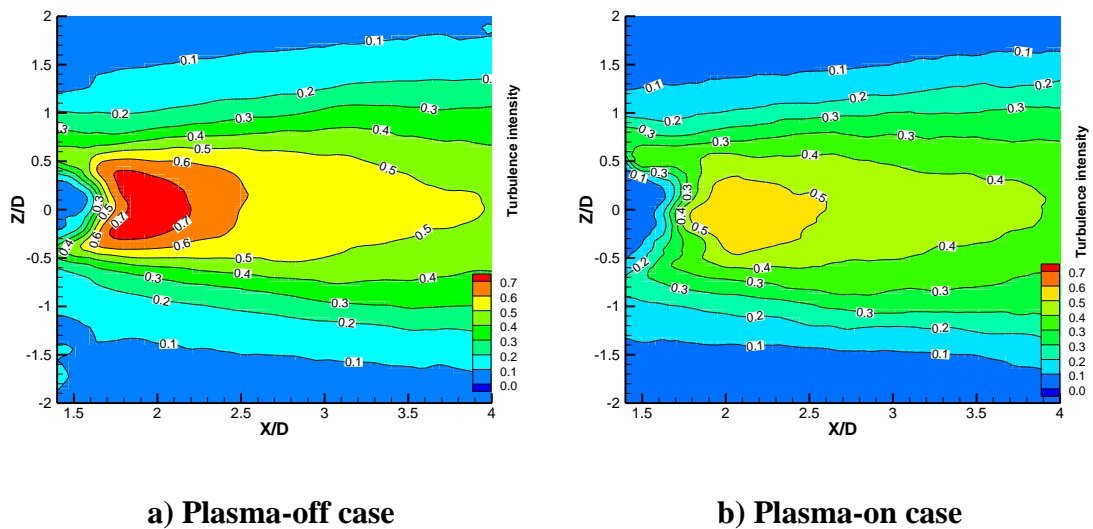
Figure 4.18: Turbulence intensity at U_∞=5 m/s (SD, V_{pp}=17.5 kV, DC=-10 kV).

a) Plasma-off case   **b) Plasma-on case**
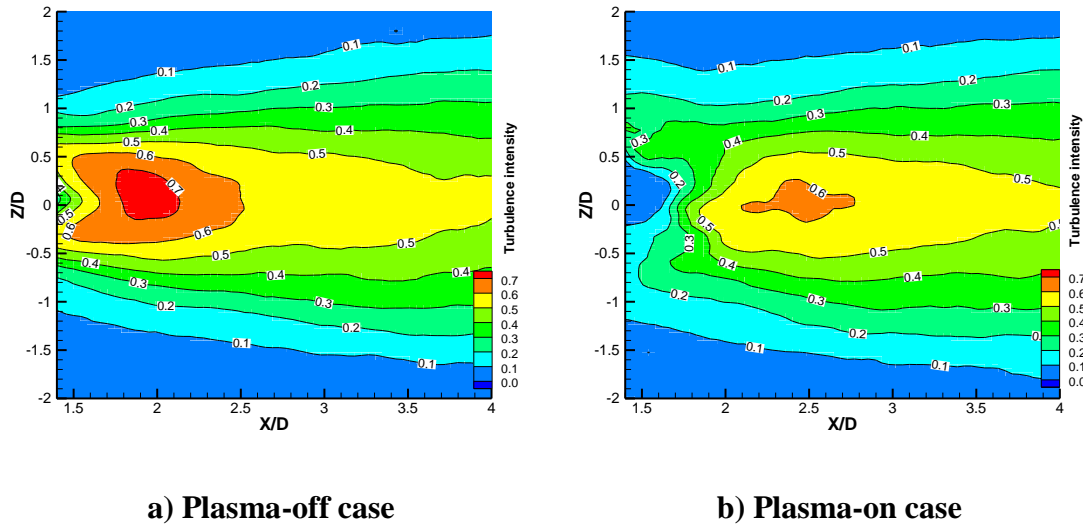
Figure 4.19: Turbulence intensity at U_∞=10 m/s (SD, V_{pp}=17.5 kV, DC=-10 kV).

Mean velocity and turbulence intensity profiles were also obtained at selected X/D locations in order to characterize the cylinder wake under natural and SD plasma actuated conditions. Figures 4.20-4.22 presented the mean streamwise velocity profiles at U_∞ = 5 m/s over a representative range of X/D=2, 3, 4, respectively. The results showed that the velocity deficit in the wake region of SD actuation was substantially less than the baseline case. The data at X/D=3 and 4 also compare well with the data of Ong and Wallace [109], who presented wake velocity data for a circular cylinder at a Reynolds number of 3900. At X/D=2, the maximum velocity defect $\Delta U_{max}/U_\infty$ reduces from 0.88 to 0.42, the wake half width $b_{1/2}$ increases from 0.75D to 1.05D. At X/D=3, the maximum velocity defect $\Delta U_{max}/U_\infty$ reduces from 0.42 to 0.22, the wake half width $b_{1/2}$ increases from 1.35D to 1.70D. At further downstream, when X/D=4, the maximum defect is approximately 45% of the baseline. The reduction of the maximum velocity defect is due to the plasma actuation induces extra downstream velocity into the wake as described in Figure 4.12b.

Figure 4.20: Wake streamwise mean velocity profiles (*X/D*=2, U_∞=5 m/s).

Figure 4.21: Wake streamwise mean velocity profiles (*X/D*=3, U_∞=5 m/s).

Figure 4.22: Wake streamwise mean velocity profiles (*X/D*=4, U_∞=5 m/s).
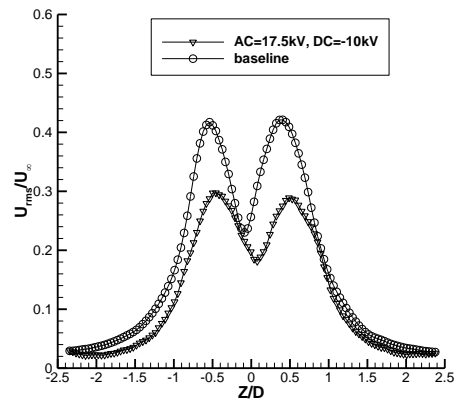
Figure 4.23: Wake streamwise turbulence intensity profiles (*X/D*=2, *U*$_\infty$=5 m/s).
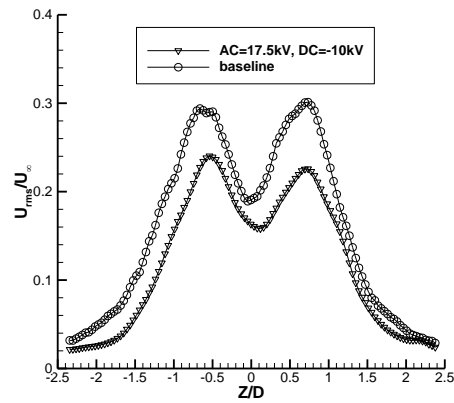
Figure 4.24: Wake streamwise turbulence intensity profiles (*X/D*=3, *U*$_\infty$=5 m/s).
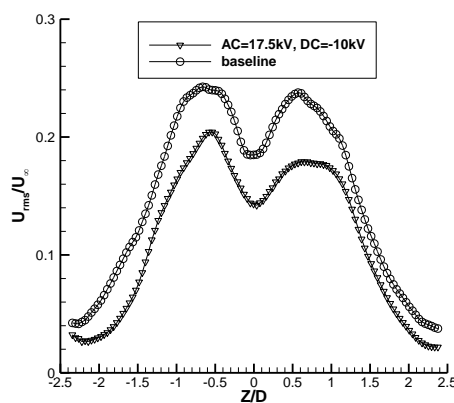
Figure 4.25: Wake streamwise turbulence intensity profiles (*X/D*=4, *U*$_\infty$=5 m/s).

Wake profiles of the streamwise turbulence intensity at different downstream locations are shown in Figures 4.23-4.25. The distribution of velocity fluctuations exhibits the typical two-lobed pattern [110]. The results are not perfect symmetric mainly due to the laser reflection from the copper electrode on the cylinder model. At X/D=3, the highest velocity fluctuation occurring at $Z/D \approx \pm0.75$ for the baseline case, with the plasma actuation, this position changes to $Z/D \approx \pm0.7$ and the peak turbulence intensity under the plasma actuation is reduced from 0.29 to 0.23. At X/D =4, the peak turbulence intensity under the plasma actuation is reduced from 0.24 to 0.19 and the highest velocity fluctuation position changes from $Z/D \approx \pm0.65$ to ±0.60 under the plasma actuation. These results indicate that the time-averaged wake width and the wake unsteadiness are reduced under the influence of the plasma actuation.

The mean transverse velocity profiles were shown in Figures 4.26-4.28. The velocity distributions in both cases also match the velocity profiles at X/D=3 and 4 measured by Ong and Wallace [109]. The results show that the transverse velocity is suppressed by the plasma actuation. At X/D=2, the peak velocity is reduced from ±0.24 to ±0.1; at X/D=3, the peak velocity is reduced from ±0.06 to ±0.04; and for X/D=4, the transverse velocity becomes nearly zero under the plasma actuation.
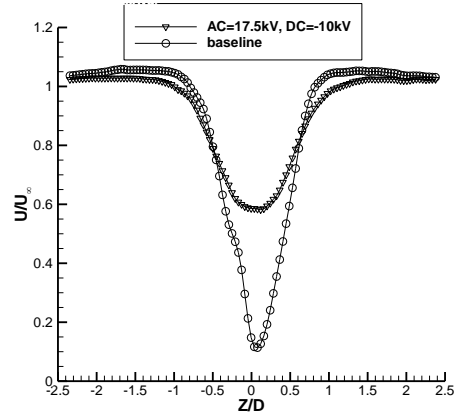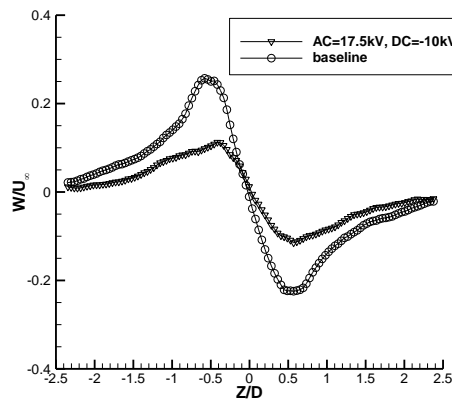

Figure 4.26: Wake transverse mean velocity profiles (X/D=2, U_∞=5 m/s).
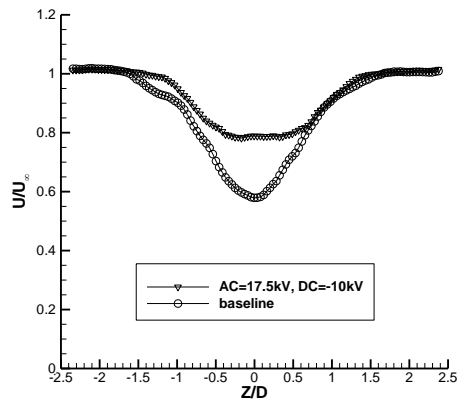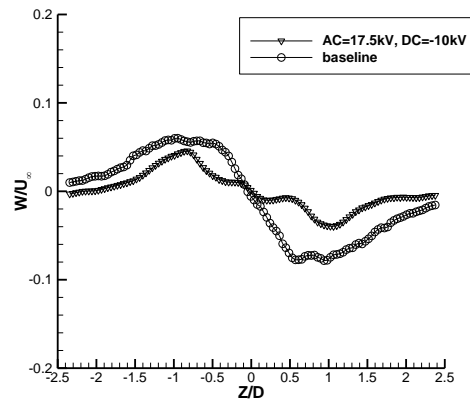
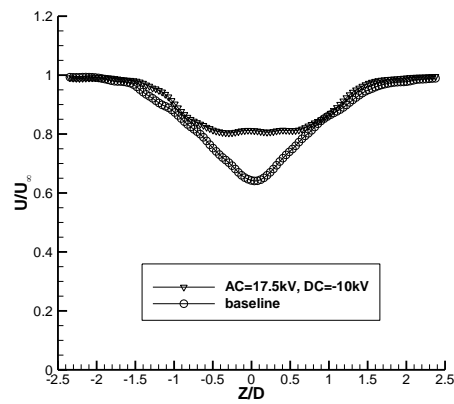**Figure 4.27: Wake transverse mean velocity profiles (*X/D*=3, U_∞=5 m/s).**
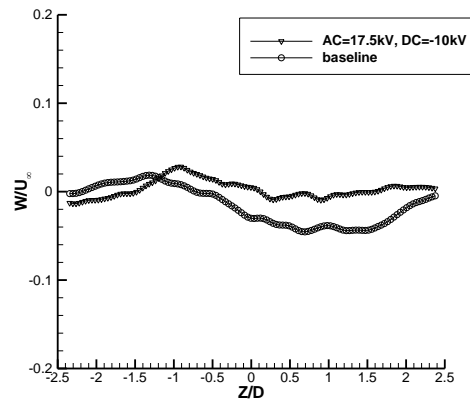
**Figure 4.28: Wake transverse mean velocity profiles (*X/D*=4, U_∞=5 m/s).**

The transverse turbulence intensities for both with and without plasma actuation are shown in Figures 4.29-4.31. Note that the turbulence intensity values in the baseline wake are quite high compare to the streamwise component. This is associated with the unsteady transverse motion of the wake due to Karman vortex shedding. At *X/D*=2, the maximum turbulence intensity value still reduced from 0.65 to 0.55. The plasma actuation results in a 25% reduction in transverse turbulence intensity at *X/D*=3. At *X/D*=4, the maximum turbulence intensity value is reduced from 0.48 to 0.38, an approximately 21% reduction. These results suggest that the plasma actuation suppressed the unsteady transverse wake motion associated with near-wake Karman vortex shedding.

78
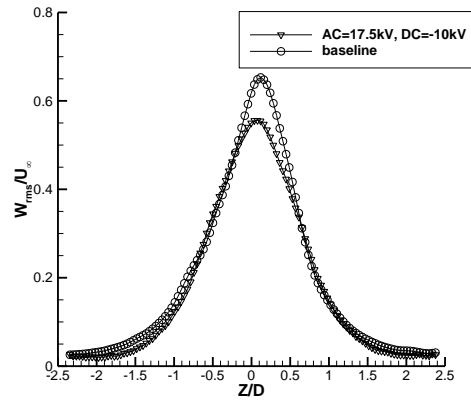
Figure 4.29: Wake transverse turbulence intensity profiles (*X/D*=2, *U*$_\infty$=5 m/s).
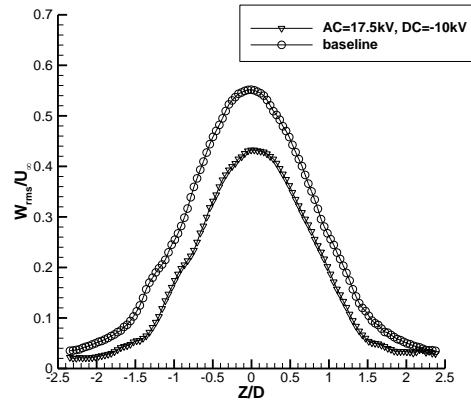
Figure 4.30: Wake transverse turbulence intensity profiles (*X/D*=3, *U*$_\infty$=5 m/s).
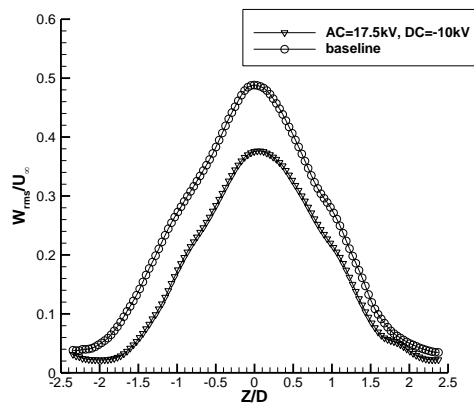
Figure 4.31: Wake transverse turbulence intensity profiles (*X/D*=4, *U*$_\infty$=5 m/s).

Sectional drag coefficients are also evaluated through the wake profiles with Eq. (4.4). As discussed previously, the Reynolds normal stresses are incorporated into the evaluation since the measurement planes are close to the downstream edge of the circular cylinder. The sectional drag coefficients for the baseline at $X/D=3$ and 4 are 1.18 and 1.19. Both of these values are slightly higher than a traditional value of 1.1 at a subcritical Reynolds number. Under the plasma actuation, the drag coefficients at $X/D=3$ and 4 are 0.82 and 0.86, respectively, results in the drag reductions of 30.5% and 27.7%. The drag coefficient for $U_\infty=5$ m/s ($Re_D=12,000$) at different section is shown in Figure 4.32. The results indicated that overall drag reduction is 30% and is bigger than the results reported by Sosa et al [29], which an up to 25% drag reduction measured directly by a balance was obtained using two separated AC+DC actuators at Reynolds number 10,560.
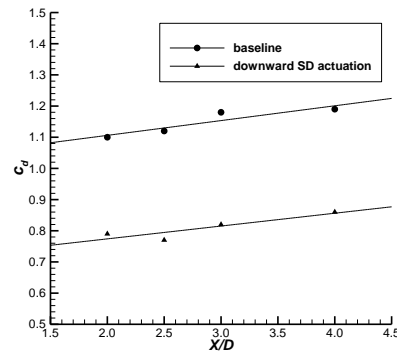
Figure 4.32: Comparison of cylinder drag coefficients (SD, $U_\infty=5$ m/s).

The effects of the same SD based five-electrode plasma jet actuation ($V_{pp}=17.5$ kV, $DC=-10$ kV) at different Reynolds numbers are shown in Figures 4.33-4.35 for $X/D=2.5$. Three Reynolds numbers of $Re_D = 7,000$, 12,000 and 24,000 (with freestream velocity $U_\infty=3$ m/s, 5 m/s and 10 m/s) were tested under the same plasma actuation. At $U_\infty=3$ m/s, the maximum velocity defect $\Delta U_{max}/U_\infty$ reduces from 0.7 to 0.26, the wake half width $b_{1/2}$ increases from 1.1D to 1.2D. At $U_\infty=5$ m/s the maximum velocity defection $\Delta U_{max}/U_\infty$ reduces from 0.6 to 0.3, the wake half width $b_{1/2}$ increases from 1.03D to 1.35D. At $U_\infty=10$ m/s, the maximum defect is just changes from 0.48 to 0.41 and there is no change of the wake half width. With the increase of Reynolds number, the plasma effect is reduced. This is due to the relative momentum addition by the plasma actuation is reduced with the increasing of the freestream velocity.
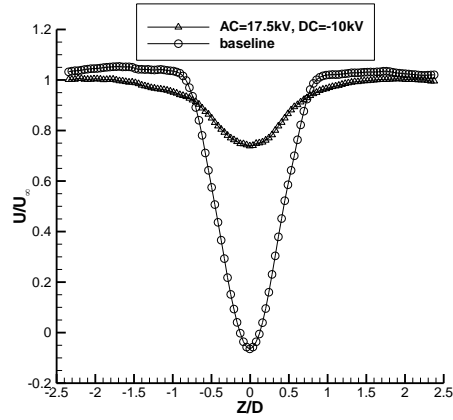
Figure 4.33: Wake streamwise velocity profiles at Re_D =7,000 (*X/D*=2.5).
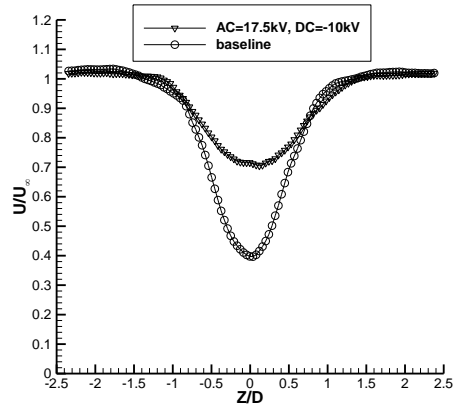
Figure 4.34: Wake streamwise velocity profiles at Re_D =12,000 (*X/D*=2.5).
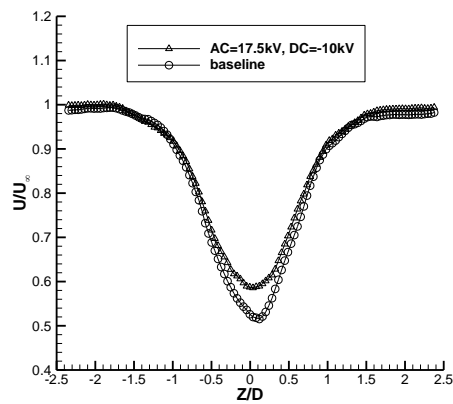
Figure 4.35: Wake streamwise velocity profiles at Re_D =24,000 (*X/D*=2.5).

81

The sectional drag coefficients under the plasma actuation at *X/D*=2.5 for U_∞=3 , 5, and 10 m/s are 0.59, 0.77 and 1.17, respectively, results in the corresponding drag reductions of 52%, 31% and 2.5%.

Wake streamwise turbulence intensity at different Reynolds numbers for *X/D*=2.5 are shown in Figures 4.36-4.38. At U_∞=3 m/s, the highest velocity fluctuation occurring at *Z/D* ≈ ±0.4 for the baseline case, with the plasma actuation, this position changes to *Z/D* ≈ ±0.3 and the peak turbulence intensity under the plasma actuation is reduced from 0.39 to 0.2. At U_∞=5 m/s, the peak turbulence intensity under the plasma actuation is reduced from 0.35 to 0.27 and the highest velocity fluctuation position changes from ±0.5D to ±0.6D under the plasma actuation. For U_∞=10 m/s, only the peak turbulence intensity is reduced from 0.32 to 0.28 and just slight change on the velocity fluctuation location.
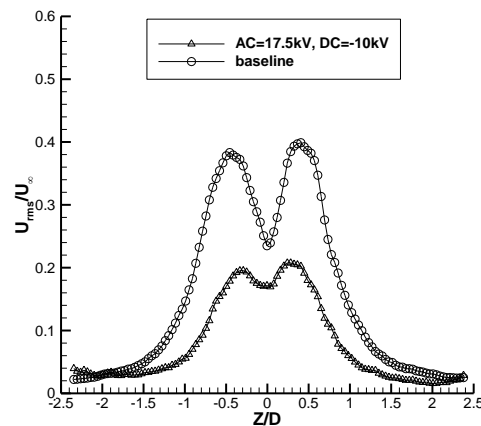
Figure 4.36: Wake streamwise turbulence intensity at Re_D =7,000 (*X/D*=2.5).
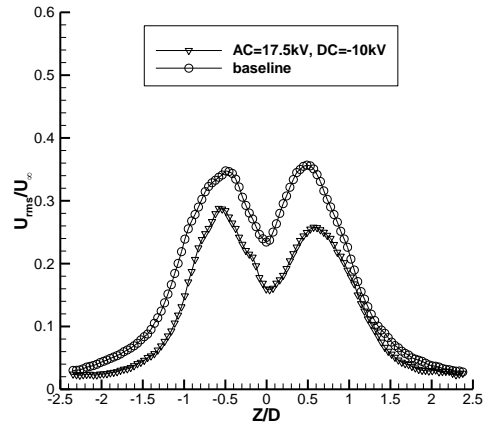
Figure 4.37: Wake streamwise turbulence intensity at Re_D =12,000 (X/D=2.5).
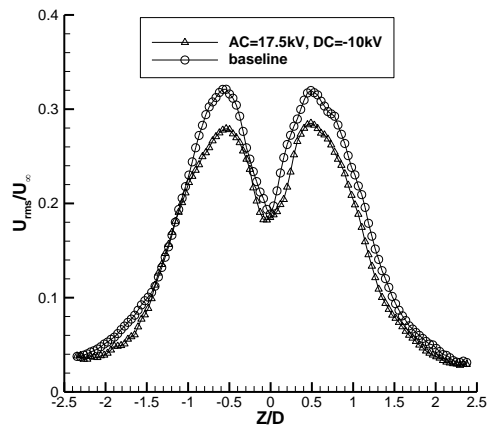
Figure 4.38: Wake streamwise turbulence intensity at Re_D =24,000 (X/D=2.5).

4.3.2 Results of Plasma Parameter Studies

Different applied high AC voltages. The influence of the applied high AC voltage for the SD based five-electrode actuator configuration was studied. The experiments were conducted U_∞=5 m/s, the applied voltages were 12.5, 15 and 17.5 kV and the DC voltage was fixed at -10 kV. The sectional wake profiles at X/D=2.5 are shown in Figures 4.39 and 4.40. Compare to the baseline case without plasma actuation, under the

tested condition, with increasing the applied AC voltage, the effects on the cylinder wake flow is similar. For example, the maximum velocity defects $\Delta U_{max}/U_\infty$ all decrease from about 0.30 to 0.23 and the peak turbulence intensities decrease from around 0.30 to 0.28. The results suggest that an expected results may be achievable using the SD actuation with corresponding lower AC voltage and hence with less energy consumption.

a) **Mean velocity**   b) **Turbulence intensity**
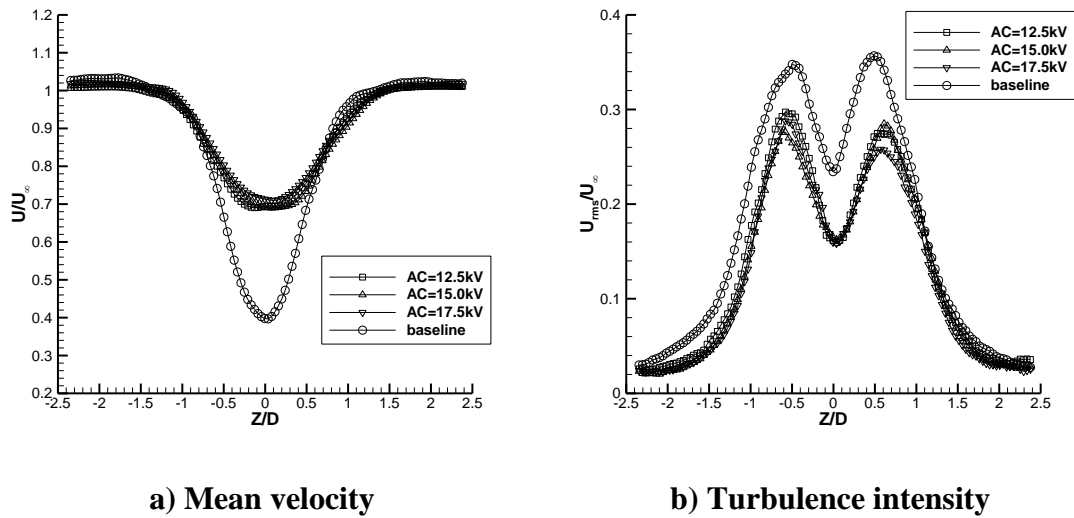
Figure 4.39: Comparison of streamwise velocity at different applied AC voltages.

a) **Mean velocity**   b) **Turbulence intensity**
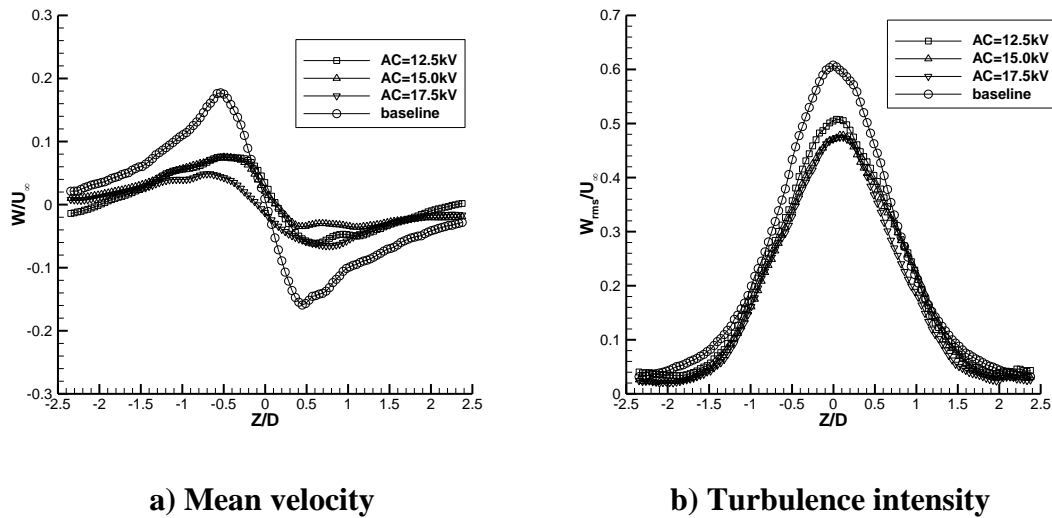
Figure 4.40: Comparison of transverse velocity at different applied AC voltages.

Different applied high DC voltages. Figures 4.41 and 4.42 showed the effects of different applied high DC voltages on the cylinder wake region. The high AC voltage was fixed at 15 kV and the high DC voltage varies from -8 kV to -12 kV. The data is collected at U_∞=5 m/s and X/D=2.5. Compare to the baseline case, with increasing the applied high DC voltage absolute value, the overall effects on the cylinder wake flow characteristics have slight differences. Both the maximum streamwise velocity defect changes and the peak streamwise turbulence intensity reduction at different applied high DC voltages are nearly the same. The maximum transverse velocity for the applied DC=-8, -10, and -12 kV, is reduced from ±0.16 to ±0.08, ±0.06 and ±0.05, respectively, and a slight higher transverse turbulence intensity peak reduction can be found with higher applied high DC voltage absolute value. The results indicate that a bigger wake velocity defect reduction can be obtained with higher applied DC voltage absolute values. This is in consistent with the actuation electric characteristics of the SD actuation mention in section 4.2.

a) Mean velocity   b) Turbulence intensity
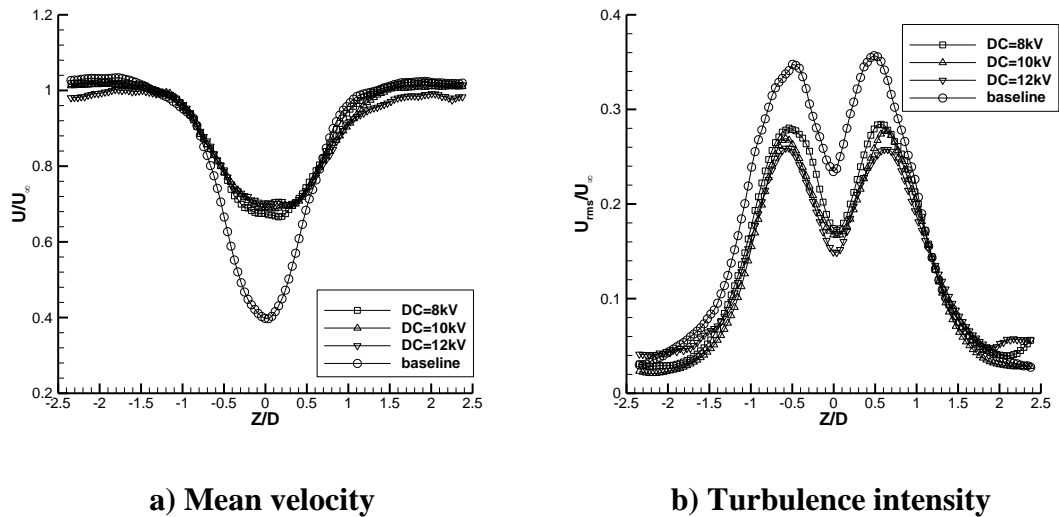
Figure 4.41: Comparison of streamwise velocity at different applied DC voltages.

a) **Mean velocity**   b) **Turbulence intensity**
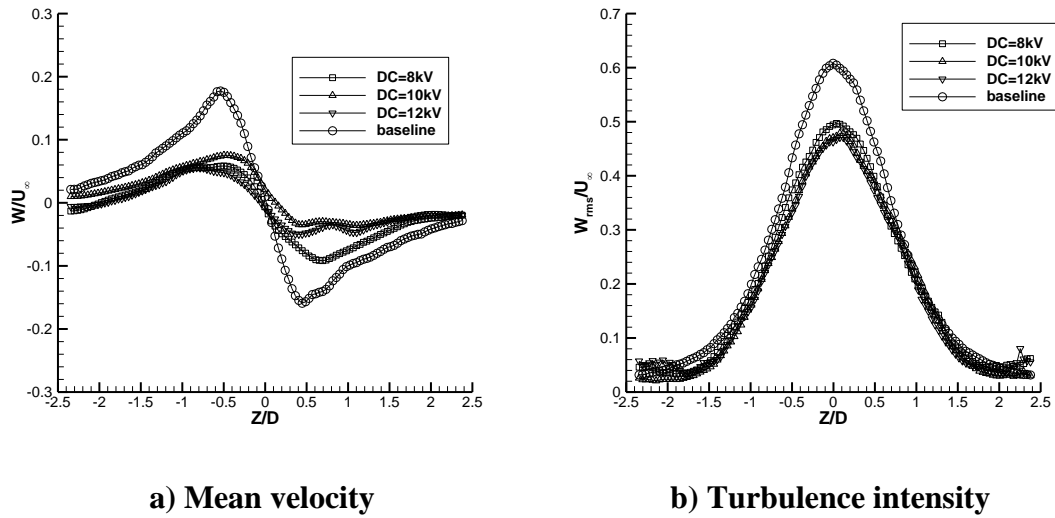
Figure 4.42: Comparison of transverse velocity at different applied DC.

Different applied high DC voltage polarity. A downstream actuation can also be achieved by the five-electrode design based on the SD actuation using a positive DC power supply (see Figure 4.43). The typical results are shown in Figures 4.44 and 4.45. The applied AC voltage is fixed at 17.5kV and the freestream velocity U_∞=5 m/s. At X/D=2.5, compares to the negative DC voltage case, with the same applied DC voltage absolute value, the same control effectiveness is obtained. The result suggests that for this SD based five-electrode plasma jet actuator design, the choice of high DC polarity is optional.
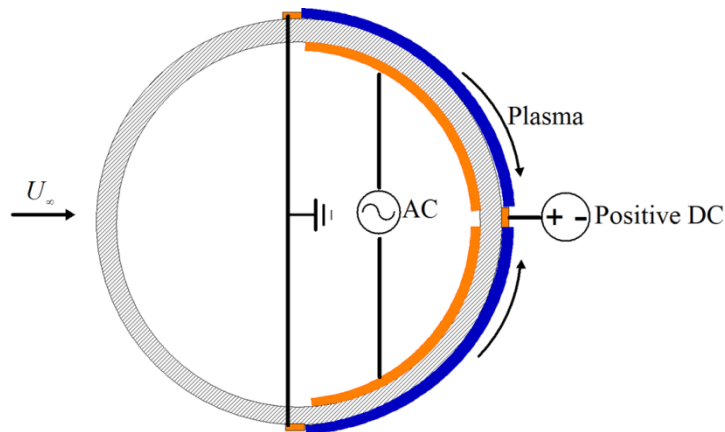
Figure 4.43: Schematic of a SD based downward actuator configuration (DC>0).

| a) Mean velocity | b) Turbulence intensity |
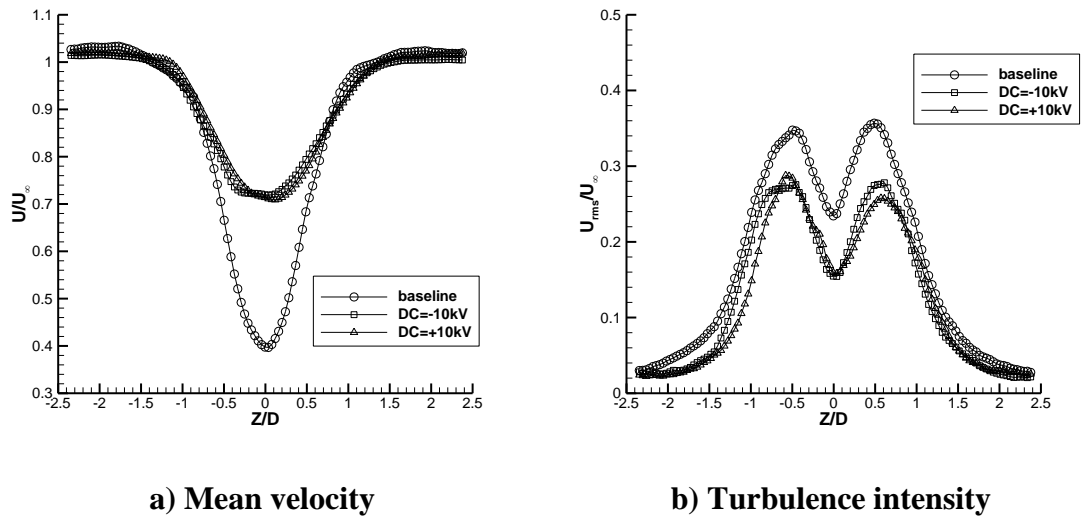
Figure 4.44: Comparison of streamwise velocity with different high DC polarity.

| a) Mean velocity | b) Turbulence intensity |
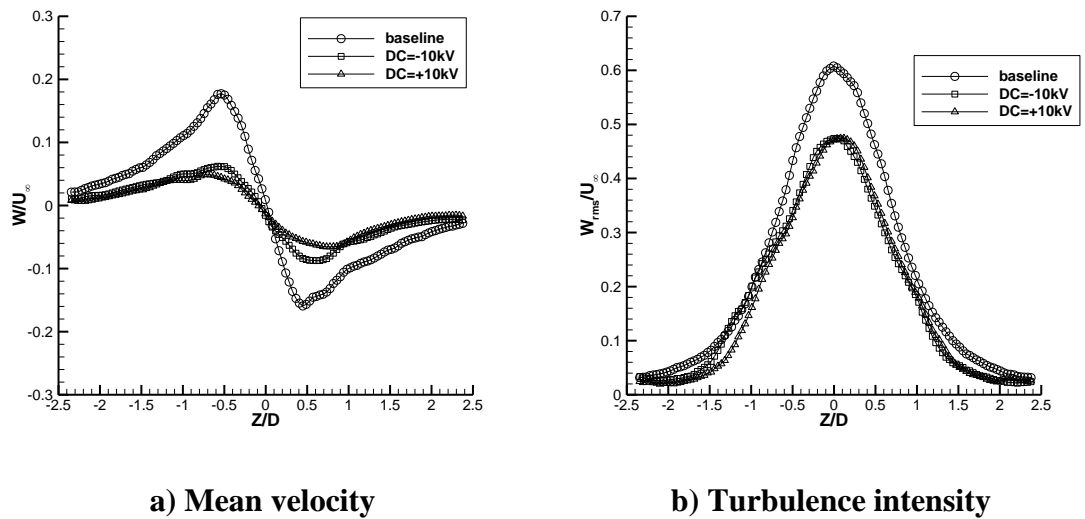
Figure 4.45: Comparison of transverse velocity with different high DC polarity.

4.3.3 Results of an AC+DC Based Downward Actuation

In this part, experiments were conducted to compare the effects between an AC+DC based five-electrode downward plasma actuator (see Figure 4.46) and the corresponding

SD based actuator (see Figure 4.43). Both actuators were operated with an *AC*=17.5 kV and *DC*=10 kV and the freestream velocity was 5 m/s.
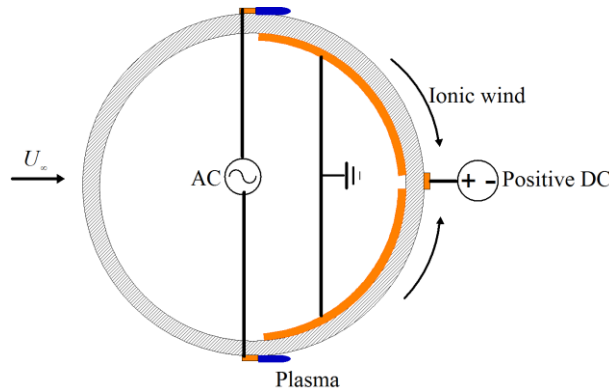
Figure 4.46: Schematic of an AC+DC based downward actuator configuration.

Typical results are shown in Figures 4.45 and 4.46. Compare to the baseline case, with the same applied AC and DC voltage values; the maximum streamwise velocity defect $\Delta U_{max}/U_\infty$ for SD and AC+DC based actuations are 0.29 and 0.33, respectively, and the peak streamwise turbulence intensity reduced from 0.35 to 0.24, and 0.27 under the actuations, respectively. As to the transverse components, the effects of both actuations are very similar. The results indicate that a SD based actuator is slightly more efficient than an AC+DC based actuator.

a) **Mean velocity**   b) **Turbulence intensity**
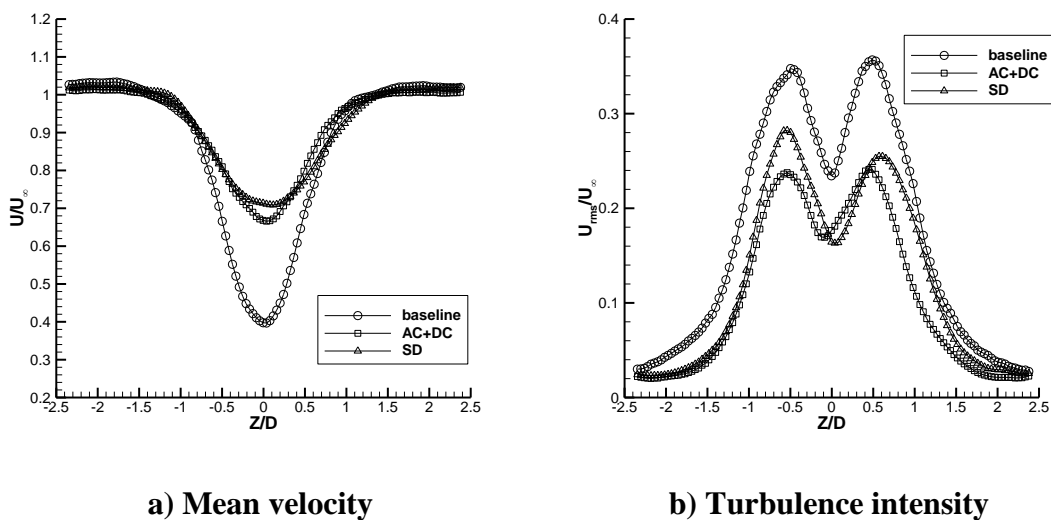
Figure 4.47: Comparison of SD and AC+DC based downward actuations (streamwise velocities).

| a) Mean velocity | b) Turbulence intensity |
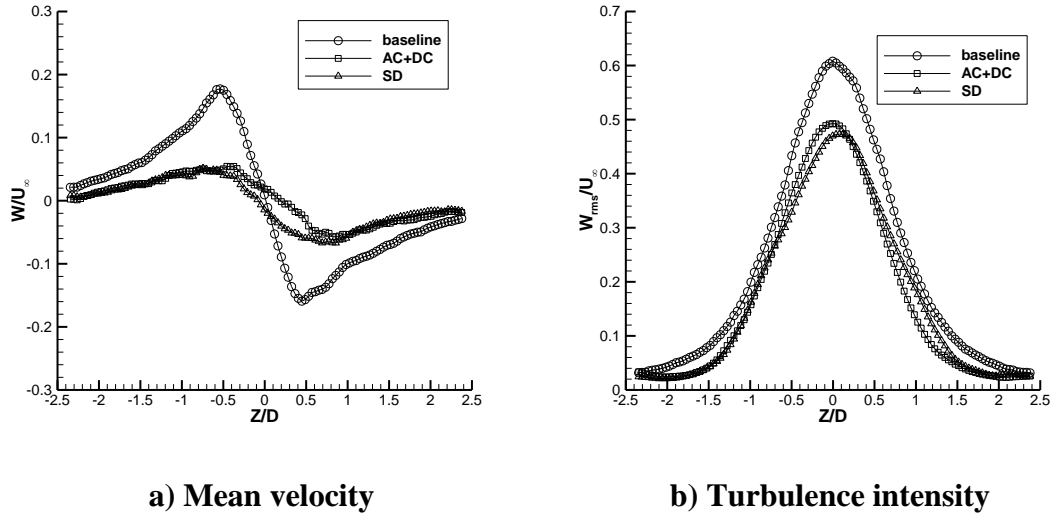
Figure 4.48: Comparison of SD and AC+DC based downward actuations (transverse velocities).

4.4 Experimental Results for Upward Plasma Actuations

This section presents the results of experimental investigations for the upward actuations by the five-electrode plasma actuators. The arrangement of the five electrodes on the cylinder model is the same as the corresponding downward actuator (Figure 4.13). These actuations can be achieved by changing the plasma power supplies electric circuit conveniently. All the results of the cylinder wake flow characteristics were obtained from an ensemble average of 500 image pairs.

4.4.1 Results of an Upward AC+DC Actuation

Based on the SD based actuation and AC+DC based actuation has demonstrated to have very similar effect on cylinder wake flow in section 4.3. In this section, the effect of the upward AC+DC actuation was selected to investigate in detail. The plasma actuator configuration applied in this study is shown in Figure 4.49. The actuation was operating at V_{pp}=17.5 kV, DC=-10 kV. The corresponding SD based upward actuation was also tested for comparison.
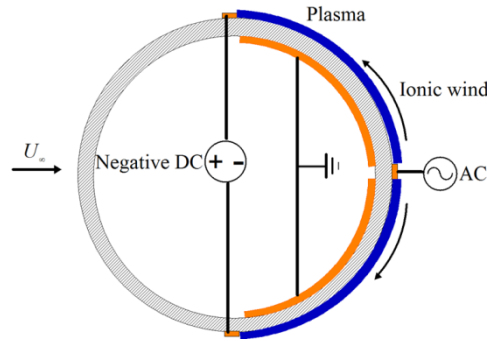
Figure 4.49: Schematic of an AC+DC based upward actuator configuration.

Figures 4.50-4.52 showed the velocity flow field in the cylinder wake with and without plasma actuation at different freestream velocities. In contrast to the plasma-off case, the plasma actuation increases the width of the separated wake region and the velocity magnitude is decreased in the wake. The effects of the actuation decreased with the increasing of freestream flow speed. For example, at U_∞= 3 m/s, the high speed velocity region (*Vel*>3.0 m/s, *X/D*=1.4-2.5) is almost disappeared under the actuation and the whole wake velocity magnitude is decreased. This is due to the addition of the reverse velocity produced by the plasma actuation.

a) **Plasma-off case**   b) **Plasma-on case**
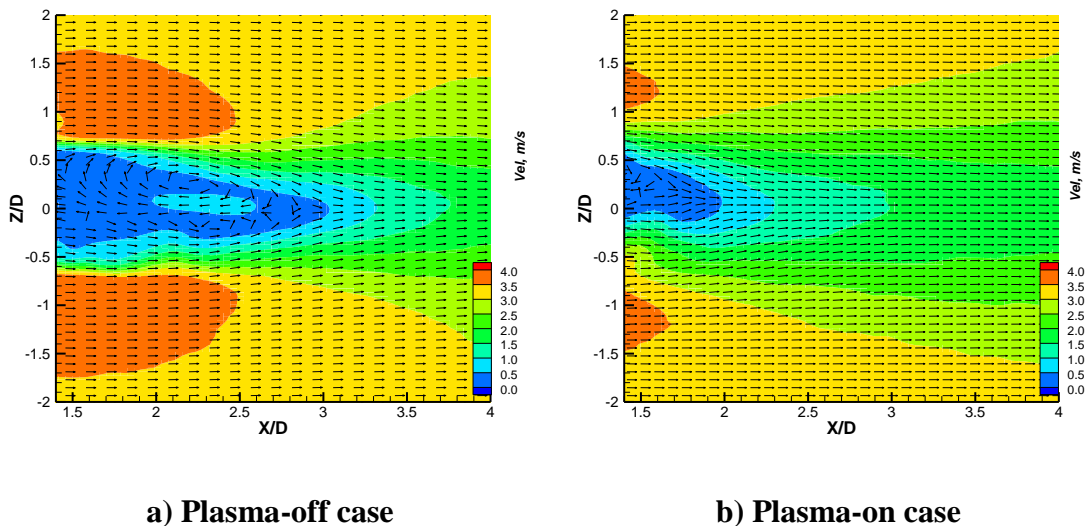
Figure 4.50: Velocity field at U_∞=3 m/s (AC+DC, V_{pp}=17.5 kV, *DC*=-10 kV).

a) Plasma-off case   b) Plasma-on case
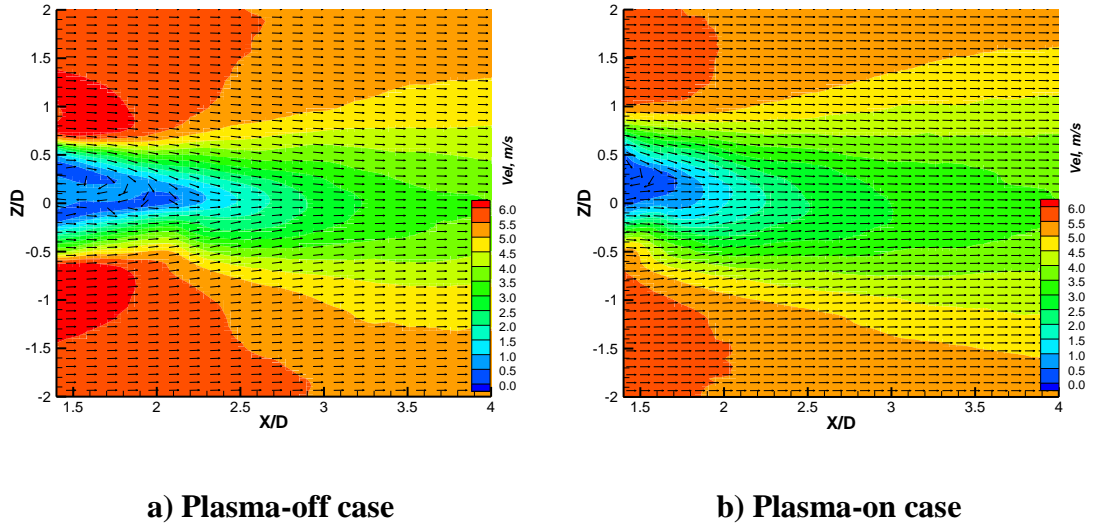
Figure 4.51: Velocity field at U_∞=5 m/s (AC+DC, V_{pp}=17.5 kV, DC=-10 kV).

a) Plasma-off case   b) Plasma-on case
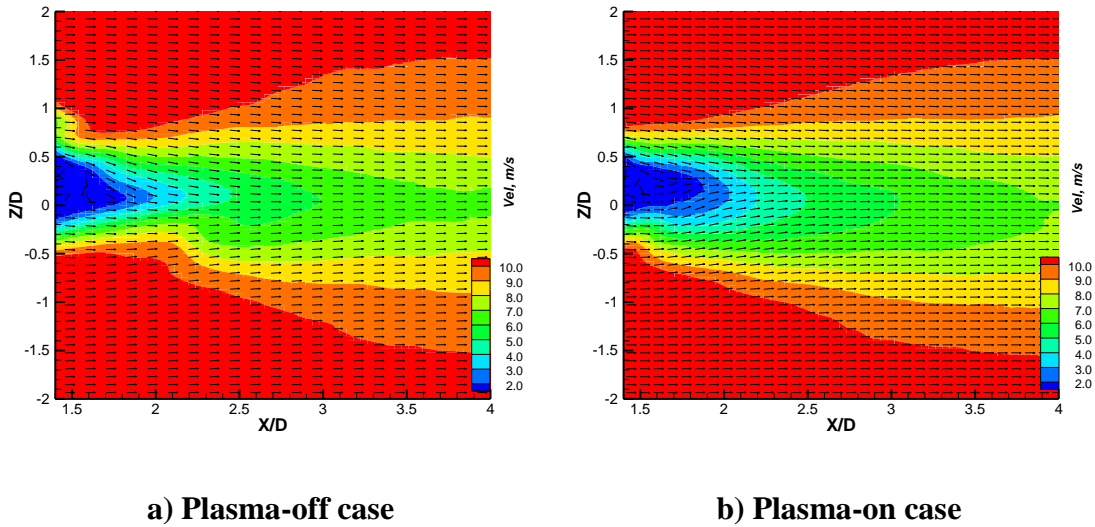
Figure 4.52: Velocity field at U_∞=10 m/s (AC+DC, V_{pp}=17.5 kV, DC=-10 kV).

The turbulence intensity contours are presented in Figures 4.53-4.55. The upward plasma jet actuation increases the cylinder wake turbulence intensity level. For example, at U_∞=3 m/s, the maximum turbulence intensity increases from 0.6 to 0.8 and the turbulence intensity in the whole wake region is greatly increased. It is interesting that the maximum turbulent intensity level reduced from 0.7 to 0.6 even though the overall turbulence level increased at U_∞=10 m/s. This may due to the momentum addition of

the plasma actuation enhanced the flow separation but suppressed the large scale Karman vortex shedding and hence the high level velocity fluctuations are reduced.

a) Plasma-off case   b) Plasma-on case
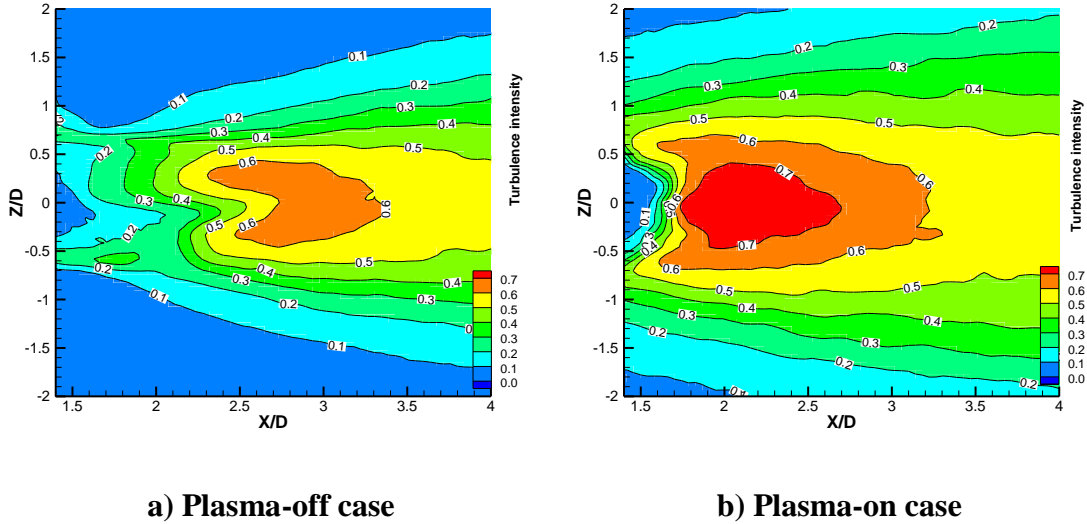
Figure 4.53: Turbulence intensity contours at U_∞=3 m/s (AC+DC, V_{pp}=17.5 kV, DC=-10 kV).

a) Plasma-off case   b) Plasma-on case
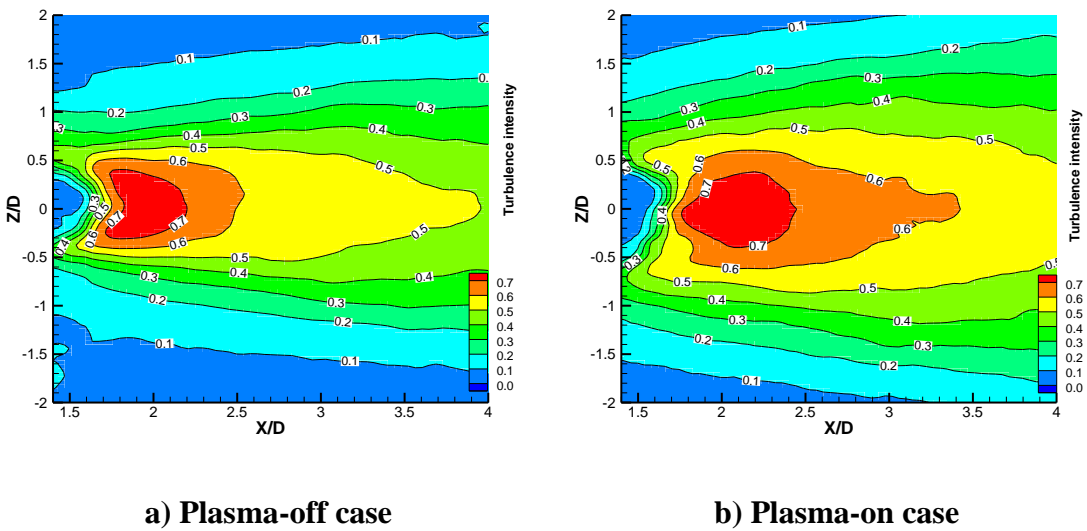
Figure 4.54: Turbulence intensity contours at U_∞=5 m/s (AC+DC, V_{pp}=17.5 kV, DC=-10 kV).

a) Plasma-off case   b) Plasma-on case
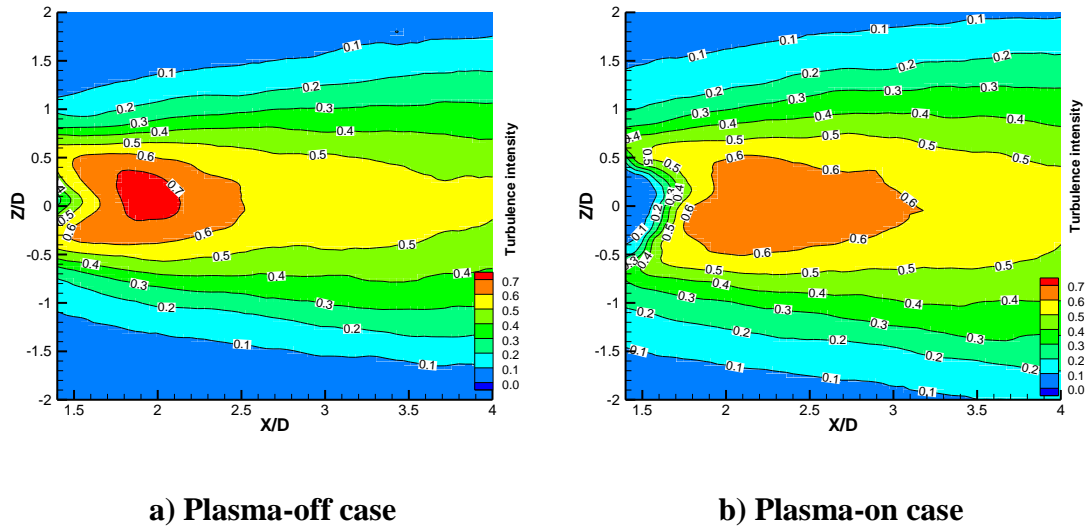
Figure 4.55: Turbulence intensity contours at U_∞=10 m/s (AC+DC, V_{pp}=17.5 kV, DC=-10 kV).

The mean velocity and turbulence intensity profiles were also obtained at typical X/D locations in order to characterize the cylinder wake under natural and plasma actuated conditions. Figures 4.56-4.58 present the streamwise velocity profiles of X/D=2, 3, 4, respectively. At X/D=2, maximum velocity defection $\Delta U_{max}/U_\infty$ reduces from 0.88 to 0.65, the wake half width $b_{1/2}$ increases from 0.75D to 1.2D. At X/D=3, the maximum velocity defection $\Delta U_{max}/U_\infty$ has little changes but the wake half width $b_{1/2}$ increases from 1.35D to 1.75D. At further downstream, when X/D=4, the wake half width $b_{1/2}$ increases from 1.55D to 2.2D.

Wake profiles of the streamwise turbulence intensities at different downstream locations are shown in Figures 4.59-4.61. The distribution of velocity fluctuations still exhibits the typical two-lobed pattern [110] after the plasma actuation. At X/D=3, the highest velocity fluctuation occurring at $Z/D \approx \pm0.75$ for the baseline case, with the plasma actuation, this position changes to $Z/D \approx \pm0.9$, but the peak turbulence intensity under the plasma actuation is no change. At X/D =4, the peak turbulence intensity under the plasma actuation is increased from 0.24 to 0.27 but the highest velocity fluctuation position remain at $Z/D \approx \pm0.6$ under the plasma actuation. These results indicate that the time-averaged wake width and the wake unsteadiness are increased due to the plasma actuation.
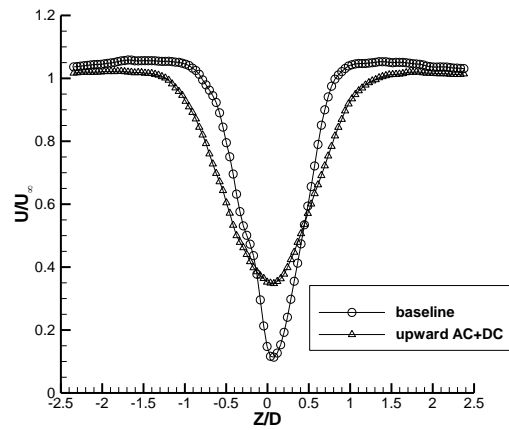
Figure 4.56: Wake streamwise velocity profile (AC+DC, *X/D*=2, *U*$_\infty$=5 m/s).
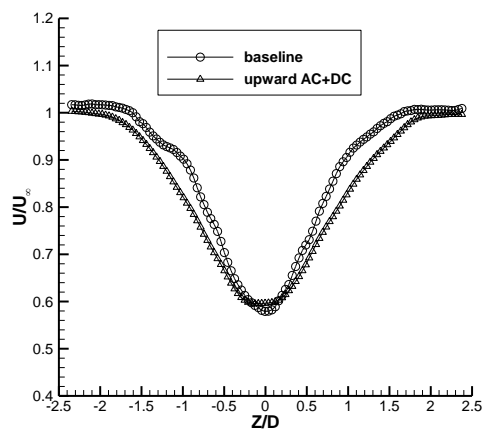
Figure 4.57: Wake streamwise velocity profile (AC+DC, *X/D*=3, *U*$_\infty$=5 m/s).
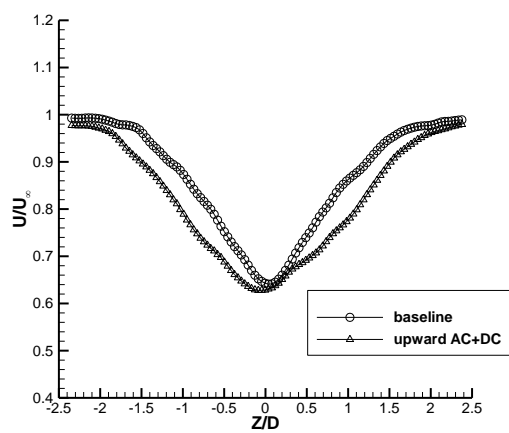
Figure 4.58: Wake streamwise velocity profile (AC+DC, *X/D*=4, *U*$_\infty$=5 m/s).
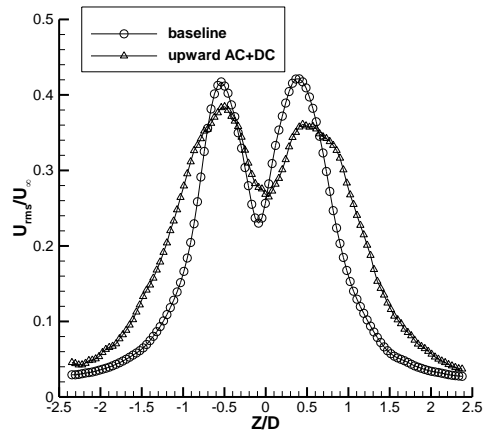
Figure 4.59: Wake streamwise turbulence intensity (AC+DC, *X/D*=2, *U*$_\infty$=5 m/s).
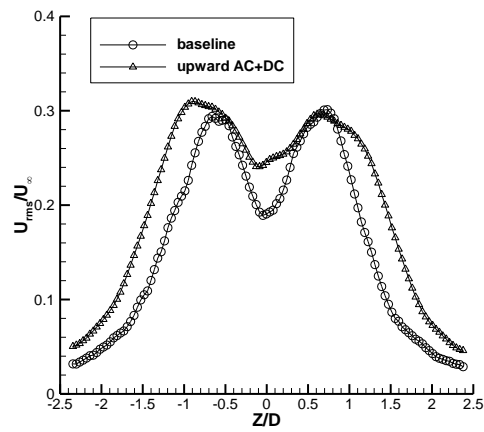
Figure 4.60: Wake streamwise turbulence intensity (AC+DC, *X/D*=3, *U*$_\infty$=5 m/s).
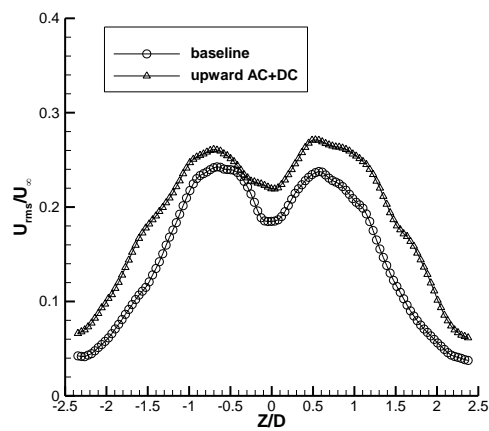
Figure 4.61: Wake streamwise turbulence intensity (AC+DC, *X/D*=4, *U*$_\infty$=5 m/s).

The transverse mean velocity and turbulent intensity profiles are shown in Figures 4.57-4.59. The results show that the transverse velocity is suppressed by the plasma actuation. At X/D=2, the peak velocity is reduced from ±0.24 to ±0.1; at X/D=3, the peak velocity is reduced from ±0.06 to ±0.02; and for X/D=4, the transverse velocity becomes nearly zero under the plasma actuation.

For the transverse turbulent intensity, At X/D=2, the maximum turbulent intensity value increased from 0.6 to 0.7 and the overall level is also increased. The plasma actuation results in overall increment in transverse turbulent intensity at X/D=3 but with the same maximum value. At X/D=4, the maximum turbulent intensity value is reduced from 0.48 to 0.44 but transverse turbulent intensity still increased in the Z/D≥0.5 and Z/D≤-0.5 region. These results suggest that the plasma actuation enhanced the unsteady transverse wake motion associated with near-wake Karman vortex shedding.

a) **Mean velocity**　　　　　　　b) **Turbulence intensity**
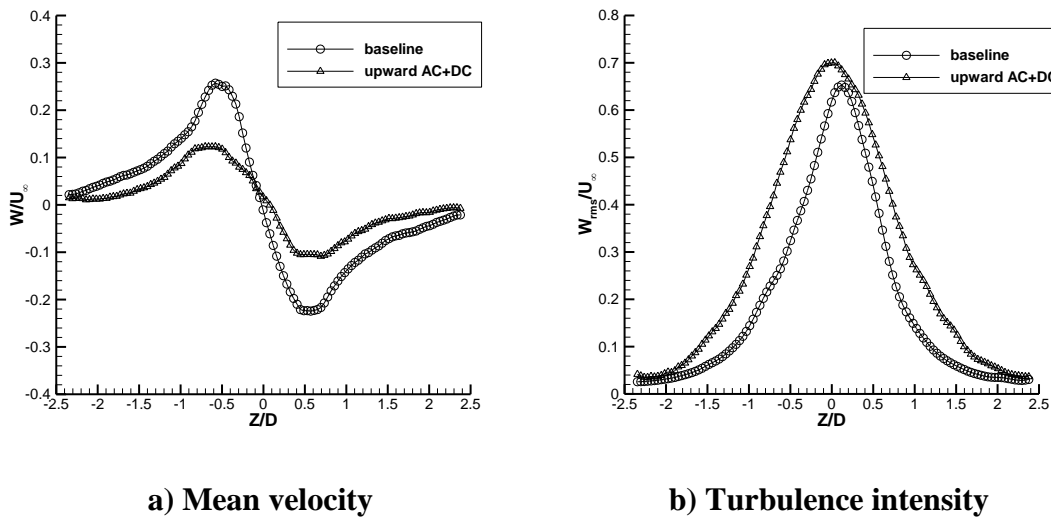
Figure 4.62: Wake transverse velocities (AC+DC, X/D=2, U_∞=5 m/s).

a) Mean velocity   b) Turbulence intensity
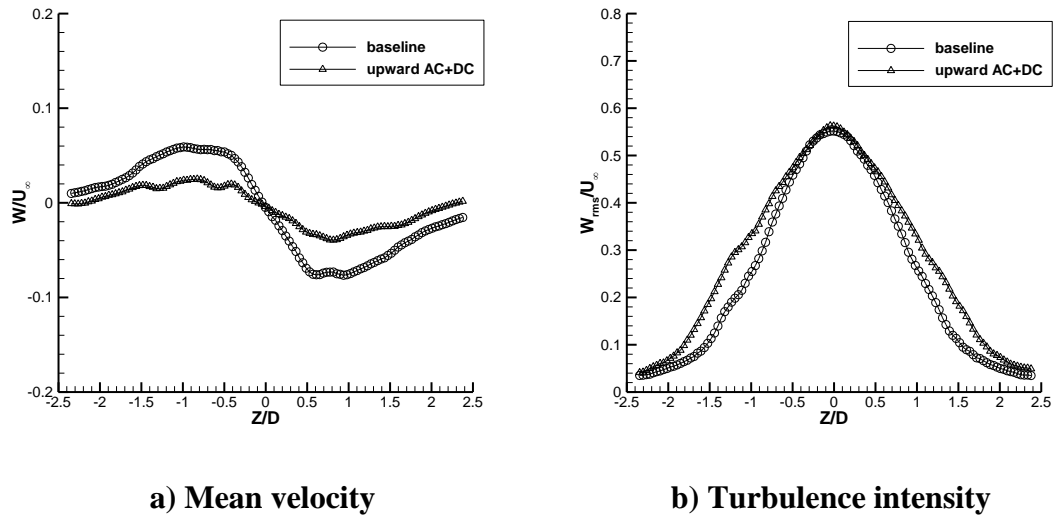
Figure 4.63: Wake transverse velocities (AC+DC, *X/D*=3, U_∞=5 m/s).

a) Mean velocity   b) Turbulence intensity
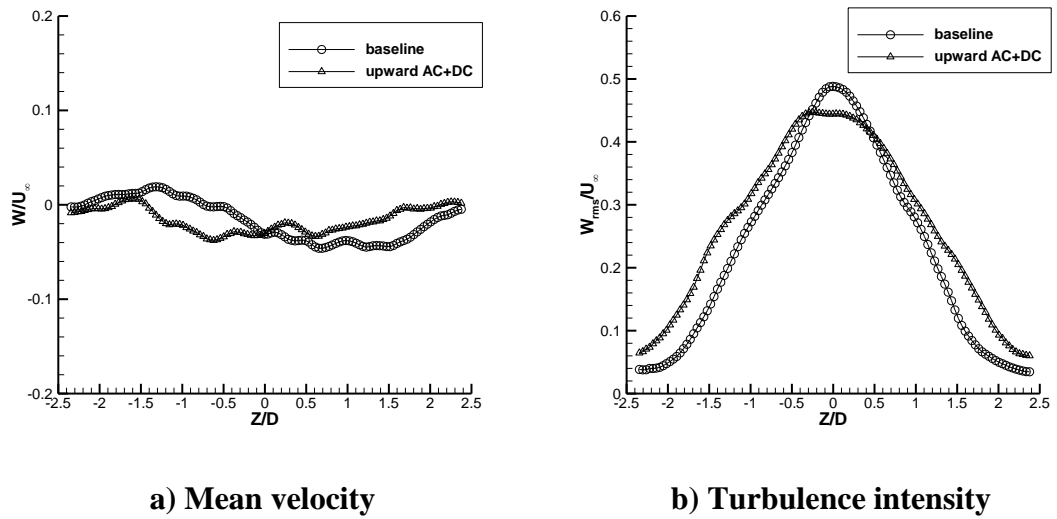
Figure 4.64: Wake transverse velocities (AC+DC, *X/D*=4, U_∞=5 m/s).

Sectional drag coefficients were also calculated for the AC+DC based upward plasma actuation at U_∞=5 m/s using Eq. (4.4). The drag coefficients at different sections are shown in Figure 4.65. The results indicated that an overall 29% drag augment is achieved by the plasma actuation.
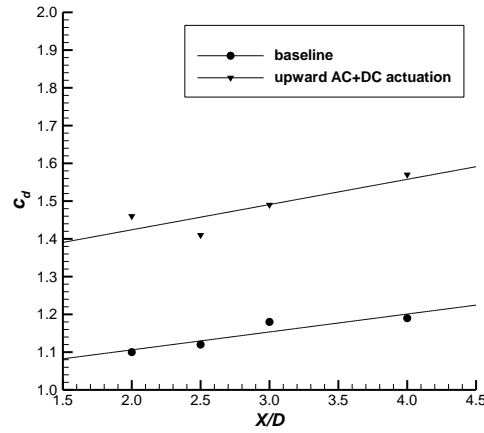
Figure 4.65: Comparison of cylinder drag coefficients (AC+DC, U_∞=5 m/s).

The effects of the upward AC+DC plasma actuation at different Reynolds numbers are shown in Figure 4.66-4.68. Three Reynolds numbers of Re_D =7,000, 12,000 and 24,000 (corresponding U_∞=3 m/s, 5 m/s and 10 m/s) were tested under the same plasma actuation (V_{pp}=17.5 kV, DC=-10 kV). At U_∞=3 m/s, the maximum velocity defect $\Delta U_{max}/U_\infty$ reduces from 0.7 to 0.58, the wake half width $b_{1/2}$ increases from 1.1D to 1.4D. At U_∞=5 m/s the maximum velocity defect $\Delta U_{max}/U_\infty$ reduces from 0.6 to 0.48, the wake half width $b_{1/2}$ increases from 1.03D to 1.53D. At U_∞=10 m/s, there is no change of both the maximum velocity defect and the wake half width.

At U_∞=3 m/s, the highest velocity fluctuation occurring at $Z/D \approx \pm 0.4$ for the baseline case, with the plasma actuation, this position changes to $Z/D \approx \pm 0.7$ and the peak turbulence intensity under the plasma actuation is reduced from 0.39 to 0.33. At U_∞=5 m/s, the peak turbulence intensity under the plasma actuation is unchanged but the highest velocity fluctuation position changes from $Z/D \approx \pm 0.5$ to $Z/D \approx \pm 0.8$ under the plasma actuation. For U_∞=10 m/s, these is no obviously change occurs. With the increase of Reynolds number, the plasma effect is reduced.
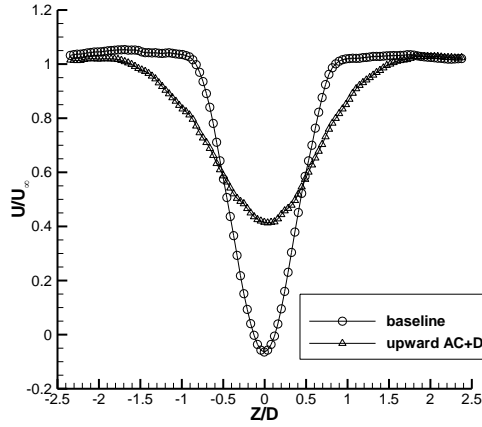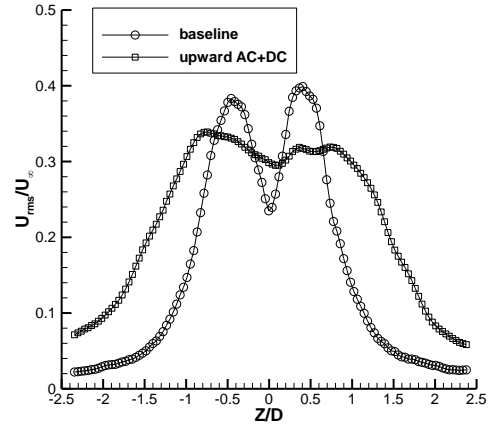
a) Mean velocity   b) Turbulence intensity

Figure 4.66: Wake streamwise velocities at Re_D=7,000 (AC+DC, X/D=2.5).
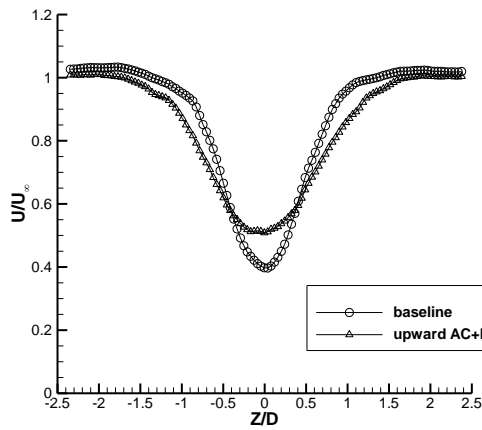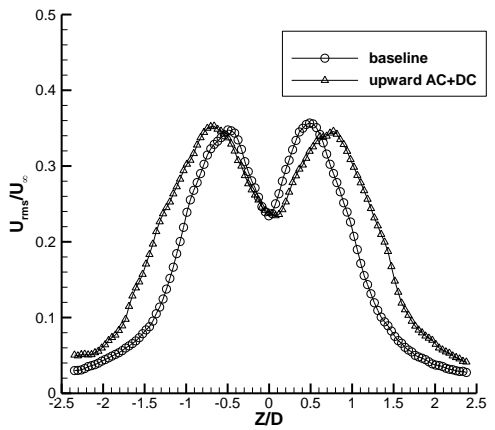
a) Mean velocity   b) Turbulence intensity

Figure 4.67: Wake streamwise velocities at Re_D=12,000 (AC+DC, X/D=2.5).

a) Mean velocity   b) Turbulence intensity
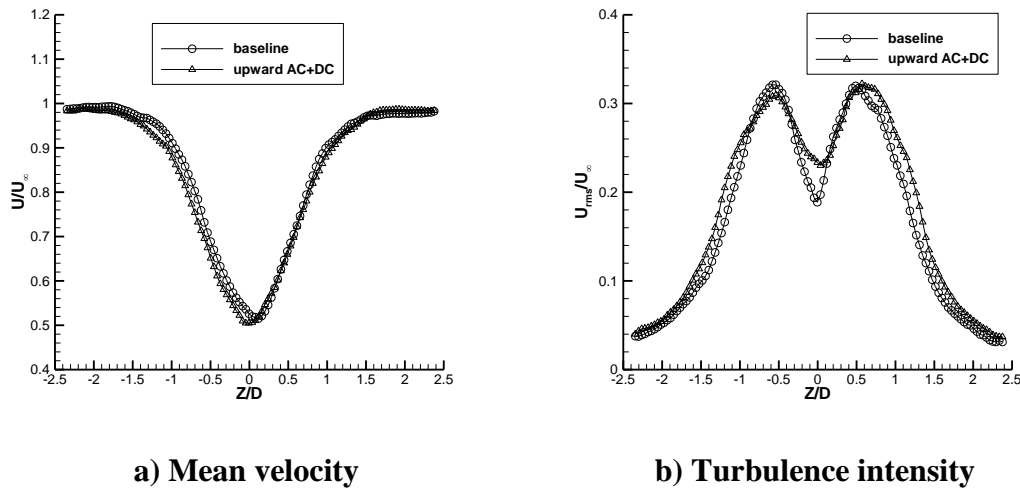
Figure 4.68: Wake streamwise velocities at Re_D=24,000 (AC+DC, X/D=2.5).

The sectional drag coefficients at X/D=2.5 under the plasma actuation for U_∞=3 , 5, and 10 m/s are 1.65, 1.41 and 1.28, respectively, results in the corresponding drag increments of 34%, 26% and 6.7%, respectively.

4.4.2 Results of a SD Based Upward Actuation

Experiments were conducted to compare the effects between the AC+DC based five-electrode (see Figure 4.49) and a corresponding SD based five-electrode actuator (see Figure 4.13). Both actuators were tested at the same plasma actuation condition (AC=17.5 kV, DC=-10 kV) and freestream velocity (U_∞=5 m/s).

Typical results at X/D=2.5 are shown in Figures 4.69 and 4.70. Compare to the baseline case, the maximum streamwise velocity defect $\Delta U_{max}/U_\infty$ and the peak streamwise turbulence intensity for both actuations are almost the same. As to the transverse velocities, the effects of both actuations are also very similar. The results indicate that a SD based actuator has nearly the same efficient as an AC+DC based actuator for the upward actuation under the tested condition.
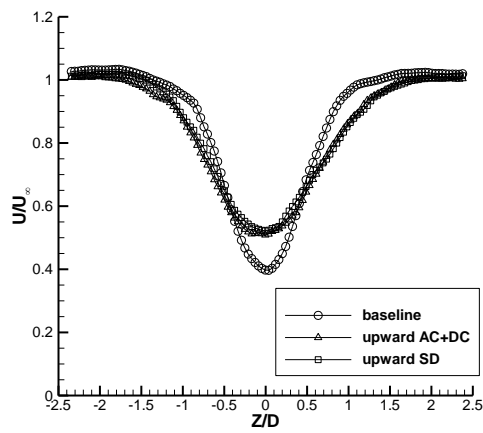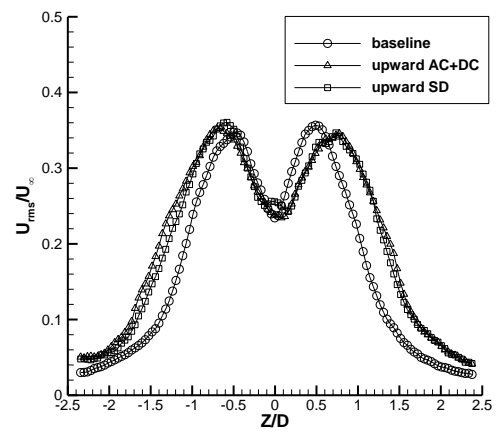
a) Mean velocity   **b) Turbulence intensity**

Figure 4.69: Comparison of AC+DC and SD based upward actuations (streamwise velocities).
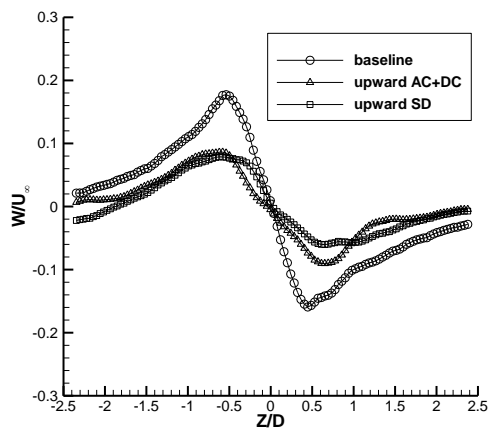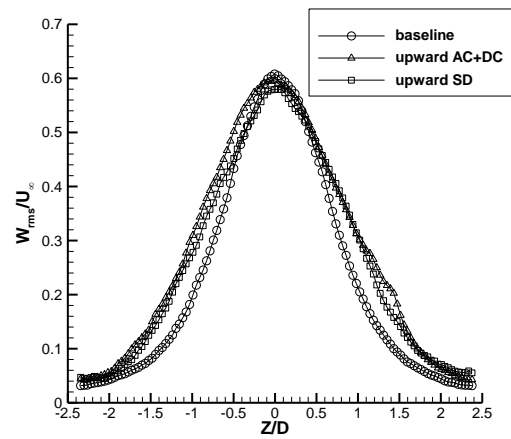
a) Mean velocity   **b) Turbulence intensity**

Figure 4.70: Comparison of AC+DC and SD based upward actuations (transverse velocities).

4.5 Summary

In this chapter, experimental study is conducted to investigate the wake flow field from a circular cylinder by introducing jet with SD/ AC+DC based five-electrode plasma jet actuator. The downward and upward jets were induced by electrode arrangements with the same five electrodes mounted on the circular cylinder model. The characteristics of a single SD actuator and the combined five-electrode actuator in the quiescent air were tested. Compare to a normal DBD actuator, the SD actuation can induce a thicker wall jet and the maximum velocity is increased with the applied DC high voltage. At a fixed applied high DC voltage, a thicker wall jet and a higher induced maximum velocity can be obtained with a higher applied AC voltage. The combined SD actuators effectively produces a jet downstream the cylinder model in absent of an outer flow.

The mean velocity profiles and the turbulent intensities in the wake behind the circular cylinder were measured using PIV at a Reynolds number varies from 7,000 to 24,000. The characteristics of the vortex shedding frequencies are changed by the downward jet and upward jet of the plasma actuators. A maximum 52% sectional drag reduction and 34% drag augment were obtained in the study. The study suggested that this novel SD/AC+DC based five-electrode plasma actuator can be used either for flow separation suppression or enhancement by simply adjusting the actuator electric circuits and is potential for practical flow control applications.

Chapter 5

Conclusion and Future Work

This chapter presents conclusions related to the TBL and circular cylinder flow control experiments using plasma based jet actuators. Recommendations for the future work are also presented.

5.1 Conclusions

This dissertation presents an experimental investigation of a new zero-mass flux plasma actuator consisting of a normal DBD actuator set within a two slots cavity unit. This novel actuator produces a transverse plasma jet into the operating flow field but with no mass flux exchange in the working fluid. Wind tunnel experiments were conducted to assess the performance of the actuator for TBL flow control. The experimental results show that the interaction of the actuator flow with the oncoming TBL flow is similar to that reported for conventional blowing jets but without net mass changes.

It was found that the plasma jet actuator produced a transverse jet similar to a continuously blowing jet but with no mass addition into the flow field. The device is different from a traditional alternative blowing-and-suction synthetic jet as the current jet is continuously blown. As such, the DBD based jet actuator is different from either a mass injection blowing jet actuator or a traditional diaphragm based synthetic jet actuator. It is the belief of the author that the device is a new and innovative one.

The plasma actuation effect along the streamwise direction is similar to that of a traditional blowing jet; in the vicinity of the plasma jet blowing slot, the flow is accelerated and the boundary layer displacement thickness, the momentum thickness and the shape factor are all reduced. Further downstream of the actuation slot, the

actuation results in an increment of the boundary layer shape parameter and the changes gradually decreases with the increasing distance from the blowing slot.

Based on the experimental results obtained in in this dissertation the following conclusions are drawn:

- The DBD based jet actuator is different from either a mass injection blowing jet actuator or a traditional diaphragm based synthetic jet actuator. The frequency of jet equals the plasma driving signal frequency and can reach tens kHz.
- The plasma actuation effect along the streamwise direction is similar to that of a traditional blowing jet.
- The effect of the plasma jet actuation on the mean velocity becomes less significant with increasing freestream flow speed.
- Different air supply slot locations have similar effect on the boundary layer and the fresh air supply slot design can fit the required operating condition flexibly, this is helpful for its flow control applications.

A new designed SD/ AC+DC based five-electrode plasma jet actuator is applied to a circular cylinder wake flow control. These five electrodes were mounted on the rear half part of circular cylinder and the induced plasma sheet covers the whole rear half part cylinder. The downward and upward jets to the main flow direction can easily induced by simply adjust the plasma five electrodes electrical connections. A maximum 52% sectional drag reduction and 34% drag increment were obtained in the study. The study suggested that this new designed five-electrode actuator for flow separation suppression or enhancement application by adjusting the plasma actuator electric circuits conveniently and can be used to practical flow control for drag reduction or noise suppression. In contrast to the plasma-off case, the plasma actuations change the cylinder wake flow characteristics significantly. It can be concluded that:

- Compare to a normal DBD actuator, the sliding discharge actuation can induce a thicker wall jet and the maximum velocity is increased with the applied DC high voltage.
- At a fixed applied high DC voltage, a thicker wall jet and a higher induced maximum velocity can be obtained with a higher applied AC voltage.

- For the downward actuations, both the maximum velocity defection and the maximum turbulence intensity in the wake region decreased under the plasma actuation.

- The sectional drag coefficients reduced under the downward plasma actuation and on the contrary, the sectional drag coefficients increased under the upward plasma actuations. Both the drag reduction and augment decreased with the increasing of Reynolds number.

- The mean wake width and the wake unsteadiness are increased under the influence of the upward plasma actuation.

- For both downward and upward actuations, the control effectiveness of an AC+DC based five-electrode actuator is very similar to a corresponding SD based actuator.

- The transverse velocity distributions become more stable compared to the baseline case for both upward and downward actuations.

- Parameter study results suggest that an expected result may be achievable using the SD actuation with corresponding lower AC voltage and hence with less energy consumption.

5.2 Recommendations for Future Work

This study has demonstrated the ability of plasma based jet actuators to control a TBL flow and a circular cylinder wake flow. Base on the current study, the following work is suggested for the future research:

- Improve DBD based plasma jet actuator performance and its applications. These works include the optimization of the actuator parameters and investigations its effects in other flow control applications such as airfoil, bluff body and so on.

- Improvement of the three-electrode plasma actuators. Optimize those actuators in terms of induced velocity, electrical power consumption and plasma actuator array design.

- Investigate the flow field with plasma actuation in more details. Because the plasma actuator creates a high intensity electric field and ion flow in the test section, so there is small corona discharge around the exposed parts of the hot-wire probe. To resolve this issue, more studies on the hot-wire anemometry should be done.

Although the PIV results presented in the current study show a good resolution at certain distance downstream the cylinder, the quality of the velocity field near the cylinder surface was not sufficient, due to reflected laser light and plasma glare. An optical filter maybe helpful for the velocity field measurement close to the surface in future PIV experiments.

- Circular cylinder flow control using the front mounted plasma based jet actuators. In this study, all the plasma actuators were mounted on the rear half part of the cylinder model. The actuations on the front part of the cylinder model are also a very interesting work.

- In this circular cylinder flow control study, the tested Reynolds numbers were in the subcritical flow regime with laminar flow separation. Further work for the sake of further extension of the Reynolds number range is also very important.

Bibliography

[1] Corke, T. C., Enloe, C. L., and Wilkinson, S. P., 2010, "Dielectric barrier discharge plasma actuators for flow control", *Annu. Rev. Fluid Mech.*, Vol. 42, pp. 505–29.

[2] Glezer, A., and Amitay, M., 2002, "Synthetic jets," *Annual Review of Fluid Mechanics.* Vol. 34, pp. 503–529.

[3] Cattafesta III, L.N., and Sheplak, M., 2011, "Actuators for active flow control," *Annu. Rev. Fluid Mech.*, Vol. 43, pp. 247–272.

[4] Roth, J. R., 2001, "Industrial Plasma Engineering." Institute of Physics Publishing, Bristol and Philadelphia.

[5] Forte, M., Jolibois, J., Pons, J., Moreau, E., Touchard, G., and Cazalens, M., 2007, "Optimization of a dielectric barrier discharge actuator by stationary and non-stationary measurements of the induced flow velocity - application to airflow control," *Experiments in Fluids*, Vol 43, pp.917–928.

[6] Moreau, E., Labergue, A., and Touchard, G., 2005, " DC and pulse surface corona discharge along a PMMA flat plate in air: electrical properties and discharge-induced ionic wind," *Journal of Advanced Oxidation,* Vol 8, pp. 241–247.

[7] Roth, J. R., Sherman, D., and Wilkinson, S., 1998, "Boundary layer flow control with a one atmosphere uniform glow discharge surface plasma," *36th AIAA Aerospace Sciences Meeting & Exhibit,* AIAA paper 98-0328.

[8] Roy, S., and Gaitonde, D., 2004, "Ionized collision flow model for atmospheric rf application," *35th AIAA Plasma dynamics and Lasers Conference,* AIAA paper 2004-2354.

[9] Boeuf, J., Lagmich, Y., Callegari, T., Pitchford, L., and Unfer, T., 2008 ,"New insights in the physics of DBD plasma actuators for flow control," *46th AIAA Aerospace Sciences Meeting and Exhibit,* AIAA paper 2008-1376.

[10] Boeuf, J., Lagmich, Y., Unfer, T., Callegari, T., and Pitchford, L., 2007, "Electrohydrodynamic force in dielectric barrier discharge plasma actuators." *J. Phys. D: Appl. Phys.,* Vol. 40, pp. 652-662.

[11] Boeuf, J., and Pitchford, L., 2005, "Electrohydrodynamic force and aerodynamic flow acceleration in surface dielectric barrier discharge," *Journal of Applied Physics*, Vol. 97, pp. 103-130.

[12]Enloe, C., McLaughlin, T., Van-Dycen, R., Kachner, K., Jumper, E., Corke, T., Post, M., and Haddad, O., 2004, "Mechanisms and responses of a single dielectric barrier plasma actuator: Plasma morphology." *AIAA Journal*, Vol. 42, No.3, pp. 589-594.

[13] Enloe, C., McLaughlin, T., Van-Dycen, R., Kachner, K., Jumper, E., Corke, T., Post, M., and Haddad, O., 2004 "Mechanisms and responses of a single dielectric barrier plasma actuator: Geometric effects," *AIAA Journal*, vol. 42, No.3, pp. 595-604.

[14] Moreau, E. 2007, "Airflow control by non-thermal plasma actuators." *J. Phys. D: Appl. Phys.,* Vol.40 No.3, pp.605–636.

[15] Grundmann, S., 2008, "Transition control using dielectric barrier discharge actuators.", *PhD thesis, Technical University Darmstadt*.

[16] Bushnell, D.M., 1983, "Turbulent drag reduction for external flows." *21st AIAA Aerospace Sciences Meeting*, AIAA paper 1983–0227.

[17] El-Khabiry, S.,and Colver, G. M., 1996, "Drag reduction by dc corona discharge along and electrically conductive flat plate for small Reynolds number flow.", *Phys. Fluids,* Vol.9, No.3, pp.587–599.

[18] Moreau, E., Leger, L., and Touchard, G., 2006, "Effect of a DC surface-corona discharge on a flat plate boundary layer for air flow velocity up to 25 m/s." *Journal of Electrostatics,* Vol. 64, No.4, pp. 215–225.

[19] Jukes, T., Choi, K. S., Johnson, G., and Scott, S., 2004, "Turbulent boundary-layer control for drag reduction using surface plasma." *2nd AIAA Flow Control Conference*, AIAA paper 2004–2216.

[20] Jukes, T., Choi, K. S., Johnson, G., and Scott, S., 2006, "Turbulent drag reduction by surface plasma through spanwise flow oscillation." *3rd AIAA Flow Control Conference*, AIAA paper 2006–3693.

[21] Rivir, R., White, A., Carter, C., and Ganguly, B., 2004, "AC and pulsed plasma flow control." *42nd AIAA Aerospace Sciences Meeting,* AIAA paper 2004-0847.

[22] Borghi, C. , Cristofolini, A., Carraro, M., and Neretti, G., 2006, "An analysis of a three phase flat panel uniform barrier discharge at atmospheric pressure," *37th AIAA Plasmadynamics and Lasers Conference* , AIAA paper 2006-3380.

[23] Roth, J., and Dai, X., 2006, "Optimization of the aerodynamic plasma actuator as an electrohydrodynamic (EHD) electrical device," *44th AIAA Aerospace Sciences Meeting and Exhibit*, AIAA paper 2006-1203.

[24] Benard, N., Mizuno, A., and Moreau, E., 2009, "A large-scale multiple dielectric barrier discharge actuator based on an innovative three-electrode design." *J. Phys. D: Appl. Phys.* Vol.42, No.23, 235204(12pp).

[25] Santhanakrishnan, A., and Jacob. J. D., 2007, "Flow control with plasma synthetic jet Actuators." *J. Phys. D: Appl. Phys*. Vol.40, No.3, pp. 637–651.

[26] Louste, C., Artana, G., Moreau, E., and Touchard, G., 2005, "Sliding discharge in air at atmospheric pressure: electrical properties." *J. of Electrostat*. Vol.63, pp.615-620.

[27] Moreau, E., Loustea, C ., and Touchard, G., 2008, "Electric wind induced by sliding discharge in air at atmospheric pressure." *J. of Electrostat*. Vol.66, pp.107-114.

[28] Moreau, E., Sosa, R. and Artana, G. 2008, "Electric wind produced by surface plasma actuators: a new dielectric barrier discharge based on a three-electrode geometry." *J. Phys. D. Appl. Phys*., Vol.41, No.11, 115204(12pp).

[29] Sosa, R., Arnaud, E., Memin, E., and Artana, G., 2008, "Study of the flow induced by a sliding discharge." *IEEE Transactions on Dielectrics and Electrical Insulation*, Vol.16, No.2, pp. 305–311.

[30] Sosa, R., Adamo, J. D. and Artana, G., 2009, "Circular cylinder drag reduction by three-electrode plasma actuators." *Journal of Physics: Conference Series.* Vol.166, No.1, pp. 1–14.

[31] Thomas, F., Corke, T., Wang, M., 2008, "Experimental aircraft noise control using dielectric barrier discharge plasma actuators: benchmark experiments and LES simulations." *NASA Progr. Rep.,* NNX07AO09A.

[32] Roupassov, D. V., Nikipelov, A. A., Nudnova, M. M., and Starikovskii, A. Y., 2009, "Flow separation control by plasma actuator with nanosecond pulsed-periodic discharge," *AIAA J.,* Vol.47, No.1, pp. 168–185.

[33] Roupassov D. V., and Starikovskii, A. Y., 2008, "Development of nanosecond surface discharge in actuator geometry," *IEEE Transactions on Plasma Science,* Vol.36, No.4, pp.1312–13.

[34] Starikovskaia, S. M., 2006, "Plasma assisted ignition and combustion," *J. Phys. D Appl. Phys.* Vol.39, pp.R265–R299.

[35] Starikovskii, A. Y., Nikipelov, A. A., Nudnova, M. M., and Roupassov, D. V., 2009, "SDBD plasma actuator with nanosecond pulse-periodic discharge," *Plasma Sources Sci. Technol.* Vol.18 No.3, 034015(17pp).

[36] George, W., and Castillo, L., 1997, "Zero-pressure-gradient turbulent boundary layer," *Appl. Mech.Rev.,* Vol.50, pp. 689-729.

[37] Tennekes, H., and Lumeley, J.L., 1997, "A first course in turbulence," 16th printing, The MIT Press.

[38] Choi, H., Moin, P., and Kim, J., 1993, "Direct numerical simulation of turbulent flow over riblets," *Journal of Fluid Mechanics*, Vol. 255, pp. 503–539.

[39] Choi, K. S., Yang, X., Clayton, B. R., Glover, E. J., Atlar, M., Semenov, B. N., and Kulik, V. M., 1997, "Turbulent drag reduction using compliant surfaces," *Proceedings of the Royal Society of London Series, A*, Vol. 453, pp. 2229–2240.

[40] Choi, J. I., Xu, C. X., and Sung, H. J., 2002, "Drag reduction by spanwise wall oscillations in wall-bounded turbulent flows," *AIAA Journal*, Vol. 40, No.5, pp. 842–850.

[41] Laadhari, F., Skandaji, L., and Morela, R., 1994, "Turbulence reduction in a boundary layer by a local spanwise oscillating surface." *Phys. Fluids*, Vol.6, No.10, pp.3218-3220.

[42] Choi, K. S., and Clayton, B. R., 2001, "The mechanism of turbulent drag reduction with wall oscillation." *International Journal of Heat and Fluid Flow*, Vol.22, No.1, pp.1–9.

[43] Moin, P., and Mahesh, K., 1998, ''Direct numerical simulation: A tool in turbulence research,'' *Annu. Rev. Fluid Mech.* Vol.30, pp.539-578.

[44] Sano, M., and Hirayama, N., 1985, "Turbulent boundary layers with injection and suction through a slit. First Report: Mean and Turbulence Characteristics," *Bulletin of the Japan Society of Mechanical Engineers*, Vol. 28, pp. 807–814.

[45] Antonia,R. A., Zhu, Y., and Sokolov, M., 1995, ''Effect of concentrated wall suction on a turbulent boundary layer,'' *Phys. Fluids*, Vol.7, No.10, pp. 2465-2474.

[46] Park, J., and Choi, H., 1999, "Effects of uniform blowing or suction from a spanwise slot on a turbulent boundary layer flow," *Phys. Fluids*, Vol.11, No.10, pp.3095–3105.

[47] Krogstad, P. A., and Kourakine, A., 2000, "Some effects of localized injection on the turbulence structure in a boundary layer," *Phys. Fluids*, Vol. 12, No.11, pp. 2990–2999.

[48] Kim, K., Sung, H. J., and Chung, M. K., 2002, "Assessment of local blowing and suction in a turbulent boundary layer," *AIAA J.*, Vol.40, No.6, pp. 175–177.

[49] Tardu, S. F., 2001, "Active control for near-wall turbulence by local oscillating blowing," *J. Fluid Mech.*, Vol. 439, No.1, pp. 217–253.

[50]Park, S. H., Lee, I., and Sung, H. J., 2000, "Effect of local forcing from a spanwise slot on a turbulent boundary layer," *Experiments in Fluids*, Vol. 31, No.4, pp. 384–393.

[51] Rhee, G. H., and Sung, H. J., 2001, "Numerical prediction of locally-forced turbulent boundary layer," *International Journal of Heat and Fluid Flow*, Vol. 22, No.6, pp. 624–632.

[52] Antonia, R. A., Fulachier, L., Krishnamoorthy, L. V., Benabid, T., and Anselmet, F., 1988, "Influence of wall suction on the organized motion in a turbulent boundary layer.", *J. Fluid Mech.*, Vol.190, pp.217-240.

[53] Piomelli, U., Ferziger, J., Moin, P., and Kim, J., 1989, "New approximate boundary conditions for large eddy simulations of wall-bounded flows." *Phys. Fluids,* Vol.1, No.6, pp.1061-1068.

[54] Sumitani , Y., and Kasagi, N., 1995, "Direct numerical simulation of turbulent transport with uniform wall injection and suction," *AIAA Journal*. Vol.33, No.7, pp.1220-1228.

[55] Ingard, U., and Labate, S., 1950, "Acoustic circulation effects and the nonlinear impedance of orifices," *Journal of the Acoustical Society of America.* Vol. 22, pp.211–219

[56] Glezer, A., and Amitay,M., 2002, "Synthetic jets," *Ann. Rev. Fluid Mech.*, Vol 34, pp.503–529.

[57] Mallinson, S.G., Reizes, J.A., and Hong, G., 2001, "An experimental and numerical study of synthetic jet flow," *The Aeronautical Journal*, Vol.105, No.1043, pp. 41–49.

[58] Smith, D.R., Glezer, A., 1998, "The formulation and evolution of synthetic jets," *Phys. Fluids,* Vol.10, No.9, pp. 2281–2297.

[59] Gallas, Q., Mathew, J., Kaysap, A., Holman, R., Nishida, T., Carroll, B., Sheplak, M., and Cattafesta, L., 2002, "Lumped element modeling of piezoelectric-driven synthetic jet actuators, *AIAA Journal,* vol. 41, No. 2, pp. 240-247.

[60] Zhang, X., 1995, "Co- and contra-rotating streamwise vortices in a turbulent boundary layer," *J. Aircraft,* Vol. 33, No.5, pp. 1095–1101.

[61] Wygnanski, I., 1997, "Boundary layer and flow control by periodic addition of momentum," *4th AIAA Shear Flow Control Conference,* AIAA paper 97-2117.

[62] Jenkins, L., Althoff, S., and Anders, S., 2002, "Flow control device evaluation for an internal flow with an adverse pressure gradient," *40th AIAA Aerospace Sciences Meeting & Exhibit*, AIAA paper 2002-0266.

[63] Mallinson, S.G., Kwok, C.Y., and Reizes, J.A., 2003 "Numerical simulation of micro-fabricated zero mass-flux jet actuators," *Sensors and Actuators*, Vol.105, pp. 229–236.

[64] Smith, D.R., Amitay, M., Kibens, V., Oarekh, D.E., and Glezer, A., 1998, "Modification of lifting body aerodynamics using synthetic jet actuators," *36th AIAA Aerospace Sciences Meeting,* AIAA paper 98-0209.

[65] Roos, F.W., 1998, "Synthetic jet microblowing for forebody flow-asymmetry management," *36th AIAA Aerospace Sciences Meeting,* AIAA paper 98-0212.

[66] Crook, A., Sadri, A. M., and Wood, N. J., 1999, "The development and implementation of synthetic jets for the control of separated flow," *17th AIAA Applied Aerodynamics Conference*, AIAA paper 99-3176.

[67] Chen, F. J., Yao, C., Beeler, G. B., Bryant, R.G., and Fox, R.L., 2000, "Development of synthetic jet actuators for active flow control at NASA Langley, *AIAA FLUIDS 2000 Conference and Exhibit*, AIAA paper 2000-2405.

[68] Mittal, R., Rampunggoon, P., and Udaykumar, H. S., 2001, "Interaction of a synthetic jet with a flat plate boundary layer," *15th AIAA Computational Fluid Dynamics Conference,* AIAA paper 2001-2773.

[69] Williamson, C. H. K., 1996, "Vortex dynamics in the cylinder wake," *Annual Review of Fluid Mechanics*, Vol. 28, pp. 477-539.

[70] Zdravkovich, M. M., 1997, "Flow around circular cylinders, Vol. 1:Fundamentals," Oxford Science Publications.

[71] Schlichting, H. and Gersten, K., 2003, "Boundary layer theory", Springer-Verlag, 8th edition.

[72] Prandtl, L., 1927, "The generation of vortices in fluids of small viscosity," *Journal of Royal Aeronautical Society*, Vol. 31, pp. 720 - 741.

[73] Gerrard, J. H., 1966, "The mechanics of the formation region of vortices behind bluff bodies," *J. Fluid Mech.*, Vol. 25, No.2, pp. 401-413.

[74] Gad-el-Hak, M., 2000, "Flow control: passive, active and reactive flow management," Cambridge University Press, Cambridge, UK.

[75] Shih, W. C. L., Wang, C., Coles, D., and Roshko, A., 1993, "Experiments on flow past rough circular cylinders at large Reynolds numbers," *Journal of Wind Engineering and Industrial Aerodynamics*, Vol. 49, No.2, pp. 351–368.

[76] Strykowski, P. J., and Sreenivasan, K. R., 1990, "On the formation and suppression of vortex "shedding" at low Reynolds numbers," *J. Fluid Mech.,* Vol. 218, pp. 71–107.

[77] Sakamoto. H., and Haniu, H., 1994, "Optimum suppression of fluid forces acting on a circular cylinder," *Journal of Fluids Engineering,* Vol. 116, No. 23, pp. 221–227.

[78] Dalton, C., Xu, Y., and Owen, J. C., 2001, "The suppression of lift on a circular cylinder due to vortex shedding at moderate Reynolds numbers," *Journal of Fluids and Structures,* Vol. 15, pp.617–628.

[79] Bearman, P. W., and Harvey, J. K., 1993, "Control of circular cylinder flow by the use of dimples," *AIAA Journal,* Vol. 31, No.10, pp. 1753–1756.

[80] Lee. S, and Kim, H., 1997, "The effect of surface protrusions on the near wake of a circular cylinder," *Journal of Wind Engineering and Industrial Aerodynamics,* Vol. 69-71, pp. 351–361.

[81] Kwon, K., and Choi, H., 1996, "Control of laminar vortex shedding behind a circular cylinder using splitter plates," *Phys. Fluids,* Vol. 8, No.2, pp. 479–486.

[82] Anderson, E., and Szewczyk, A., 1997, "Effects of a splitter plate on the near wake of a circular cylinder in 2 and 3-dimensional flow configurations," *Experiments in Fluids,* Vol. 23, No.2, pp.161–174.

[83] Ozono, S., 1999, "Flow control of vortex shedding by a short splitter plate asymmetrically arranged downstream of a cylinder," *Phys. Fluids* Vol. 11, No.10, pp. 2928–2934.

[84] Hwang, J. Y., Yang, K. S., and Sun, S. H., 2003, "Reduction of flow-induced forces on a circular cylinder using a detached splitter plate," *Phys. Fluids,* Vol. 15, No.8, pp. 2433–2436.

[85] Lim, H., and Lee, S., 2002, "Flow control of circular cylinders with longitudinal grooved surfaces," *AIAA Journal,* Vol. 40, No.10, pp.2027–2036.

[86] Amitay, M., Smith, B. L., and Glezer, A., 1998, "Aerodynamic flow control using synthetic jet technology," *36th AIAA Aerospace Sciences Meeting and Exhibit*, AIAA paper 98–0208.

[87] Blackburn, H., and Henderson, R. 1999, "A study of two-dimensional flow past an oscillating cylinder," *J. Fluid Mech.* Vol. 385, pp.255–286.

[88] Cetiner, O., and Rockwell, D., 2001, "Streamwise oscillations of a cylinder in a steady current. Part 1: locked-on states of vortex formation and loading," *J. Fluid Mech.* Vol. 427, pp. 1–28.

[89] Carberry, J., Sheridan, J., and Rockwell, D., 2003, "Controlled oscillations of a cylinder: a new wake state," *Journal of Fluids and Structures,* Vol. 17, pp. 337–343.

[90] Williams, D., Mansy, H., and Amato, C., 1992, "The response and symmetry properties of a cylinder wake subjected to localized surface excitation," *J. Fluid Mech.,* Vol. 234, pp.71–96.

[91] Lin, J., Towfighi, J., and Rockwell, D., 1995, "Near-wake of a circular cylinder: control by steady and unsteady surface injection," *Journal of Fluids and Structures,* Vol. 9, No.6, pp. 659–669.

[92] Delaunay, Y., and Kaiktsis, L., 2001, "Control of circular cylinder wakes using base mass transpiration," *Phys. Fluids,* Vol. 13, No.11, 3285(18pp).

[93] Arcas, D., and Redekopp, L., 2004, "Aspects of wake vortex control through base blowing/ suction," *Phys. Fluids* Vol. 16, No.2, pp.452–456.

[94] Fujisawa, N., Takeda, G., and Ike, N., 2004, "Phase-averaged characteristics of flow around a circular cylinder under acoustic excitation control." *Journal of Fluids and Structures,* Vol. 19, No.2, pp.159–170.

[95] Konstantinidis, E., Balabani, S., and Yianneskis, M., 2005, "The timing of vortex shedding in a cylinder wake imposed by periodic inflow perturbations," *J. Fluid Mech.* Vol. 543, pp. 45–55.

[96] Kim, S., and Lee, C., 2000, "Investigation of the flow around a circular cylinder under the influence of an electromagnetic force," *Experiments in Fluids,* Vol. 28, No.3, pp. 252–260.

[97] Artana, G., Sosa, R., Moreau, E., and Touchard, G., 2003. "Control of the near-wake flow around a circular cylinder with electrohydrodynamic actuators," *Experiments in Fluids,* Vol. 35, No.5, pp. 580–588.

[98] Kim, J., Choi, H., 2005, "Distributed forcing of flow over a circular cylinder," *Phys. Fluids,* Vol. 17, No.3, 033103(16pp).

[99] Tokumaru, P. T, and Dimotakis, P. E., 1991, "Rotary oscillatory control of a cylinder wake," *J. Fluid Mech.,* Vol. 224, pp. 77–90.

[100] Thomas, F. O., Kozlov A., and Corke, C., 2008, "Plasma actuators for cylinder flow control and noise reduction," *AIAA Journal*, Vol.46, No.8, pp. 1921-1931.

[101] Gregory, J. W., Porter, C. O., and McLaughlin, T. E., 2008, "Circular cylinder wake control using spatially distributed plasma forcing," *4th AIAA Flow Control Conference* , AIAA paper 2008-4198.

[102] Jukes, N., Timothy and Choi, K. S., 2009, "Control of unsteady flow separation over a circular cylinder using dielectric-barrier discharge surface plasma," *Phys. Fluids*, Vol. 21, No.9, 094106(15pp).

[103] Maina, E. I., 2004, "The development of passive flow control vortice," *PhD thesis*, University of Southampton.

[104] Peers, E., Huang, X., and Luo, X., 2009, "A numerical model of plasma-actuator effects in flow-induced noise control," *IEEE transactions on plasma*, Vol. 37, No. 11, pp. 2250-2256.

[105] Krogstad, P. A., and Kourakine, A., 2000, "Some effects of localized injection on the turbulence structure in a boundary layer," *Phys. Fluids*, Vol.12, No.11, pp.2990–2999.

[106] Zhang, X., Luo, X. and Chen, P., 2011, "Airfoil flow control using plasma actuation and Coanda effect ," *29th AIAA Applied Aerodynamics Conference*, AIAA paper 2011-3516.

[107] Bloor, M. S., 1964, "The transition to turbulence in the wake of a circular cylinder," *J. Fluid Mech.,* Vol. 19, pp. 290–304.

[108] Antonia, R. A., and Rajagopalan, S., 1990, "Determination of drag of a circular cylinder," *AIAA Journal*, Vol. 28, No. 10, pp. 1833-1834.

[109] Ong, L. and Wallace, J., 1996, "The velocity field of the turbulent very near wake of a circular cylinder," *Experiments in Fluids*, Vol.20, No.6, pp.441-453.

[110] Gregory, J. W., Porter, C. O., and McLaughlin, T. E., 2008, "Circular cylinder wake control using spatially distributed plasma forcing," *4th AIAA Flow Control Conference*, AIAA paper 2008-4198.